POLITECNICO DI TORINO

Collegio di Ingegneria Chimica e dei Materiali

Corso di Laurea Magistrale
in Ingegneria Chimica e dei Processi Sostenibili

Tesi di Laurea Magistrale

Assessment of corrosion behaviour of SLM AlSi10Mg alloy: as-printed, heat treated and cast counterpart

Relatori:

Grassini Sabrina
Angelini Emma Paola Maria Virgina
Badini Claudio Francesco
Padovano Elisa

Candidato
Dolly Vanesa Sánchez

Dicembre 2020

TABLE OF CONTENTS

Studio del comportamento a corrosione della lega AlSi10Mg ottenuta per Additive Manufacturing, trattata termicamente e paragonata con il cast

I. INTRODUZIONE

In qualità di ingegneri chimici, un importante compito di cui è possibile farsi carico riguarda lo sviluppo di tecnologie e di materiali innovativi allo scopo di rendere i processi industriali più eco sostenibili. Questo avrà come principale obbiettivo la diminuzione dell'impatto ambientale offrendo così un cammino orientato all'economia verde. Un esempio di questo, è l'utilizzo dei materiali *light-weight*, come le leghe di alluminio invece delle classiche leghe in acciaio per applicazioni automobilistiche. In questa maniera, la riduzione del peso dell'autoveicolo consente un'importante riduzione in termini di carburante con conseguente riduzione di emissioni di CO_2 in atmosfera. Tra le diverse tecnologie di produzione di materiali metalli, ci viene in aiuto oggigiorno l'*Additive Manufacturing* (AM), che promette una via economicamente sostenibile per la produzione di parti automobilistiche; offrendo la possibilità alle case di produzione di personalizzare velocemente la parte desiderata tramite *computer-aided* design, e riprodurla in massa. Tuttavia, prima che un nuovo materiale sia incluso nella produzione di massa, questo deve superare con successo una fase di prototipazione. Questa fase mira a valutare ogni proprietà meccanica, fisica e chimica necessaria per assicurare una corretta prestazione finale. In questa valutazione è necessario includere la determinazione del comportamento a corrosione, che potrebbe limitare l'uso di un metallo a fronte degli effetti deleteri che potrebbe comportare sul pezzo.

Per tali motivazioni questo lavoro di tesi è stato sviluppato con l'obiettivo principale di valutare la resistenza alla corrosione di una particolare lega di alluminio, conosciuta come AlSi10Mg, prodotta con la tecnologia AM di Fusione Laser Selettiva (*Selective Laser* Melting - SLM). Inoltre, poiché le proprietà meccaniche sono abbastanza importanti nel settore automobilistico, un trattamento termico è stato eseguito sul materiale citato al fine di ridurre le tensioni residue caratteristiche delle tecnologie *additive*. Per comprendere al meglio la tecnica precedentemente citata, un capitolo intero di questa tesi[1] è stato dedicato ad approfondire i suoi parametri, gli effetti sulla microstruttura e il comportamento generale alla corrosione delle parti metalliche risultanti.

Essendo un potenziale materiale da utilizzare nelle applicazioni automobilistiche, va tenuto conto anche il principale processo di fabbricazione utilizzato per le parti in alluminio nelle automobili. Si tratta del processo *casting*, che genera quasi il 64% di tutte le parti in alluminio (secondo un'analisi di *Ducker Frontier* per i veicoli nel 2019 [1]). Pertanto, la valutazione della corrosione dei campioni di AM è confrontata con la forma più utilizzata della lega di alluminio, cioè, AlSi10Mg *cast*. L'applicazione dell'alluminio all'industria automobilistica e le principali caratteristiche del citato metallo sono descritte in un capitolo completo all'interno di questo lavoro[2]. Inoltre, è anche presentata un'introduzione sull'interpretazione delle immagini di microstruttura, nonché la sequenza di processi che ogni campione ha subito.

Per quanto riguarda la parte sperimentale di questa tesi, lo studio sistematico della corrosione viene effettuata comprendendo due principali prove elettrochimiche: prove di polarizzazione potenziostatica e spettroscopia d'impedenza elettrochimica (*Electrochemical Impedance Spectroscopy* - EIS). Entrambe i test condotti forniscono risultati tra loro complementari, che aiutano così a caratterizzare in modo più approfondito l'andamento della

[1] Capitolo 2 presente nel testo principale di questa tesi.

[2] Capitolo 3 presente nel testo principale di questa tesi.

corrosione della lega nelle sue tre configurazioni (*as-printed* AP, trattata termicamente HT e l'omologo cast). Queste due prove sono state eseguite mediante l'utilizzo di una cella elettrochimica, composta da tre elettrodi collegata ad un potenziostato. I risultati sono stati ottenuti e analizzati con il software *IviumSoft*. I tre elettrodi menzionati sono immersi in una soluzione di cloruro di sodio 0.6 M, soluzione definita *artificial seawater* in quanto ha una percentuale in peso di cloruri simile a quella dell'acqua marina.

Nel primo caso sperimentale viene valutata la variazione nella densità di corrente di corrosione alla variazione del potenziale. Questo andamento è fornito in un grafico dal quale è possibile estrarre i parametri termodinamici e cinetici che descrivono il comportamento a corrosione della lega. Essi sono rispettivamente, il potenziale di corrosione (E_{corr}) e la densità di corrente di corrosione (i_{corr}). Da quest'ultima è possibile determinare la velocità di corrosione.

La seconda prova sperimentale (EIS) riguarda la valutazione del particolare rivestimento passivo che si forma sulle leghe di alluminio quando sono esposte ad ambienti corrosivi. Per ottenere i parametri rappresentativi di tale strato occorre eseguire una serie di procedure di modellizzazione. Inoltre, vengono presentati due tipi standard di grafici EIS: i grafici Bode e Nyquist. Ognuno di essi fornisce ulteriori informazioni sulla resistenza dello strato.

Un obiettivo molto importante, e non ancora menzionato, di questa tesi è quello di studiare l'anisotropia che spesso presentano le parti generate dalla tecnologia additive. A tal fine vengono analizzati due piani caratteristici: uno parallelo (XZ) ed un altro perpendicolare (XY) alla direzione di fabbricazione (Z) per ogni campione AP e HT.

L'interpretazione di ogni prova EIS e dei risultati delle prove di polarizzazione non sarebbe completa se non fosse eseguita anche l'analisi della microstruttura. A questo scopo viene utilizzato il microscopio elettronico a scansione a emissione di campo (*Field Emission Scanning Electron Microscope* - FESEM), in quanto fornisce micrografie a diversi ingrandimenti. Su questi possono essere facilmente identificate le diverse fasi delle microstrutture, la loro morfologia, dimensioni caratteristiche ed eventuale porosità. Pertanto, sarebbe possibile identificare quali sono le caratteristiche che influenzano maggiormente il comportamento a corrosione delle diverse leghe, tenendo conto delle tecniche di fabbricazione e post-fabbricazione. In effetti, questi argomenti saranno commentati nel capitolo finale sugli sperimenti e discussione.

Questa tesi è stata realizzata come parte del progetto di ricerca "Corrosion behaviour of metallic materials for automotive processed according to different technologies" in Accordo di Cooperazione fra FCA-CRF e il Politecnico di Torino.

I-a L'Additive Manufacturing (AM)

Con questo termine si fa riferimento a una tecnologia innovativa, ma ancora in continua ottimizzazione, per la produzione mediante stratificazione successiva (*layer by layer*) di elementi tridimensionali [2]. Anche se è possibile utilizzare diversi materiali come materie prime, ad esempio ceramiche o polimeri, in questa tesi si farà riferimento all'utilizzo dei soli materiali metallici [3] per la loro applicazione nel settore automobilistico. In particolare, l'utilizzo di materiali leggeri, quali l'alluminio ha sempre più importanza in quanto possono raggiungere ottimi requisiti di rigidezza dopo essere stati sottoposti a trattamenti termici [4] permettendo una riduzione del peso totale. Tuttavia, la formabilità rimane una sfida piuttosto grande in quanto molte parti possiedono una geometria molto complessa. È per questa ragione che il processo SLM risulta interessante per la produzione di parti veicoli, dato che il prodotto fabbricato strato dopo strato raggiunge la forma desiderata senza che siano necessari ulteriori trattamenti. Inoltre, l'uso di materiali leggeri comporta altri benefici riguardanti l'impatto ambientale, che diminuisce dato che il consumo di benzina è minore. Se invece si considerano i veicoli elettrici, la loro autonomia sarà maggiore con l'uso di leghe leggere.

Uno dei principali vantaggi di questa tecnologia sta nella progettazione del componente, la quale essendo basata su un modello digitale (*Computer-aided design* - CAD) [5] permette di avere una più ampia possibilità di modellazione rispetto ai processi tradizionali. Avendo definito la geometria del componente, il fascio laser fonde selettivamente il letto di polvere seguendo il CAD [6], come mostrato in **Figura 2.1**[3]. Questa operazione è comunemente conosciuta come Fusione Laser Selettiva (*Selective Laser Melting* - SLM). Il letto di polvere si trova su una piattaforma di costruzione (*building platform*), la quale è definita con le coordinate X-Y mentre la direzione di fabbricazione avrà la coordinata Z. Lo spessore di ogni strato di polvere per la fabbricazione dei campioni usati in questa tesi è di 30 μm. Una volta che uno strato è stato fuso mediante il laser di 400 W di potenza e a una velocità di 1300 mm/s, la piattaforma di costruzione si abbassa per continuare con la successiva deposizione di un nuovo strato di polvere mediante un *recoater*. Lo strato successivo invece viene fuso con un'orientazione ruotata di 67º rispetto allo strato precedente. Quando la fabbricazione del pezzo è finita, la polvere restante che non è stata fusa viene rimossa [7].

I principali parametri della tecnologia additiva sono definiti nella **Figura 2.2**[4]. Tra questi è importante menzionare la potenza del laser e la velocità di scansione che determinano la quantità di energia trasferita a una quantità specifica di volume di polvere [8]. Se sono scelte adeguatamente insieme allo spessore del letto di polvere si produce una traccia di aspetto continuo e uniforme. L'energia trasferita deve anche assicurare la fusione dello strato sottostante per avere una continuità nel prodotto finito. Tra gli effetti negativi prodotti da una inadeguata quantità di energia trasmessa, sia eccessiva che insufficiente, abbiamo: la porosità, l'effetto *balling*, tracce di composti ossidati, l'effetto *keyhole* e la perdita di composti volatili [9]. I parametri sopracitati, descritti nella figura, determinano la microstruttura prodotta. Per esempio, se la velocità di raffreddamento viene aumentata, sia per un aumento nel gradiente termico o per velocità di solidificazione elevati (quest'ultima determinata dalla velocità di scansione), allora si otterrà una microstruttura più fina [10]. Per ogni tipo di lega vengono comunque eseguite diverse sperimentazioni al fine di trovare i parametri più adatti per produrre le caratteristiche desiderate nel prodotto finale.

---

[3] Immagine presente nella Sezione 2.1 del testo principale di questa tesi.

[4] Immagine presente nella Sezione 2.1 del testo principale di questa tesi.

I-b Corrosione in leghe prodotte dall'AM.

Per quanto riguarda la corrosione delle leghe prodotte dalle tecnologie additive la porosità è una delle caratteristiche più influenti [11]. Questa può essere prodotta dalla porosità della polvere della lega inizialmente usata, oppure formata in seguito a causa dei gas intrappolati durante il processo di fabbricazione. Inoltre, ottimizzando i parametri dell'operazione AM è possibile diminuire la porosità. Quest'ultima è correlata al tipo di corrosione comunemente trovato nelle leghe di alluminio, cioè al *pitting*, perché le irregolarità dei pori rappresentano i siti di nucleazione per tale attacco.

Una seconda caratteristica che incide sul comportamento a corrosione sono i caratteristici limiti dei *molten pool*, conformazioni semicircolari come mostrato in **Figura 2.3**[5]. Questi siti sono ottimali per lo sviluppo dei *pit*, perché hanno una maggior concentrazione di difetti rispetto alle zone centrali, ad esempio maggior concentrazione di pori e di stress residui. Le differenze nella microstruttura saranno poi spiegati meglio nella *Sezione III*.

Infine, la terza importante caratteristica che influenza la corrosione è la rugosità superficiale, la quale è più elevata nei prodotti generati con questa tecnologia rispetto ai metodi tradizionali. La rugosità aumenta notevolmente la propensione alla corrosione dato che una superficie irregolare, con i difetti, produce la scomposizione del film di passivazione lasciando scoperte certe aree, che subiscono un attacco corrosivo. Numerosi studi condotti [12, 13, 14] hanno dimostrato questo effetto.

[5] Immagine presente nella Sezione 2.2 del testo principale di questa tesi.

II. MATERIALI E METODI

II-a Presentazione e preparazione dei campioni

Come prima accennato, la lega di alluminio utilizzata in questa tesi è conosciuta come AlSi10Mg. La sua composizione, sia nel campione *cast* che *as-printed* è la medesima; mentre la composizione chimica delle polveri utilizzate per produrre la forma AP è specificata nella **Tabella 4.1**[6] e sono ottenute mediante atomizzazione in gas [15].

Per la fabbricazione dei campioni AP è stata utilizzata la macchina EOS M 290, che possiede un laser Yb-fibre di potenza 400 W, a una velocità di scansione di 1300 mm/s e distanza tra tracce di 0.19 mm. Ogni letto di polvere ha uno spessore di 30 μm mentre la strategia di scansione consiste in una rotazione di 67º tra un *layer* e quello successivo. I campioni così prodotti hanno dimensioni di 20 mm di lato, come riportato in **Figura 4.1**[7].

I provini HT corrispondono ai provini AP che hanno subito un trattamento termico, con l'obbiettivo di ridurre le tensioni residue naturalmente prodotte dal processo SLM. Il trattamento termico consiste in un riscaldamento lento a 200ºC/h per 90 minuti. Una volta raggiunti i 300ºC si mantiene per 2 ore, dopodiché subisce un raffreddamento graduale in forno.

Per ogni campione AP e HT sono stati generati due campioni diversi che rappresentano diversi piani, uno che rappresenta il piano parallelo (XZ) e l'altro che rappresenta il piano perpendicolare (XY) alla direzione di fabbricazione (Z) come mostrato in **Figura 4.3**[8]. Inoltre, la designazione per ogni campione usato in questa tesi è riassunta nella **Tabella 4.2**[9].

Prima di essere utilizzati nelle prove elettrochimiche ogni campione deve essere sottoposto ad operazioni di condizionamento. Inizialmente, i provini cubici di 20 mm di lato sono stati sezionati con una troncatrice in maniera da produrre i campioni XZ e XY. A seguito di questo sono stati inglobati in una resina epossidica fissando al campione un filo con una colla d'argento, assicurando così il passaggio continuo della corrente. Il risultato finale è mostrato in **Figura 4.4**[10]. Successivamente si lucida manualmente ogni campione tramite la lucidatrice Mecatech 234, utilizzando carte abrasive con numero di grana crescente. Infine si procede con il bagno ultrasonico per ottenere una pulizia altamente efficace della superficie del campione. Il campione viene immerso in un Becker contenente una soluzione di metanolo, il quale viene poi immerso nel bagno d'acqua come esposto in **Figura 4.6**[11].

---

[6] Tabella presente nella Sezione 4.1 del testo principale di questa tesi.

[7] Immagine presente nella Sezione 4.1 del testo principale di questa tesi.

[8] Immagine presente nella Sezione 4.2 del testo principale di questa tesi.

[9] Immagine presente nella Sezione 4.2 del testo principale di questa tesi.

[10] Immagine presente nella Sezione 4.3 del testo principale di questa tesi.

[11] Immagine presente nella Sezione 4.3 del testo principale di questa tesi.

II-b Prove elettrochimiche

Tutte le prove elettrochimiche sono state eseguite utilizzando una cella elettrochimica composta da tre elettrodi, come mostrato in **Figura 4.7**[12], immersi in una soluzione 0.6 M di cloruro di sodio. L'elettrodo di riferimento (RE) è ad Ag/AgCl, mentre il controelettrodo (CE) è costituito da un filo di platino e l'elettrodo di lavoro (WE) costituisce il campione inglobato.

Prima di eseguire le prove sia di polarizzazione che d'impedenza si effettua la misura del potenziale di libera corrosione (*Open Circuit Potential* - OCP) per sessanta minuti fino alla sua stabilizzazione. Questo permette il raggiungimento dello stato stazionario.

La prova di polarizzazione consiste nella variazione del potenziale tra il WE e l'RE mentre si registra la risposta nella corrente che passa tra il WE e il CE, come riportato in **Figura 4.8**[13] [16]. La scansione è stata impostata a 0.5 mV/s e il potenziale fatto variare tra OCP – 1.0000 V e OCP + 0.7000 V.

Per il monitoraggio dello strato protettivo si utilizza la prova EIS, la quale comporta l'applicazione di un potenziale sinusoidale al WE e la misura della corrente alternata, la quale avrà la stessa frequenza (ω) ma una fase diversa (φ) dal potenziale [17, 18]. Tramite un analizzatore della risposta in frequenza è possibile ottenere questi dati variabili nel tempo, così come il valore dell'impedenza definito con l'equazione (1.63)[14]. I valori di frequenza sono stati compresi tra 10^{-2} e 10^{5} Hz, mentre l'ampiezza della tensione applicata era 0.1 V. Le misure di EIS sono state eseguite dopo 1, 3, 5 ore e una volta al giorno per sette giorni (168 ore).

[12] Immagine presente nella Sezione 4.4 del testo principale di questa tesi.

[13] Immagine presente nella Sezione 4.4 del testo principale di questa tesi.

[14] Equazione presentata nella Sezione 1.4 del testo principale di questa tesi.

III. RISULTATI SPERIMENTALI

III-a Studio della microstruttura

Inizialmente risulta importante studiare le principali caratteristiche della microstruttura del campione cast, così da poter capire in seguito quelle che sono cambiate per il campione *as-printed* e per quello *heat-treated*.

Si presenta una micrografia, effettuata con il FESEM, nella **Figura III.1** dove la fase primaria α-Al si distingue per le formazioni arrotondate, alcune di cui sono più allungate con lunghezze di 37 ± 12 µm, mentre altre sono più rotonde con diametro di 16 ± 4 µm. La fase eutettica di silicio si presenta ad alti ingrandimenti mediante due tipi di conformazioni discontinue: principalmente forma elementi arrotondati con diametro inferiore al micrometro, ma anche si osservano delle conformazioni più allungate raggiungendo lunghezze di 12 µm.

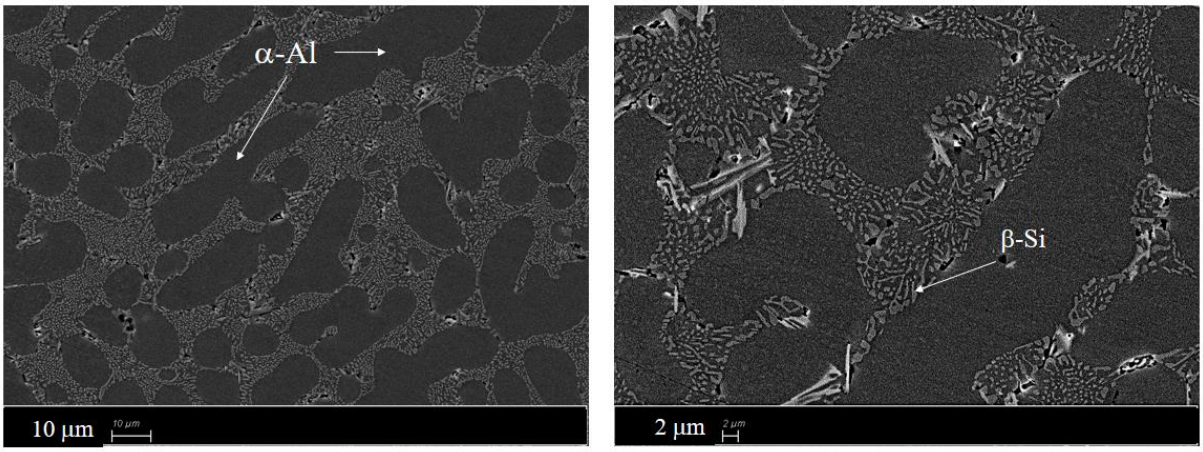

Figura III. 1: Microstruttura del campione cast a bassi (a) ed alti (b) ingrandimenti.

Per quanto riguarda il campione *as-printed*, i caratteristici *molten pool* a bassi ingrandimenti sono evidenziati nella **Figura 5.3**[15]. Nel piano XZ le profondità dei *molten pool* è di 115 ± 15 µm e la lunghezza di 142 ± 68 µm. Nel piano XY è possibile evidenziare la strategia di scansione dato che anche gli strati posizionati sotto si riescono a vedere. Alcuni ricercatori [19] hanno collegato questo effetto alle diverse profondità raggiunte nelle varie tracce fuse, che creano delle diverse sovrapposizioni.

Analizzando la microstruttura all'interno di ogni *molten pool*, si trovano tre zone con diverse caratteristiche come mostrato in **Figura III.2**. La prima zona, segnalata con il numero 1 corrisponde alla zona centrale di ogni *molten pool*, la quale presenta una struttura molto fina. Questo vuol dire che la fase α-Al, regione più scura, forma strutture cellulari di diametro molto piccolo, di 0.48 ± 0.16 µm e di forma tondeggiante per il piano perpendicolare (b).

[15] Immagine presente nella Sezione 5.1 del testo principale di questa tesi.

Mentre nel piano parallelo (a) la configurazione risulta molto più allungata e con uguale distanza tra due bracci dendritici. Che delimita questa fase primaria si ha una rete di silicio eutettico, regione più chiara, la quale sarà molto più distanziata nella regione 2 e ancora di più nella 3 rispetto alla regione 1. Anche se la maggior concentrazione di silicio si trova in questa rete, non si deve dimenticare che la fase α è soprassatura di silicio.

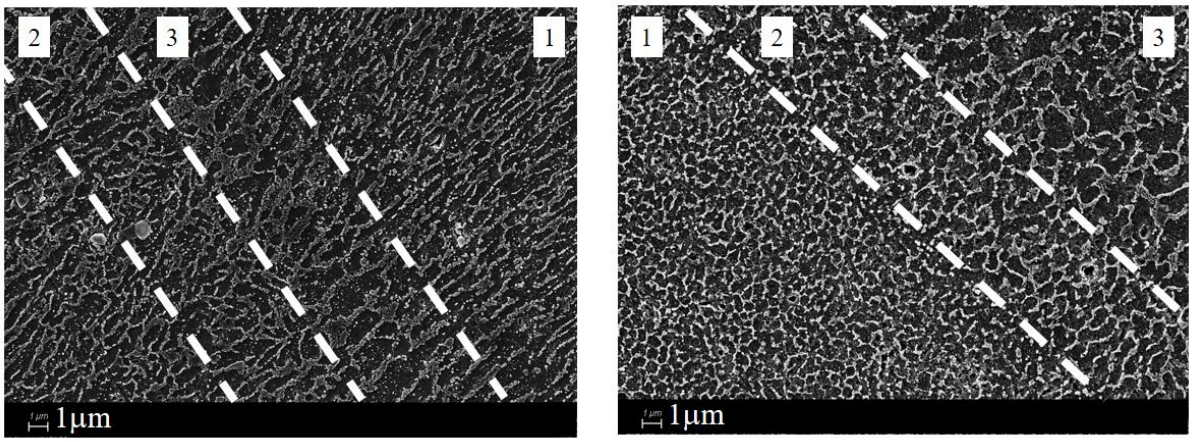

a) b)

Figura III. 2: Microstruttura dei campioni *as-printed* per il piano a) parallelo e b) perpendicolare.

La seconda area indicata con il numero 2 corrisponde alla zona termicamente alterata (*Heat Affected Zone* - HAZ) ed è quella influenzata dalla fusione di una traccia eseguita di fianco. La zona 3 rappresenta il bordo tra un *molten pool* e quello adiacente ed è quello che ha la maggior dimensione dendritica. Anche in questo caso la morfologia è molto più allungata per i campioni XZ, i quali hanno una separazione di 1.24 ± 0.24 µm, mentre nel piano perpendicolare hanno una separazione di 1.84 ± 0.88 µm. Inoltre, non è solo una maggior separazione che si vede in quest'ultimo piano ma anche una maggiore discontinuità nella rete di silicio.

Queste differenze nelle diverse dimensioni delle tre zone sono dovute ai diversi processi di raffreddamento che subiscono. Mentre nel centro di ogni *molten pool* si produce un rapido raffreddamento, senza che sia influenzato da quelli adiacenti, la HAZ subisce un lieve riscaldamento mentre si fondono le tracce vicine. Questo sommato al fatto che alte velocità di raffreddamento generano una microstruttura più fina [20] spiega accuratamente la microstruttura evidenziata.

Per quanto riguarda i campioni trattati termicamente, la microstruttura risultante è esposta nella **Figura III.3**. La principale caratteristica evidenziata è la perdita nella continuità della rete di silicio e la conseguente formazione dei precipitati poligonali circondati dalla fase ricca di alluminio [21, 22]. Secondo alcuni studi [23] parte del silicio presente nella fase sovrasatura di alluminio viene allontanata, andando a formare parte degli eventuali precipitati di Si (*coarser* Si) così come Si libero (*finer* Si). La quantità di *finer* Si raggiunge quasi quella che caratterizza il campione cast, mentre il *coarser* Si si trova principalmente nelle zone di

overlapping tra tracce adiacenti. Questo fenomeno è mostrato schematicamente nella **Figura 3.9**[16] e sperimentalmente accertato nella **Figura 5.6**[17].

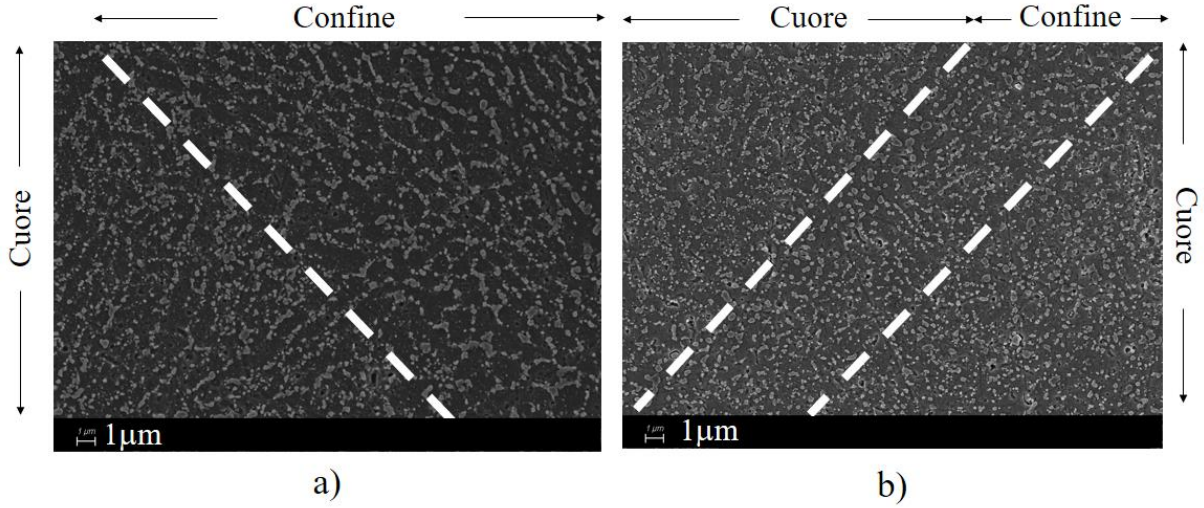

Figura III. 3: Microstruttura dei campioni *heat-treated* del piano a) parallelo e b) perpendicolare.

Le dimensioni dei precipitati sono 160 ± 64 nm per la superficie perpendicolare, mentre è 333 ± 166 nm in quelle parallele. Inoltre, diverse densità di particelle di Si sono evidenziate tra il cuore di ogni *melt pool* e il loro confine, come mostrato nella precedente figura, essendo maggiore in quest'ultima zona. Invece nella zona centrale si vede una maggiore uniformità nella dispersione di tali particelle, così come una minore dimensione. Per il campione parallelo si vede una configurazione molto più simile a quella originale *as-printed,* che ancora segue la conformazione allungata dei precedenti grani. Paragonato al piano perpendicolare, i precipitati nel piano parallelo formano una microstruttura più continua e meno fina.

III-b Risultati delle prove di polarizzazione

Come accennato nella *Sezione II.b*, è stato inizialmente determinato il valore di OCP, il quale ha presentato valori nei dintorni di -0.7 $V_{Ag/AgCl}$ per tutti i campioni. Tale determinazione è stata effettuata durante 60 minuti per assicurare il raggiungimento dello stato stazionario.

Per ogni campioni sono state fatte tre ripetizioni, ottenendo le caratteristiche curve di potenziale rispetto alla densità di corrente (normalizzata con ogni valore di superficie esposta). Questi andamenti sono mostrati nelle **Figure 5.8 a 5.10**[18]. In base a questi dati è stata fatta l'analisi di Tafel per poter determinare i consueti parametri: il potenziale di

[16] Immagine presente nella Sezione 3.6 del testo principale di questa tesi.

[17] Immagine presente nella Sezione 5.1 del testo principale di questa tesi.

[18] Immagini presenti nella Sezione 5.2 del testo principale di questa tesi.

corrosione (E_{corr}) e la densità di corrente di corrosione (i_{corr}), specificati nella **Tabella 5.1**[19]. La **Figura III.4** esibisce i risultati ottenuti.

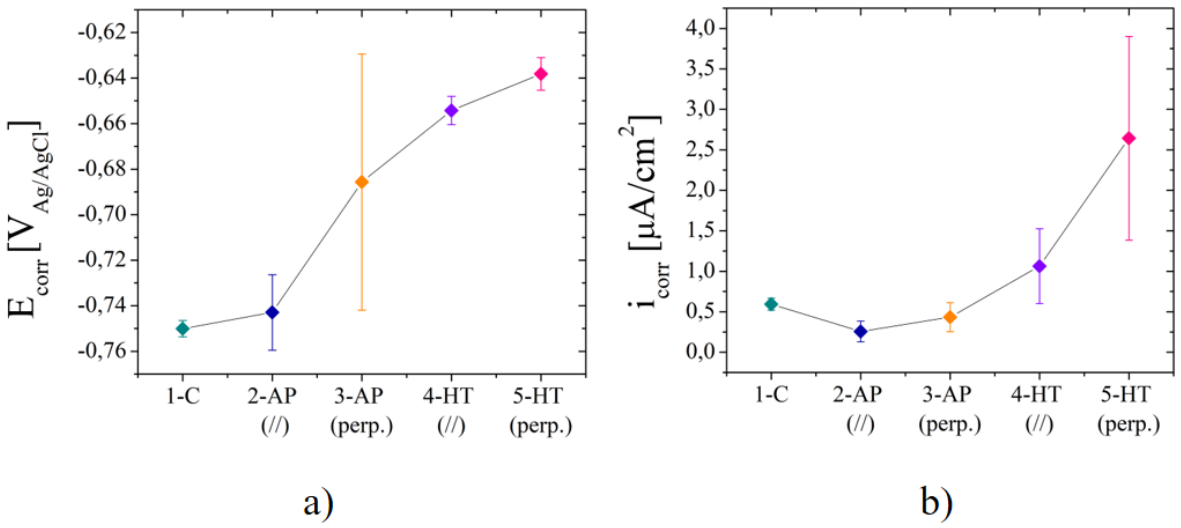

Figura III. 4: Paragone dei risultati ottenuti dei valori di E_{corr} e i_{corr}.

Analizzando i valori di E_{corr} si vede che la corrosione è più favorita nei campioni *cast*. Questo è dovuto agli intermetallici di magnesio e al maggior contenuto di silicio libero che aumentano considerabilmente la predisposizione all'attacco corrosivo [13, 14, 24]. Invece i campioni AP, anche avendo la stessa composizione, non presentano praticamente la formazione di fasi secondarie di Mg mentre il contenuto di silicio libero è provocando che la matrice α sia soprassatura di Si. Questi effetti sono dovuti al rapido processo di riscaldamento e raffreddamento caratteristico del processo *additive*. Inoltre, i campioni così prodotti sono caratterizzati da una microstruttura molto più fina di alluminio soprassaturo circondata da una rete di silicio eutettico [25], la quale influisce positivamente nella resistenza alla corrosione. I campioni HT sono quelli meno soggetti a corrosione, dal punto di vista termodinamico, dato che il tipo di corrosione che loro presentano è uniforme. Mentre per i campioni AP la corrosione è localizzata nei confini dei *molten pool* [14].

La velocità di corrosione è direttamente proporzionale ai valori di i_{corr}. I campioni *cast* presentano valori di i_{corr} maggiori rispetto agli AP ma minore degli HT. In primo luogo, la maggiore i_{corr} dei campioni *cast* è collegata alla sua microstruttura, la quale causa una rottura del film passivo nelle zone eterogenee degli intermetallici di Fe e Mg [26]. Le fasi di Fe diventano catodiche rispetto ai dintorni, potenziando la dissoluzione della matrice α, mentre le fasi di Mg diventano anodiche rispetto alla matrice α fornendo dei siti opportuni a subire attacco corrosivo. Nei campioni AP invece la microstruttura con dimensioni di grano minori aumenta la resistenza alla corrosione, sommata alla minore quantità di silicio libero, che ora forma parte della matrice α-Al, e la quasi non apprezzabile quantità dell'intermetallico Mg_2Si. Questa maggior concentrazione di Si nella fase primaria diminuisce la differenza di potenziale tra la matrice anodica e le particelle di silicio catodiche, diminuendo così la velocità di

[19] Immagine presente nella Sezione 5.2 del testo principale di questa tesi.

corrosione. Questo effetto è pero annullato per i campioni HT, i quali avranno una velocità di corrosione maggiore dovuta a non solo la maggior percentuale di silicio libero [23] e alla formazione di singoli precipitati di Si ma anche alla presenza della fase Mg_2Si. La conseguente diminuzione nella percentuale di Si nella matrice di alluminio aumenta la differenza di potenziale tra la fase più nobile e quella di Al, aumentando così la i_{corr}. Quest'ultima è ulteriormente aumentata per la presenza dei "microanodi" di magnesio che potenziano la corrosione nei campioni *heat-treated*.

Per quanto riguarda le differenze tra i piani paralleli e perpendicolari, diverse analisi sono state realizzate sia per i campioni AP che HT. Nel primo caso si deve tenere conto che i siti più adatti per l'attacco corrosivo sono rappresentati dai confini dei *molten pool* e dai difetti come ad esempio la porosità [27]. Seguendo queste analisi i piani paralleli dovrebbero essere quelli più soggetti a corrosione, data la loro microstruttura presentata in **Figura 5.3**[20]. Ma questa tesi non è supportata dai risultati sperimentali, per questa ragione è necessario effettuare un'analisi più approfondita sulla zona più soggetta a corrosione. Di conseguenza, si può affermare che una rete di silicio più discontinua nei bordi dei *molten pool* (zona 3 nella **Figura III.2**) e con separazioni più elevate genera una maggior predisposizione all'attacco corrosivo sulle superfici XY. Al contrario, una matrice più allungata e continua dei piani XY genera una maggior resistenza alla corrosione.

In relazione ai campioni HT una maggior tendenza alla corrosione si è anche vista per i piani XY. Questo può essere spiegato mediante le differenze constatate tra le due microstrutture, già precedentemente descritte, dove una configurazione meno interrotta e più simile a quella precedente *as-printed*, come evidenziata nei piani paralleli, influisce positivamente nella resistenza alla corrosione. Una maggior dimensione dei precipitati Si può anche essere legata al miglior comportamento sopracitato. Invece, una distribuzione più uniforme di precipitati più piccoli sembra di diminuire la resistenza alla corrosione.

III-c Risultati delle prove EIS

Quando una lega di alluminio è immersa in un ambiente corrosivo, come è quello di una soluzione 0.6 M di NaCl, questa forma uno strato passivante formato da due *layers* come mostrato schematicamente nella **Figura 3.1**[21]. Le prove EIS sono condotte con il principale obbiettivo di studiare le proprietà di questo strato superficiale, collegando la sua risposta al potenziale sinusoidale applicato con un circuito elettrico equivalente. Questo deve tenere conto dei due strati, uno più compatto e formato direttamente sopra la superficie esposta del metallo (A) ed un altro più poroso (B) formato sopra lo strato precedente. Di conseguenza il circuito presentato nella **Figura III.5** descrive correttamente questo *layer* includendo la resistenza dell'elettrolita, *Rs*, in serie e i due loop A e B dei due strati. Risulta importante notare che questo circuito è utilizzato di solito in diverse ricerche [13, 27, 28].

[20] Immagine presente nella Sezione 5.1 del testo principale di questa tesi.

[21] Immagine presente nella Sezione 3.2 del testo principale di questa tesi.

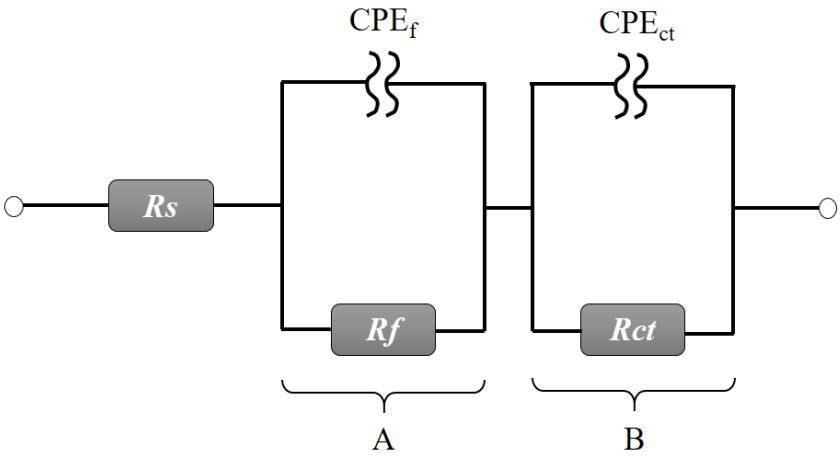

Figura III. 5: Circuito elettrico equivalente dello strato passivante e la resistenza dell'elettrolita *Rs*.

I parametri *Rf* e *Rct* sono rispettivamente la resistenza del film passivo e la resistenza al trasferimento di carica. Le sigle *CPE* corrispondono al *Constant Phase Electrode*, il quale è equivalente a un capacitore ma tiene conto della non idealità che possiede il film [29]. L'impedenza di ogni *CPE* può essere calcolata con l'equazione (5.2)[22].

I dati ricavati dalle diverse prove EIS possono essere rappresentati mediante due tipi di grafici: Bode e Nyquist. Nonostante le misure sono fatte dopo 1, 3, 5 ore e ogni giorno per 7 giorni (168 ore), solo le ore più significative saranno qui presentate dato che dalla **Figura 5.15**[23] è possibile vedere come i dati dalle ore 24 a 168 sono abbastanza simili. Per questo motivo si farà riferimento al comportamento del film dopo 1, 24 e 168 ore d'immersione, rappresentando quest'ultimo valore come quello più prossimo al raggiungimento dello stato stazionario.

I grafici di Bode sono illustrati nella loro totalità in **Figura 5.17**[24], dove i punti sparsi sono i singoli dati sperimentali mentre le linee continue sono i risultati delle diverse modellizzazioni fatte con il circuito della **Figura III.5**. Nella successiva **Figura III. 6** si presentano i risultati delle modellizzazioni della prima e dell'ultima ora d'immersione.

Come principale andamento in tale figura, il modulo dell'impedenza a bassa frequenza che rappresenta la resistenza del film passivo è sempre maggiore nelle prime ore rispetto alla fine della prova. Questo è spiegato dal fatto che nei momenti prima di essere immersa la lega esposta all'aria forma uno strato passivo, il quale fornirà di una maggiore protezione appena immerso nella soluzione di NaCl. Man mano che aumenta il tempo d'immersione, il film raggiunge progressivamente la sua configurazione stazionaria, diminuendo a sua volta il modulo dell'impedenza. I valori ad alte frequenze invece sono sempre molto simili, questo perché rappresentano la resistenza dell'elettrolita (*Rs*), la quale rimane costante nel trascorso della prova. Questa tendenza è anche verificata nei parametri presentati in **Tabella III.1**. Analogamente, se si paragonano i comportamenti dopo 1 ora e dopo 168 ore, come

[22] Equazione presente nella Sezione 5.3 del testo principale di questa tesi.

[23] Immagine presente nella Sezione 5.3 del testo principale di questa tesi.

[24] Immagine presente nella Sezione 5.3 del testo principale di questa tesi.

evidenziato nella figura precedente, si vede che inizialmente tutti i campioni avevano caratteristiche simili nelle frequenze intermedie (tra 10^0 e 10^3 Hz) e diventarono più dissimili tra AP e HT nei momenti finali d'immersione, il che evidenzia le caratteristiche finali dello strato.

Per quanto riguarda i grafici Bode ϕ rispetto a f a 168 ore, i picchi dei campioni HT si presentano a frequenze più alte rispetto a quelli degli AP, per cui minori tempi caratteristici ($\tau_D \sim 1/f_C$) si attribuiscono a questi campioni. Secondo alcune ricerche [27] un minore tempo caratteristico è correlato con una maggior tendenza alla dissoluzione della matrice α-Al nelle vicinanze delle particelle di Si. Di conseguenza si verificano le velocità di corrosione più alte nei campioni *heat-treated*. È importante notare che queste curve dovrebbero esibire due picchi corrispondenti ai due tempi caratteristici derivanti dal circuito equivalente. Nella prima ora d'immersione di solito non si manifesta, infatti la curva è sempre più allungata. Nelle successive ore si dovrebbero comunque differenziare i due picchi che, secondo alcuni studi [27, 30], possono essere sovrapposti in maniera che solo un picco si riesca a vedere.

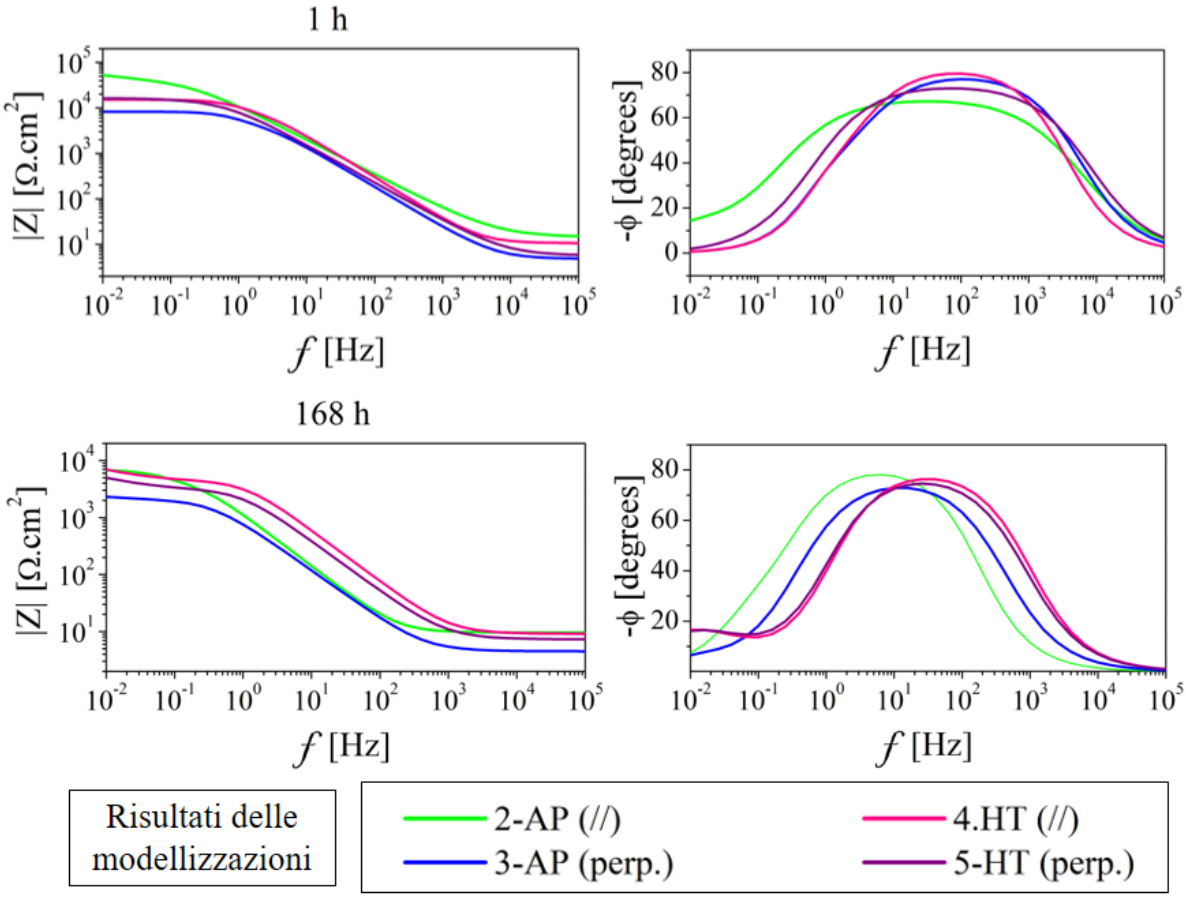

Figura III. 6: Grafici Bode corrispondenti ai risultati delle modellizzazioni fatte.

Nei grafici Nyquist, presentati completamente nella **Figura 5.20**[25], ciò che è possibile distinguere è la resistenza del film passivo analizzando il diametro dei semicerchi. Nella prima ora di test si trovano dei diametri molto più elevati rispetto alle seguenti ore. Questo ha

[25] Immagine presente nella **Sezione 5.3** del testo principale di questa tesi.

riscontro con quanto è stato spiegato precedentemente sul modulo dell'impedenza. Inoltre, i due cerci adiacenti non sono evidenziate in quest'ora ma nelle successive 24 e 168 ore, in modo più evidente per i campioni HT. Confrontando con i risultati delle prove di polarizzazione, nella prima ora i campioni paralleli non presentano sempre cerchi più grandi rispetto quelli perpendicolari, come invece succede nelle ore successive. Questo evidenzia ancora una volta che lo strato passivante caratteristico di ogni campione comincia a evidenziarsi solo dopo alcuni giorni d'immersione.

Le caratteristiche più importanti dei test EIS sono evidenziate al meglio quando si analizzano i parametri risultanti dai processi di modellizzazione. Con questo obbiettivo si presenta la **Tabella III.1** riassuntiva. Basandoci sui lavori di ricerca [30], il valore di capacità (definito come *CPEf* e *CPEct*) è inversamente proporzionale allo spessore dello strato passivo. Seguendo questa relazione, è possibile contemplare gli effetti del trattamento termico nello spessore dello strato poroso, il quale è più elevato nei campioni HT rispetto a quello degli AP. Tale osservazione è derivata dai valori di *CPEct* per le ore 24 e 168 i quali sono sempre minori nei campioni HT. Parallelamente, gli spessori dello strato compatto interno è sempre maggiore nei campioni AP, anche con l'eccezione della prima ora. Questi risultati sono in accordo con altri studi di ricerca [31] per i quali lo strato compatto dei campioni *heat-treated* ha mostrato una qualità più elevata nella prima ora d'immersione per la stessa ragione esposta precedentemente.

Tabella III. 1: Risultati dei parametri EIS risultanti dai processi di modellizzazione.

Sample	*Rs* [$\Omega.cm^2$]	*Rf* [$\Omega.cm^2$]	*Rct* [$\Omega.cm^2$]	*CPEf* [$s^n/(\mu\Omega.cm^2)$]	n_1	*CPEct* [$s^n/(\mu\Omega.cm^2)$]	n_2
2-AP							
1h	14.4	30624.0	40400.0	314.8	0.7180	21.8	0.7726
24h	25.6	8206.4	4300.8	462,3	0.7000	38,7	0.904
168h	9.6	4401.6	2612.8	513.1	0.8929	226.8	0.9370
3-AP							
1h	4.8	3672.0	4603.0	23.7	0.8720	49.5	0.9987
24h	5	3398.0	2312.0	41.7	0.8522	2206.0	0.7500
168h	4.5	2109.0	395.9	235.1	0.8665	28610.0	0.9087
4-HT							
1h	10.6	9176.2	6040.5	23.6	0.9790	13.1	0.9061
24h	9.1	7448.0	6578.6	2117.1	0.7000	22.2	0.8447
168h	9.1	6362.7	4309.2	1691.4	0.7200	39.4	0.9150
5-HT							
1h	5.7	15381.9	961.5	20.5	0.8338	1137.9	0.9100
24h	6.5	8197.2	4656.7	1120.3	0.7900	25.4	0.9031
168h	7.3	4505.2	3003.5	2116.1	0.700	65.4	0.9011

Questi risultati inerenti allo spessore vanno anche studiati assieme ai valori di resistenza, in quanto in alcuni studi [32] viene attribuita una velocità di corrosione più elevata a minori valori di resistenza. In tutti i casi le resistenze *Rf* e *Rct* sono più alte nella prima ora d'immersione diminuendo progressivamente nelle ore successive nella quasi totalità dei casi. Questo è analogo a quanto mostrato nelle rappresentazioni Bode. In alcuni campioni, come 2-AP e 5-HT, i valori di *Rf* sono addirittura superiori di un ordine di grandezza. Per quanto riguarda i campioni *as-printed* la resistenza *Rct* è inizialmente superiore a quella interna *Rf*, a differenza di quelli *heat-treated* che presentano il caso opposto. Tuttavia, con il raggiungimento dello stato stazionario, i valori di resistenza *Rf* diminuiscono per tutti i casi per la progressiva corrosione. Invece la resistenza *Rct* ha un andamento diverso: per i campioni AP diminuisce progressivamente, mentre per gli HT aumenta fino alle 24 ore e poi diminuisce. Ciò potrebbe indicare che mentre lo strato poroso esterno diventa più spesso anche la sua resistenza aumenta fino a un certo punto. Dopodiché l'attacco corrosivo diventa più aggressivo e la sua resistenza diminuisce.

Considerando la microstruttura che ha dato origine a le proprietà esposte dallo strato passivo, si constata che l'allontanamento del silicio dalla matrice α per formare dei singoli precipitati (*finer* e *coarser* Si) causa uno ispessimento dello strato poroso il quale presenta una resistenza crescente fino a 24 ore dopo immersione ma che diminuisce nelle successive ore. Al contrario, una rete di silicio più connessa fornisce siti micro-galvanici meno localizzati, generando quindi uno strato protettivo più spesso.

Confrontando i casi paralleli e perpendicolari degli stessi tipi di campione, ossia tra AP e tra HT, i piani perpendicolari mostrano continuamente capacità *CPEct* più elevate; il che suggerisce una resistenza alla corrosione più elevata dei piani paralleli rispetto a quelli perpendicolari. Analogamente, lo strato poroso esterno presenta resistenze superiori (*Rct*) nel caso XZ. Un andamento opposto è seguito dai valori *CPEf*, questo indica che i piani perpendicolari generano uno strato compatto più spesso rispetto a quello generato dai paralleli. Tuttavia, i corrispondenti valori di resistenza *Rf* in *as-printed* confermano che, anche se il *layer* interno è più sottile, possiede una resistenza più elevata fornendo quindi un rivestimento di qualità superiore. Per i campioni *heat-treated* le *Rf* non seguono questa tendenza dato che è maggiore nei piani perpendicolari. Ciò significa che quando si eseguono dei trattamenti termici sui campioni AM, lo strato poroso esterno contribuisce principalmente alla resistenza alla corrosione, in quanto quello generato dai piani XZ è più spesso e più resistente alla corrosione. Tale affermazione è in accordo con certi articoli [33] che propongono lo strato poroso come il fattore decisivo nella resistenza all'attacco corrosivo.

Seguendo il confronto fra tali piani, il piano XY sia nel caso AP che HT presenta una microstruttura che contribuisce alla formazione di strati porosi più sottili e meno resistenti rispetto ai piani XZ. Questo è legato, quindi, alla maggior discontinuità che si presenta nei confini dei *molten pool* e alle dimensioni di grano minore nella zona centrale dei campioni AP. Parallelamente, uno strato poroso con proprietà meno protettive è legato alla configurazione più raffinatamente distribuita dei piani XY. Pertanto, le microstrutture che mostrano una rete di silicio più continua possono certamente migliorare la qualità dello strato passivo formato e così aumentare la resistenza alla corrosione, sia nei campioni AP che HT.

IV. CONCLUSIONI

Durante lo sviluppo di questa tesi si è studiato il potenziale impiego delle tecniche AM nel settore automobilistico, facendo particolare riferimento alle proprietà di corrosione che determinano parte delle prestazioni che forniscono tali leghe. Le motivazioni che hanno portato all'utilizzo delle tecnologie AM al posto di quelle tradizionali sono state trovate in seguito alle analisi eseguite in questa tesi. Queste motivazioni sono legate alla loro flessibilità nella produzione, il potenziale di realizzare parti che possiedono una geometria molto complessa e la riduzione degli scarti di materiale.

Dai numerosi test sperimentali realizzati così come dalla conseguente analisi dei dati, lo studio del comportamento corrosivo della lega AlSi10Mg si è rivelato essere uno studio complesso e legato a moltissimi altri aspetti dello studio dei materiali. Esso ha compreso non solo le diversi prove elettrochimiche ma anche la caratterizzazione delle microstrutture assieme ad eventuali constatazioni provenienti da altre ricerche per completare alcune interpretazioni.

Il punto di partenza di questo studio è stato la comprensione delle caratteristiche di ciascuna delle microstrutture della lega. I campioni cast sono caratterizzati da una fase ricca di alluminio con conformazione arrotondata e con diametro medio di 16 ± 4 μm. Lungo i suoi confini si presenta una fase di silicio con formazione anche arrotondata ma molto più fina. I campioni AM presentano nei piani paralleli le caratteristiche conformazioni semicircolari dei *molten pool*, mentre la strategia di scansione (rotazione di 67º tra *layer* e *layer*) è stata chiaramente identificata nel piano perpendicolare. La microstruttura più fina è stata resa studiabile mediante l'utilizzo di maggiori ingrandimenti dei *molten pool* ed è composta da una matrice cellulare di α-Al (diametro non maggiore di 3 μm) che è soprassatura di silicio ed è delimitata dal network di silicio eutettico. Il piano XY ha presentato morfologie quasi arrotondate mentre nelle superfici XZ i grani sono più allungati. I campioni sottoposti a trattamento termico hanno evidenziato una microstruttura totalmente diversa, in quanto la fase continua di silicio è diventata discontinua formando delle particelle poligonali isolate. Tuttavia, una tendenza più allungata è stata osservata anche nella faccia parallela.

Per quanto riguarda i risultati delle prove di polarizzazione, i campioni *as-printed* hanno presentato un E_{corr} meno negativo rispetto al campione *cast*, mentre quelli trattati termicamente hanno evidenziato i valori più alti. Ciò indica che l'attacco corrosivo è termodinamicamente più favorito nei campioni *cast* a causa della microstruttura con maggiore dimensione dei grani così come alla presenza delle diverse fasi secondarie contenenti Si e Mg. Esse influiscono nella rottura del film passivo che favorisce la corrosione *pitting*. Nei campioni *as-printed* invece queste fasi non sono presenti in quantità apprezzabili, questo è dovuto al processo di riscaldamento e raffreddamento rapido che permette una maggiore solubilità dei soluti nella matrice α. I campioni *heat-treated* sono ancora meno favoriti, dal punto di vista termodinamico, a subire corrosione dato l'elevato spessore dello strato poroso generato (condizione accertata nei risultati EIS) oltre a presentare la tipica corrosione generalizzata. Questo comportamento è legato alla configurazione di particelle di silicio distribuite nella matrice di alluminio che presentano i campioni HT.

Dal punto di vista cinetico, le superfici parallele hanno presentato una velocità di corrosione inferiore a quelli perpendicolari, sia per i campioni AP che per quelli HT. I parametri delle modellizzazioni EIS hanno confermato questo andamento per i campioni AP tramite i valori delle resistenze *Rf* e *Rc*, le quale sono più elevate per i piani paralleli. In questi si genera uno strato passivo più protettivo come risultato di una microstruttura più allungata e

più continua nei bordi dei *molten pool*. Parallelamente è stato determinato che il principale fattore che migliora la resistenza alla corrosione nei campioni HT è la formazione di uno strato poroso esterno più spesso (*CPEct* minore) e più resistente. Inoltre, sui piani XZ lo strato passivo ha presentato proprietà maggiormente protettive come risultato di una distribuzione di silicio più concentrata e più simile a quella originale *as-printed*.

Una particolarità molto interessante è stata trovata nei parametri EIS della prima ora d'immersione: nei campioni HT il film passivo ha evidenziato uno strato interno più spesso rispetto a quello esterno, mentre nel caso AP lo strato esterno era il più spesso. Con il passare del tempo e il raggiungimento della conformazione finale si denota la crescita dello strato poroso nei campioni HT e dello strato compatto nei campioni AP. Prendendo in considerazione le resistenze *Rf* e *Rct*, entrambe sono risultate più alte nella prima ora rispetto alle successive per i campioni AP, mentre per gli HT solo la *Rf* seguiva l'andamento prima citato. Questo è dovuto al film passivo che si è generato quando il campione viene esposto all'aria (alcuni momenti prima dell'immersione). Tuttavia, nelle successive ore di immersione del campione AP nella soluzione, lo strato interno è diventato più spesso e più resistente rispetto allo strato poroso. Lo spessore dello strato esterno dei campioni HT è aumentato, così come la sua resistenza, fino a 24 ore. Dopodiché la resistenza è diminuita perché l'attacco corrosivo è diventato più aggressivo.

Questo andamento si riscontra anche nei diagrammi Bode che hanno evidenziato una diminuzione dell'impedenza dalla prima all'ultima ora d'immersione. Inizialmente il grafico |Z| rispetto *f* ha mostrato delle curve molto simili anche sovrapposte, invece si assiste ad una maggiore differenziazione delle curve verso la fine del test. Inoltre, i grafici Nyquist hanno evidenziato nelle ore 24 e 168 i due tempi caratteristici previsti dal circuito elettrico proposto, ossia due curve a forma di semicerchio. Ciò ha ulteriormente confermato che i parametri sui quali è più corretto fare delle analisi sono dopo 24 e 168 ore. Nelle rappresentazioni di Nyquist per le ore 24 e 168, si riscontrano diametri più elevati nei piani paralleli rispetto a quelli perpendicolari. Il che conferma la presenza di uno strato passivo più protettivo nei piani XZ. Inoltre, grazie ai grafici Bode, costanti di tempo più elevate sono state riscontrate per i campioni *as-printed* rispetto agli *heat-treated*. Questo comportamento ha ulteriormente verificato le maggiori velocità di corrosione nelle leghe HT.

Sulla base di questi risultati, e considerando che il silicio è più nobile della matrice α, una delle principali conclusioni che si possono trarre è che il tipo di distribuzione del silicio determina infine la risposta all'attacco corrosivo. Una struttura AP cellulare è considerata più omogenea e meno reattiva, dal punto di vista galvanico, rispetto alle singole particelle di silicio scollegate che caratterizzano i campioni trattati termicamente. L'allontanamento del silicio crea dei "microcatodi" i quali riducono notevolmente la resistenza dello strato passivo. Inoltre, la presenza della fase Mg_2Si è stata constata per i campioni HT, mentre che nei campioni AP non era praticamente apprezzabile. Questa fase secondaria di Mg rappresenta dei siti opportuni per subire attacco corrosivo, causando l'aumento della velocità di corrosione.

La determinazione delle pendenze di Tafel e i parametri di modellizzazione hanno fornito informazioni concordanti nella quasi totalità dei casi. Tuttavia, in altri casi sono emerse alcune discrepanze. Risulta allora opportuno considerare le limitazioni che si possono

presentare nelle prove elettrochimiche, come quelle esposte nell'ultima sezione del corpo principale di questa tesi[26].

Complessivamente, l'effetto negativo nella corrosione che conferisce il trattamento termico a 300ºC per due ore rimane una questione da superare. La sua applicazione è legata al miglioramento delle proprietà meccaniche, ma questo ha aumentato significativamente la velocità di corrosione. Una soluzione che può essere suggerita riguarda lo sviluppo di leghe di altre composizioni, come ad esempio l'uso di leghe di Al-Mg-Zn che presentano una resistenza meccanica, formabilità e capacità di resistere alla corrosione più elevate rispetto alle leghe cast Al-Si-Mg [34]. Un altro modo per mantenere le proprietà di corrosione nella lega AM e ridurre ancora le sollecitazioni residue comprende il riscaldamento delle piattaforme di costruzione durante il processo *additive* o addirittura l'ottimizzazione della strategia di scansione in maniera da ridurre le tensioni residue. Indipendente da quanto esposto, si potrebbero valutare altri processi di riduzione degli stress residui caratterizzando il loro comportamento a corrosione.

Un secondo argomento per sviluppi futuri riguarda l'ottimizzazione nella finitura superficiale dei pezzi fabbricati con la tecnologia additive. Questo perché tutte le prove elettrochimiche sono state sviluppate su superfici lucidate ed è ben nota la migliore resistenza alla corrosione che questo tipo di finitura conferisce rispetto a una superficie non lucidata. Inoltre tale processo di lucidatura non rappresenta una procedura fattibile da implementare nelle parti automobilistiche. Pertanto, un approccio più realistico per ridurre i difetti di superficie nelle parti AM merita future ricerche.

Un terzo argomento che ha diverse interpretazioni riguarda l'influenza della microstruttura nel comportamento a corrosione. Per questo motivo si suggerisce un approfondimento nello studio dei punti più soggetti a precipitazione delle fasi secondarie, così come una maggior conoscenza della loro esatta composizione chimica.

Infine, è di grande importanza sottolineare che lo studio del comportamento alla corrosione nelle potenziali parti automobilistiche, generate mediante processo AM, è solo uno dei tanti studi da effettuare prima di poter essere effettivamente incorporato nell'industria automobilistica. Tali studi supplementari comprendono principalmente la determinazione delle proprietà meccaniche che, insieme al comportamento alla corrosione, possono garantirne una migliore integrazione funzionale tra esse.

[26] Sezione 5.4 del testo principale di questa tesi.

BIBLIOGRAFIA

[1] Ducker Frontier (2019) 'Aluminum Content in European Passenger Cars', *European Aluminium*, p. 13. Available at: https://www.european-aluminium.eu/media/2714/aluminum-content-in-european-cars_european-aluminium_public-summary_101019-1.pdf (Accessed: 5 November 2020).

[2] Majeed, A. *et al.* (2021) 'A big data-driven framework for sustainable and smart additive manufacturing', *Robotics and Computer-Integrated Manufacturing*. Elsevier Ltd, 67(June 2020), p. 102026. doi: 10.1016/j.rcim.2020.102026.

[3] Patalas-Maliszewska, J. *et al.* (2020) 'Single Tracks as a Key Factor in Additive Manufacturing Technology-Analysis of Research Trends and Metal Deposition Behavior', *Materials*, 13(5), p. 23. doi: 10.3390/ma13051115.

[4] Djukanovic, G. (2018) *Latest Trends for Aluminium Demand in Automotive Industry*. Available at: https://www.spotlightmetal.com/latest-trends-for-aluminium-demand-in-automotive-industry-a-736213/ (Accessed: 5 November 2020).

[5] Karayel, E. and Bozkurt, Y. (2020) 'Additive manufacturing method and different welding applications', *Journal of Materials Research and Technology*. Korea Institute of Oriental Medicine, 9(5), pp. 11424–11438. doi: 10.1016/j.jmrt.2020.08.039.

[6] ISO/ASTM International (2017) 'BSI Standards Publication Additive manufacturing — General principles — Terminology (ISO/ASTM 52900:2015)', pp. 1–19.

[7] Yap, C. Y. *et al.* (2015) 'Review of selective laser melting: Materials and applications', *Applied Physics Reviews*, 2(4). doi: 10.1063/1.4935926.

[8] Yadroitsev, I. and Smurov, I. (2010) 'Selective laser melting technology: from the single laser melted track stability to 3D parts of complex shape', 5(2), pp. 551–560. doi: 10.1016/j.phpro.2010.08.083.

[9] Huang, L. *et al.* (2018) 'Effect of magnesium content on keyhole-induced porosity formation and distribution in aluminum alloys laser welding', *Journal of Manufacturing Processes*. Elsevier, 33(January), pp. 43–53. doi: 10.1016/j.jmapro.2018.04.023.

[10] Yan, C. *et al.* (2015) 'Microstructure and mechanical properties of aluminium alloy cellular lattice structures manufactured by direct metal laser sintering', *Materials Science and Engineering A*. Elsevier, 628, pp. 238–246. doi: 10.1016/j.msea.2015.01.063.

[11] Kong, D. *et al.* (2019) 'Corrosion of metallic materials fabricated by selective laser melting', *npj Materials Degradation*. Springer US, 3:24. doi: 10.1038/s41529-019-0086-1.

[12] Cabrini, M. *et al.* (2016) 'Corrosion resistance of direct metal laser sintering AlSiMg alloy', *Surface and Interface Analysis*, 48(8), pp. 818–826. doi: 10.1002/sia.5981.

[13] Cabrini, M. *et al.* (2016) 'Evaluation of corrosion resistance of Al-10Si-Mg alloy obtained by means of Direct Metal Laser Sintering', *Journal of Materials Processing Technology*. Elsevier B.V., 231, pp. 326–335. doi: 10.1016/j.jmatprotec.2015.12.033.

[14] Sander, G. *et al.* (2018) 'Corrosion of additively manufactured alloys: A review', *Corrosion*, 74(12), pp. 1318–1350. doi: 10.5006/2926.

[15] Wei, P. *et al.* (2017) 'The AlSi10Mg samples produced by selective laser melting: single track, densification, microstructure and mechanical behavior', *Applied Surface Science*. Elsevier B.V., 408, pp. 38–50. doi: 10.1016/j.apsusc.2017.02.215.

[16] Rodríguez Rius, Daniel (2000). Obtención de capas de nitruro de titanio mediante tratamiento termoquímico en titanio y Ti6A14V y caracterización de sus propiedades para aplicaciones biomédicas. Tesis Doctoral, Universitat Politècnica de Catalunya. Available at: http://hdl.handle.net/10803/6032.

[17] Barsoukov, E. and Macdonald, J. R. (eds) (2005) *Impedance Spectroscopy -Theory, Experiment, and Applications*. Second Edi. New Jersey, U.S.A.: John Wiley & Sons, Inc. doi: https://doi.org/10.1007/s10008-007-0260-1.

[18] Orazem, M. E. and Tribollet, B. (2008) *Electrochemical Impedance Spectroscopy*. New Jersey, U.S.A.: John Wiley & Sons, Inc. doi: 10.1002/9780470381588.

[19] Manfredi, D. *et al.* (2013) 'From Powders To Dense Metal Parts: Characterization of a Commercial AlSiMg Alloy Processed through Direct Metal Laser Sintering', *Materials*, 6(3), pp. 856–869. doi: 10.3390/ma6030856.

[20] Yan, C. *et al.* (2015) 'Microstructure and mechanical properties of aluminium alloy cellular lattice structures manufactured by direct metal laser sintering', *Materials Science and Engineering A*. Elsevier, 628, pp. 238–246. doi: 10.1016/j.msea.2015.01.063.

[21] Iturrioz, A. *et al.* (2018) 'Selective laser melting of AlSi10Mg alloy: influence of heat treatment condition on mechanical properties and microstructure', *Welding in the World*. Welding in the World, 62(4), pp. 885–892. doi: 10.1007/s40194-018-0592-8.

[22] Alghamdi, F. and Haghshenas, M. (2019) 'Microstructural and small-scale characterization of additive manufactured AlSi10Mg alloy', *SN Applied Sciences*. Springer International Publishing, 1(3), pp. 1–10. doi: 10.1007/s42452-019-0270-5.

[23] Prashanth, K. G. *et al.* (2014) 'Microstructure and mechanical properties of Al-12Si produced by selective laser melting: Effect of heat treatment', *Materials Science and Engineering A*. Elsevier, 590, pp. 153–160. doi: 10.1016/j.msea.2013.10.023.

[24] Ambat, R. *et al.* (2006) 'Effect of iron-containing intermetallic particles on the corrosion behaviour of aluminium', *Corrosion Science*. Elsevier, 48(11), pp. 3455–3471. doi: 10.1016/j.corsci.2006.01.005.

[25] Leon, A., Shirizly, A. and Aghion, E. (2016) 'Corrosion behavior of AlSi10Mg alloy produced by additive manufacturing (AM) vs. Its counterpart gravity cast alloy', *Metals*, 6(7). doi: 10.3390/met6070148.

[26] Vargel, C. (2004) *Corrosion of Aluminium*, *Corrosion of Aluminium*. Elsevier B.V. doi: 10.1016/B978-0-08-044495-6.X5000-9.

[27] Cabrini, M. *et al.* (2016) 'Effect of heat treatment on corrosion resistance of DMLS AlSi10Mg alloy', *Electrochimica Acta*. Elsevier Ltd, 206, pp. 346–355. doi: 10.1016/j.electacta.2016.04.157.

[28] Battocchi, D. *et al.* (2006) 'Comparison of testing solutions on the protection of Al-alloys using a Mg-rich primer', *Corrosion Science*. Elsevier Ltd, 48(8), pp. 2226–2240. doi: 10.1016/j.corsci.2005.05.059.

[29] Gramy Instruments Inc. (2014) 'Basics of Electrochemical Impedance Spectroscopy', pp. 1–28.

[30] Nie, J. *et al.* (2020) 'Corrosion mechanism of additively manufactured 316 L stainless steel in 3.5 wt.% NaCl solution', *Materials Today Communications*. Elsevier Ltd., p. 101648. doi: 10.1016/j.mtcomm.2020.101648.

[31] Rafieazad, M., Mohammadi, M. and Nasiri, A. M. (2019) 'On microstructure and early stage corrosion performance of heat treated direct metal laser sintered AlSi10Mg', *Additive Manufacturing*. Elsevier, 28(April), pp. 107–119. doi: 10.1016/j.addma.2019.04.023.

[32] Gu, X. *et al.* (2019) 'Abnormal corrosion behavior of selective laser melted AlSi10Mg alloy induced by heat treatment at 300 °C', *Journal of Alloys and Compounds*. Elsevier B.V, 803, pp. 314–324. doi: 10.1016/j.jallcom.2019.06.274.

[33] Vargel, C. (2004) *Corrosion of Aluminium*, *Corrosion of Aluminium*. Oxford, UK: Elsevier B.V. doi: 10.1016/B978-0-08-044495-6.X5000-9.

[34] Zolotorevsky, V. S., Belov, N. A. and Glazoff, M. V. (2017) *Casting Aluminium Alloys*. First Edit. Oxford, UK: Elsevier. doi: 10.1017/CBO9781107415324.004.

Assessment of corrosion behaviour of SLM AlSi10Mg alloy: as-printed, heat-treated and cast-counterpart

INTRODUCTION

As chemical engineers, one potential and quite important task that is possible to perform concerns the transformation of currently employed technologies and materials into more sustainable ones. It is a principal goal that these produce lesser impact to the environment and thus provide a solving path to one of biggest concerns that we face as a society. The shift from steel parts into the utilization of light-weight materials, like aluminium alloys, has been an example of this, carried out in the automotive industry in view of reducing the amount of gasoline needed and thus diminishing the CO_2 impact. Interestingly, formability remains quite a big challenge as many parts characterize by their complex shape and traditional manufacturing processes may not be as efficient as expected. It is at this point that Additive Manufacturing (AM) promisingly provides an affordable way of replacing current automotive parts by offering a splendid mass customization through the possibility of instant computer-aided modifications. Nonetheless, before a new material is included in mass production it must successfully pass a prototyping phase which aims to evaluate every mechanical, physical and chemical property that is necessary to assure a proper final performance. Within this evaluation, Corrosion Assessment is an essential feature to include and which can certainly discard the usage of a metal as for the fairly adverse consequences that it might entail.

It is for such reasons that this thesis work is developed with the principal aim of evaluating the corrosion resistance of a particular aluminium alloy, known as AlSi10Mg, manufactured with the AM technology of Selective Laser Melting (SLM). Moreover, as mechanical properties are quite important for the automotive field, annealing process was performed to the mentioned material in order to diminish the residual stresses that characterizes every additive technology. In order to better understand the additive technique, its parameters, effects on microstructure and general corrosion behaviour of the resulting metal parts, an exhaustive chapter is presented in this thesis.

As a potential material to be used in automotive applications, the main utilized manufacturing process for aluminium parts in automobile also has to be taken into account. This relates to casting process, which generates nearly 64% of all of the aluminium parts (according to a *Ducker Frontier* assessment in 2019 vehicles [1]). Therefore, the corrosion assessment of AM samples is compared to the most utilized form of aluminium alloy, that is, cast AlSi10Mg. Aluminium application on automobile industry as well as the main characteristics that makes it an interesting material to study are described in a fully comprehensive chapter within this work. Moreover, and introduction on the interpretation of microstructure images as well as the sequence of processes that each sample submitted and gave rise to such characteristics is also detailed.

Regarding the experimental part of this thesis, the systematic corrosion study that is carried out comprises two main electrochemical experiments: Potentiodynamic and Electrochemical Impedance Spectroscopy (EIS) tests. Both performed with different goals, that is, to obtain different kinds of information that are nonetheless compatible and reflect the metal corrosion response. Each of these tests comprise the usage of a three-electrode cell connected to a potentiostat apparatus, whilst the results were displayed and analysed with the software *IviumSoft*. The three mentioned electrodes are immersed in a 0.6 M sodium chloride solution which provides the appropriate corrosive conditions. This solution is commonly defined as artificial seawater because of its equivalent chloride weight percentage to the seawater.

In the first experimental case the current response to the potential variation is assessed, generating a characteristic plot, from which thermodynamic and kinetic information can be extracted. For this purpose, a vast introductory chapter regarding electrochemistry background and corrosion is presented since it results helpful when interpreting the parameter values arising from the characteristic slopes determination. Furthermore, it provides an insight on the phenomena that is occurring at the interface of the corroding surface when submitting polarization tests.

The second mentioned experiment (EIS) regards the evaluation of the particular passive coating that is formed upon aluminium alloys when exposed to corrosive environments. A series of modelling procedure have to be performed in order to obtain representative parameters explaining such deposition layer features. Moreover, two types of standard EIS graphics are presented: the Bode and the Nyquist plots. Each of them also providing further information on layer resistance properties.

A quite important, yet not mentioned thus far, goal of this thesis is to ascertain the anisotropy that AM parts often present by differentiating the corrosion behaviour of two characteristic planes within. These refer to the parallel (XZ) and perpendicular (XY) to building direction (Z) planes; which not only depict different microstructure features but may also respond differently to a corrosion attack. Therefore, for the as-printed and the heat-treated samples, both XY and XZ planes are methodically evaluated.

The interpretation of each EIS and potentiodynamic results would not be complete if microstructure analysis was not performed as well. For this purpose, the use of the Field Emission Scanning Electron Microscope (FESEM) is included in the evaluation as it provides valuable micrographs at different magnifications. Upon these, different phases, morphology, characteristic dimensions and eventual porosity can readily be identified. Thus, it could become clear what are the features that influence the most the corrosion behaviour of the different alloys depending on their manufacture and post-manufacture techniques. In fact, these matters are acutely commented in the final experimental and discussion chapter.

As final statement, this thesis work has been performed in the frame of the research project "Corrosion behaviour of metallic materials for automotive processed according to different technologies" - Cooperation Agreement between FCA-CRF and Politecnico di Torino for the period 2019-2020.

1. ELECTROCHEMISTRY AND CORROSION

The Electrochemistry reflects a field of the chemistry studies with the aim of understanding the physical and chemical properties of systems where charged particles are involved, determining the electrical parameters and the chemical changes that take place [2]. These interactions between electrons and ions can take place under equilibrium conditions or non-equilibrium ones, depending on whether there is current involved or not.

In broad terms, it is the field to which corrosion studies always resorts to as these oxidizing reactions are taking place at the interface within the metal of interest and the environment to which it is exposed, which in turn can be in gas, liquid or solid state.

Within this wide area of studying, one can distinguish two main parts: one that studies the electrolytes' theory, which seeks the understanding of equilibrium and non-equilibrium properties of the electrolyte phase; and another part studying the thermodynamics and kinetics aspects of electrochemistry. This latter one explains the general equilibrium conditions characterizing the interfacial separation charged zones and the transport mechanisms carried out by charged particles through these zones and their structure's nature [3] as well. In fact, it is the one presented in the first part of this chapter.

1.1 Thermodynamics

1.1.1 Electromotive force (emf) in cells

According to thermodynamics' first law, any change of a system's internal energy is generated by heat (Q) absorbed or released and work (w) applied on it [4]. This is expressed on the following equation:

$$\Delta U = Q + w \tag{1.1}$$

The work done can be related to a mechanical one ($dw = -P.dV$), but also there could be present an electrical work (w_{elec}). At constant temperature and pressure conditions, equation (1.1) becomes:

$$\Delta U_{T,P} = T\Delta S - P\Delta V + w_{elec} \tag{1.2}$$

At constant pressure, using equation (B.2) in Appendix B:

$$\Delta U_P + P\Delta V = \Delta H_P \tag{1.3}$$

And, at constant temperature, using equations (B.2) and (B.3):

$$\Delta G_T = \Delta H_T - T\Delta S \tag{1.4}$$

Therefore, considering equations (1.2) to (1.4) the electric work can be defined as the change in Gibb's energy while maintaining pressure and temperature constant:

$$\Delta G_{T,P} = w_{elec} \tag{1.5}$$

When evaluating the w_{elec} that an electrochemical cell is able to produce, then it is convenient to evaluate the scheme illustrated in **Figure 1.1** (representative of a thermodynamic system as well).

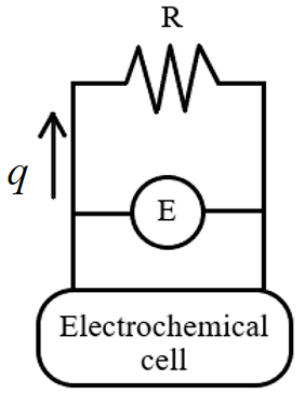

Figure 1. 1: Basic representation for an electrochemical cell (Adapted from [4] with modifications)

The cell has two terminals which submit not only an electric potential difference (here denoted as E and measured in volts [V]) but are also connected to an external resistance (R [Ω]) representing the surroundings. The work that the charged particle (q [C]) can perform to the surroundings is equal to the product: - $E.q$. This because the work represents a quantity of energy, measured in joules [J], whereas the product of volt [V] per coulomb [C] is equal to a joule. The negative sign is introduced as it is a magnitude that does not enter the system but transfers to the surroundings.

In order to determine the value of the transported charge, one can use the basic charged particle that is involved in electrical circuits: the electron. Thus,

$$q=[number\ of\ exchanged\ electrons]*[charge/electron] \tag{1.6}$$

or,

$$q = [number\ of\ electrons\ exchanged\ in\ the\ reaction\ as\ written]*[charge/mole\ of\ electron] = n\ .\ F \tag{1.7}$$

In the last product, the definition of the Faraday's constant (F) was introduced as the charge in coulombs (96484,6 C) per mole of electron. Therefore, the maximum electrical work that this system is able to perform is:

$$w_{elec} = -nFE \tag{1.8}$$

Combining this latter equation with equation (1.4) we have:

$$\Delta G_{T,P} = -nFE \tag{1.9}$$

Where the ΔG will be measured in [J/mol]. This equation is of great importance as it allows to determine the magnitude of the Gibb's energy thanks to measureable magnitudes (number of electron's mole and potential difference).

In the case where all the substances present in the system are at their standard state, then:

$$\Delta G_{T,P}{}^{0} = -nFE^{0} \tag{1.10}$$

where E^0 is the standard potential of the reaction [V].

The E^0 values can be used to calculate the electromotive force of the cell (ε). Considering that it is composed by two half reactions, the reduction one will have a value of E^0 that is equal to the *emf*, while the oxidation must submit a sign change. This because every value of Eº is defined considering the standard hydrogen electrode (SHE) as a reference. Therefore, all the potentials are reduction potentials, which reflects the component's tendency for submitting a reduction reaction. Knowing that in a cell's cathode the reduction takes place, and in the anode the oxidation, the following equation is used to calculate its electromotive force (ε_F):

$$\varepsilon_F = E^0{}_{cathode} - E^0{}_{anode} \tag{1.11}$$

1.1.2 Nernst Equation

Walther Nernst (1864-1941) suggested that the cell's potential (emf) can be related to the compound's compositions, the oxidizing agents as well as the reducing ones. Using equations (B.19) and (1.9):

$$-nFE = \Delta G^0 + RT\ln\left(\frac{a_C{}^{\gamma}.a_D{}^{\delta}}{a_A{}^{\alpha}.a_B{}^{\beta}}\right) \tag{1.12}$$

Defining the cell's standard potential (E^0) as:

$$E^0 = -\frac{\Delta G^0}{nF} \tag{1.13}$$

then the equation (1.12) can be rewritten as it follows:

$$E = E^0 - \frac{RT}{nF}\ln\left(\frac{a_C{}^{\gamma}.a_D{}^{\delta}}{a_A{}^{\alpha}.a_B{}^{\beta}}\right) \tag{1.14}$$

This is the Nernst equation that states the potential that an electrochemical cell can generate given the concentration of the involved species.

If working at room temperature (25ºC), it can be convenient to express the previous equation as:

$$E = E^0 - \frac{0.0592}{n}\log\left(\frac{a_C{}^{\gamma}.a_D{}^{\delta}}{a_A{}^{\alpha}.a_B{}^{\beta}}\right) \quad (1.15)$$

1.2 Kinetics

1.2.1 Double electric layer

In this section the focus will be at a molecular level, for the phenomenon taking place in the interface between the electrolyte and the electrode have a large theory background.

When the electrode is placed within an electrolyte solution, it gains a certain charge and as a consequence a potential difference is generated (electrode and electrolyte have different electric potential). There are several processes that can alter a surface's charge, for instance:

- Electron's movement from the metal to the electrolyte and vice versa [5].
- Ions adsorption over a solid surface
- Stablishing a potential difference using an external source.

The term of electric double layer refers to the formation of two opposite charged surfaces, made of ions or charged particles, which places in the interface between the electrode and the electrolyte. Therefore, this region is submitted to an electrostatic potential that differs from that of the electrolyte solution [6].

There are several theories that seek the explanation of this phenomena. One of them was introduced by Helmholtz (1871), who considered the ions forming these parallel charged surfaces to be immobilized by electrostatic attraction. As a consequence, the surface experiences a neutral charge. Moreover, this layer has a characteristic thickness beyond which the potential will instantaneously fall at the solution's bulk from its maximum (ϕ_0) at the very location of the layer. This variation is linearly characterized. In **Figure 1.2** this theory is represented.

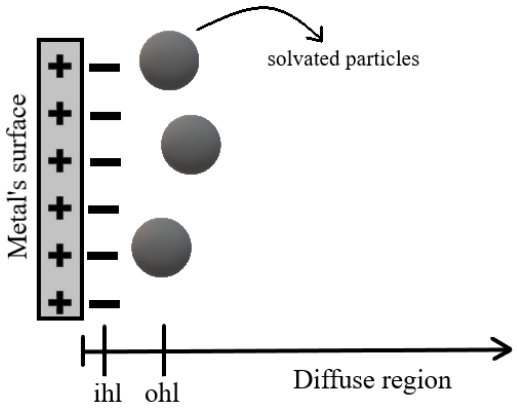

Figure 1. 2: Graphical description of Helmholtz theory (Adapted from [4], [7] and [8] with modifications)

Water solvent molecules have the characteristic of being dipolar, therefore, their effects must also be taken into account [7]. These tend to be attracted to the electrode's surface, with an orientation that depends on the surface's charge, and contribute to the mentioned potential difference within the double layer. Even more, water forms a solvation layer, which means a coat with adsorbed water molecules over the metal's surface. As a consequence, ions will approximate to the electrode only as far as the water layer and solvating water molecules permit

This maximum cation's approach distance will be taken as the reference for defining the *outer Helmholtz layer (ohl)*, whereas the *inner Helmholtz layer (ihl)* is formed by the specifically adsorbed ions. Finally, the charged particles positioned from the outer Helmhotz plane toward the electrolyte form part of the *charge diffuse region* [8].

As was outlined before, the local effect that arises in this particular region must guarantee a global charge of zero given by:

$$q_m + q_{ihl} + q_d = 0 \tag{1.16}$$

where q designes always a charge, q_m those of the electrons at the surface of the electrode, q_{ihp} related to those adsorbed and q_d the one characterizing the diffuse region.

In electrochemical tests, the electrode's potential is evaluated referring to a reference electrode, which is of course placed outside the diffuse region. This explored potential (ϕ_w) can be expressed as:

$$\phi_w - \phi_{ref} = (\phi_w - \phi_{ihl}) + (\phi_{ihl} - \phi_{ref}) \tag{1.17}$$

where the subscript *ref* denotes the reference electrode's potential.

It results important to outline that, according to Helmholtz theory, the interfacial capacitance value (concept explained in *Section 1.2.2*) does not depend on the applied potential. Conversely, it actually strongly depends on the potential. This is the reason why other theories were presented, owing the original charge redistribution hypothesis to the Helmholtz model.

The second theory was afterwards suggested by Gouy and Chapman [6]. They stablished that the layer could not only be made of immobilized ions, but there should exist another one submitted to non-uniform thermal motions. For this reason, the formation of a "diffuse double layer" within the solution would be the cause of the consequent neutralization of the interface. A charged particle distribution, of not only anions or water molecules but also cations, will generate a less sharped fall on the potential than the one predicted by Helmholtz, and expands over the outer Helmholtz layer no more than 1 μm. In fact, the decrease is exponentially characterized.

Finally, a more accurate theory was presented by Stern (1924). This would combine both previously mentioned theories. Therefore, immobilized ions as well as the diffuse layer contribute to neutralize the interface layer.

1.2.2 Double layer effects

When working with electrochemical cells, an external potential difference can be applied. As a consequence, the electrode's potential as well as the double layer's characteristics change. It is in this way that the effects of this particular layer's presence can be controlled and also modified.

When working with non-rigid electrodes, like a mercury drop electrode, there is a surface tension that arises within the electrode and electrolyte interface, a phenomenon that is called electrocapillarity. The mentioned electrode is formed by a capillary that will be placed inside the solution. A mercury drop will form on this capillary, increasing its size no further than a characteristic dimension, determined by the surface tension. A second scenario is also possible and takes place when working with constant capillary flow, a mercury drop creates but its lasting is markedly influenced by the mentioned tension. For the fulfilment of this thesis objectives, laboratory tests are carried out with rigid electrodes. Thus, the electrocapillarity is not going to be taken into account. Nonetheless, its studies are useful to determine the capacity of the layer. Therefore, a schematics of the variation of the surface tension (γs) with the applied potential (E), obtained thanks to the experiments carried out by Lippmann's method, is here shown in **Figure 1.3-a**.

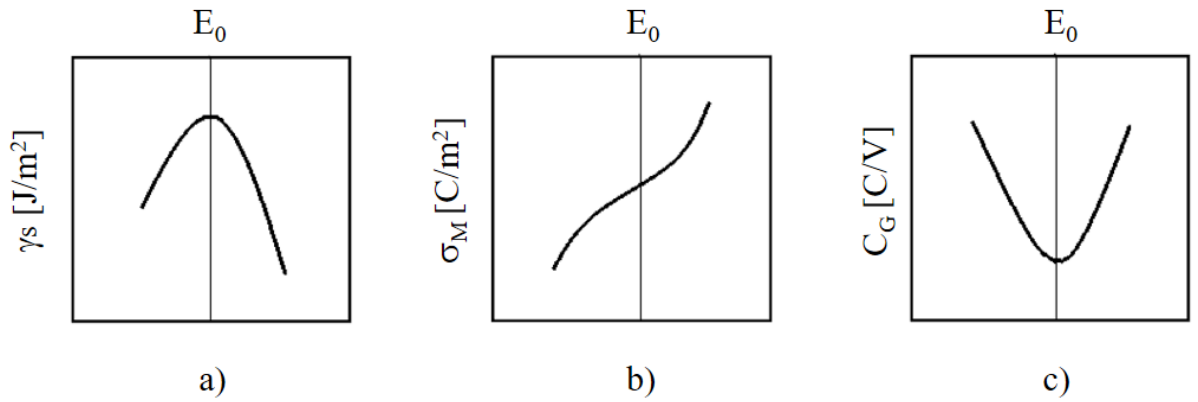

Figure 1. 3: Characteristic behaviour, with emphasis at E_0, of surface tension (a), charge density σ_M (b) and capacitance of the Gouy Layer C_G (c). Illustration adapted from [6].

As was outlined before, a second layer effect consists of the capacitance that its presence represents. In order to explain this, it is useful to know that a capacitor is an element that is able act as an electric energy storage, delivering the quantity of charge that it was able to collect during its charging period.

When an electrode, submerged in an electrolyte solution, submits a decreasing potential difference starting from zero (E_0), then the double layer is going to be charged up positively in order to maintain the neutrality of the system as the electrode's surface becomes more negative (σ_M). In the opposite case, when increasing the potential difference, then the double layer acts as a negative charge store. This behaviour is exhibited in the **Figure 1.3-b**. The metal's charge can be obtained by the following differential equation:

$$\frac{\partial \gamma_S}{\partial \Delta \phi} = -\sigma_M \tag{1.18}$$

The derivate of γ_S is done with respect of the potential difference ($\Delta\phi = \phi_M - \phi_S$) between the metal and the solution. If a random potential difference is stablished, then we can use the potential difference E_Δ applied instead of the $\Delta\phi$. Hence, equation (1.18) turns into:

$$\frac{\partial \gamma_S}{\partial E_\Delta} = -\sigma_M \tag{1.19}$$

It is then easy to see that the curve (b) represents the first derivate of the curve (a), and a characteristic potential E_0 is defined when the metal charge is equal to zero.

The concept of capacitance (C) reflects the ratio between the charge (q) that is stored and the applied voltage (ϕ) and is therefore measured in farads [F ≡ C/V]. Expressing it as a differential equation [4]:

$$C = \frac{dq}{d\phi} \tag{1.20}$$

According to Gouy model, the net surface charge density (σ), expressed in [C/m^2], is:

$$\sigma = \frac{\varepsilon\varepsilon_0\phi_a}{x_A} \tag{1.21}$$

where ε is the medium's dielectric constant, ε_0 is the free space permittivity (ε_0=8.854.10^{-12} C^2/(J.m)), "a" stands for the Helmholtz immobilized layer's thickness, and X_A is a parameter defined as:

$$x_A = \sqrt{\frac{\varepsilon\varepsilon_0 RT}{F^2 I_S}} \tag{1.22}$$

being F the Faraday constant, R the ideal gases constant, T the absolute temperature and I_S the ionic strength.

Considering in equation (1.20) the capacitance to be per unit of area in order to replace q [C] per σ [C/m^2], then the capacity of the Gouy layer (C_G) can be expressed, via equation (1.21), as:

$$C_G = \frac{\varepsilon\varepsilon_0}{x_A} \tag{1.23}$$

The latter equation represents the minimum value of capacitance that the system may present, and its determined experimentally when the potential equals the E_Z value, concept that was explained before. Even more, a representation of C_G vs potential is exhibited in **Figure 1.3-c**, which represents the derivate of curve (b). Therefore,

$$\frac{\partial \sigma_M}{\partial E_\Delta} = C_G = \frac{\partial \gamma_S}{\partial E_\Delta} \tag{1.24}$$

During the electrochemical tests that are going to be carried out in this thesis, the reaction will take place in one electrode, the working electrode (WE), which behaves in part as an

ideal polarizable electrode (IPE) [9] due to the double layer's effect. The IPE refers to the electrode's property of being able to block any current flow when there is a variation in the applied potential, as a capacitor does. If the current were illustrated against the applied potential then a straight line would be seen, for no variation in the current while the potential changes.

Nonetheless, a real electrode can only behave as an IPE within a specific potential range, whilst before and after that range current will be able to flow.

On the contrary, the second electrode used in electrochemical tests, the reference electrode (RE), is characterized by being ideally non-polarizable. Therefore, when measuring the potential between the working and the reference electrode, a voltage drop given by the following equation is seen:

$$E = iR = iR_s \tag{1.25}$$

where i is the current density [A/cm^2], R_s is the solution resistance, measured in ohms [Ω]; and E refers to a potential value. In particular, for tests conducted with voltage values under 1-2 mV, the two-electrode configuration can be used. Otherwise, a three-electrode arrangement is preferred, this third one called the counter electrode (CE).

1.2.3 Electron-transfer mechanism

This type of electron's proceeding will be firstly considered under the following simplifying hypothesis [4]:

• The mass diffusion processes throughout the electrolyte will be neglected for the solution is supposed to be properly stirred.

• Sufficient concentrated solution in order to assure a potential in the outer Helmholtz layer equal to that of the solution's bulk (initially equal to zero).

• As a consequence of the latter hypothesis, the concentration of the specimens in the bulk are equal to that of the outer Helmholtz layer.

On the basis of the next general equation, where O represents the oxidized form of a component, R its reduced form and e- the electron that is exchanged:

$$O + e^- \leftrightarrow R \tag{1.26}$$

both the cathodic and anodic rates can be expressed as being of first order with respect to the oxidized and reduced concentrations (C_O and C_R respectively), measured in [mol/m^3] and defined with the equations (1.27) and (1.28) correspondingly. Both of them are expressed as functions of the position with respect to the electrode's surface and time (t).

$$rate_{cathode} = k_c C_O(0,t) \tag{1.27}$$

$$rate_{anode} = k_a C_R(0,t) \tag{1.28}$$

The rate constants, k_c and k_a, have [m/s] as units of measurement. Therefore, the units for the rate are [mol/(m^2.s)], which represents a flux measurement. This indicates that the

cathode-anode difference is actually the net flux of the oxidize compound, which is also proportional to the net flowing current (I):

$$I = F.A.[k_c C_O(0,t) - k_a C_R(0,t)] \tag{1.29}$$

being A the cross-sectional area [m^2].

Assuming that the rate's constant is temperature-dependent, defined by the Arrhenius relation, then:

$$k_c = Z_r.e^{\frac{-\Delta G_c^{\Diamond}}{RT}} \tag{1.30}$$

$$k_a = Z_r.e^{\frac{-\Delta G_a^{\Diamond}}{RT}} \tag{1.31}$$

where Z_r is a pre-exponential term, theoretically determined, with measurement units being [m/s]; and $\Delta G^{\Diamond}$ the free energy of activation for the cathodic and anodic reaction.

It is known that at equilibrium conditions, the flowing current (I) is zero. Therefore, combining equations (1.29) to (1.31) and introducing the rate constants at this zero current state ($k_{a,0}$ and $k_{c,0}$), the next formula is obtained:

$$\ln \frac{C_O(0,t)}{C_R(0,t)} = \ln \frac{k_{a,0}}{k_{c,0}} = \frac{\Delta G_c^{\Diamond} - \Delta G_a^{\Diamond}}{RT} \tag{1.32}$$

Using the Nernst equation (1.14) for the compound's concentration ratio at equilibrium, the previous arrangement turns into:

$$\ln \frac{C_O^*}{C_R^*} = \frac{F(E_e - E^0)}{RT} \tag{1.33}$$

expressing the equilibrium potential as E_e and the bulk concentrations with the superscript "*". Moreover, when combining equations (1.32) and (1.33), the following is obtained:

$$\Delta G_c^{\Diamond} - \Delta G_a^{\Diamond} = F(E_e - E^0) \tag{1.34}$$

This latter equation shows how the difference between the system's energy change is equal to the difference between direct and reverse activation ΔG. As a consequence, by varying the cell's potential the cathodic and anodic rates can also be changed. An approximate approach of this dependence can be expressed, using a cathodic (α) and anodic (β = 1-α) transfer coefficient in order to separate the cathodic from the anodic free energy contribution:

$$\Delta G_c^{\Diamond} = \Delta G_0^{\Diamond} + \alpha F(E_e - E^0) \tag{1.35}$$

$$\Delta G_a^{\Diamond} = \Delta G_0^{\Diamond} - \beta F(E_e - E^0) \tag{1.36}$$

Results then that the activation free energy is equal to $\Delta G_0^{\Diamond}$ when the system's equilibrium potential is equal to the standard state potential ($E_e=E^0$). Hence, this parameter is considered to be a constant when working at a specific temperature value. The expressions for the cathodic and anodic constant rates can therefore be rewritten as:

$$k_{c,0} = k_0 . e^{\frac{-\alpha F(Ee-E^\circ)}{RT}} \tag{1.37}$$

$$k_{a,0} = k_0 . e^{\frac{\beta F(Ee-E^\circ)}{RT}} \tag{1.38}$$

where k0 is defined as:

$$k_0 = Z_r . e^{\frac{-\Delta G_0^{\Diamond}}{RT}} \tag{1.39}$$

Whenever a polarization test is performed, there's current flowing thanks to potential variations, and this means that the system is at a non-equilibrium state. Subsequently, the definition of an overpotential η is introduced for this deviation:

$$E = E_e + \eta \tag{1.40}$$

It is important to clarify that the overpotential is defined for a specific chemical reaction as the equilibrium potential is the known value. During corrosion phenomenon, more than one reaction is generally taking place. Therefore, there is going to be an overpotential related to each of them. Nonetheless, in the tests carried out in this thesis the potential range studied is chosen in a way to assure merely one reaction occurring [10].

Returning to the equation (1.40), it shows that under non-equilibrium conditions (due to a potential applied E), the cathodic $\Delta G^{\Diamond}$ submits a variation equivalent to "$\alpha F\eta$", whereas the anodic variation is "$-\beta F\eta$" [4]. Therefore, the constant rate equations turn into:

$$k_c = k_{c,0} . e^{\frac{-\alpha F\eta}{RT}} \tag{1.41}$$

$$k_a = k_{a,0} . e^{\frac{\beta F\eta}{RT}} \tag{1.42}$$

Using these latter expressions in equation (1.29) to calculate the net flowing current:

$$I = F.A.\left[k_{c,0} C_O(0,t) . e^{\frac{-\alpha F\eta}{RT}} - k_{a,0} C_R(0,t) . e^{\frac{\beta F\eta}{RT}} \right] \tag{1.43}$$

or in a reduced expression:

$$i = i_0 \left[\frac{C_O(0,t)}{C_O^*} . e^{\frac{-\alpha F\eta}{RT}} - \frac{C_R(0,t)}{C_R^*} . e^{\frac{\beta F\eta}{RT}} \right] \tag{1.44}$$

being $\boldsymbol{i_0} = i_{c,e} = - i_{a,e}$, the exchanged current density value in equilibrium conditions. In the case of a fast mass transport, where $C_O(0,t) = C_O^*$ and $C_R(0,t) = C_R^*$, the Butler-Volmer equation can be obtained:

$$i = i_0 \left[e^{\frac{-\alpha F \eta}{RT}} - e^{\frac{\beta F \eta}{RT}} \right] \tag{1.45}$$

This expression is valid for pure electronic transference state or activation state, that is, where the electron's transference is the mechanism controlling the global corrosion rate.

As a further consideration of the transfer coefficients α and β, in equations (1.41) and (1.42) it was seen that they represent the influence that k_c and k_a respectively have on the overpotential η. Taking the limiting case of α being zero (and β=1), the cathodic $\Delta G^{\Diamond}$ as well as the cathodic current would turn to be independent of the η, thus the anodic electrode of the cell would be the one under current flowing conditions.

1.2.4 Several overpotential contributions

In the previous section the concept of overpotential was introduced. As it reflects how far the system is away from equilibrium conditions, then it stablishes the polarization magnitude. A polarization can be done either with more negative potentials, with respect to the E_e, in which case we will be talking about a cathodic polarization or, if done with more positive potentials, it would be an anodic polarization.

When carrying out tests in any electrochemical cell, there would be three types of contributions to the total overpotential present. In this interpretation, the total overpotential (η_{total}) is defined as:

$$\eta_{total} = \eta_{act} + \eta_{conc} + I.R \tag{1.46}$$

where η_{act} represents the activation overpotential, η_{conc} the concentration overpotential and the product "I.*R*" would be the ohmic drop.

The activation overpotential η_{act} prevails at small current or voltage values. This characteristic electrochemical behaviour is described by the Butler-Volmer equation (1.45) from which then derives the Tafel expression (*Section 1.3*).

On the contrary case, the concentration overpotential η_{conc} is describing the mass transport resistance, in this phase: rate controlling. Fick's law expresses this phenomenon with the following equation:

$$J_O = -D_0 \left(\frac{\partial C_O}{\partial x} \right) \tag{1.47}$$

where J_O represents the oxidize species flux in [mol/s.cm^2], D_O its diffusion coefficient [cm^2/s] and the remaining ratio express its concentration variation within the interface or diffusion layer, being "*x*" the space coordinate.

The characteristic example for this kind of control is the reduction that the dissolved oxygen has to overcome by its diffusion toward the corroding interface [7]. Simultaneously, the corroding metal's ions (cations) spend a characteristic time to pass through the double

layer as well. At very high potential difference, the corrosion rate increases, which means that the concentration of the cations formed will also increase. As this situation is far for equilibrium, the passage from the metal's surface to the outer Helmholtz layer will be limited (diffusion limited) and repulsive force will arise. As a consequence, the further progress of the anodic process will stop, reaching the flowing current density its limited value regardless the voltage applied. This phenomenon is represented in **Figure 1.4**, precisely in the non-linear part, beyond the activation polarization zone.

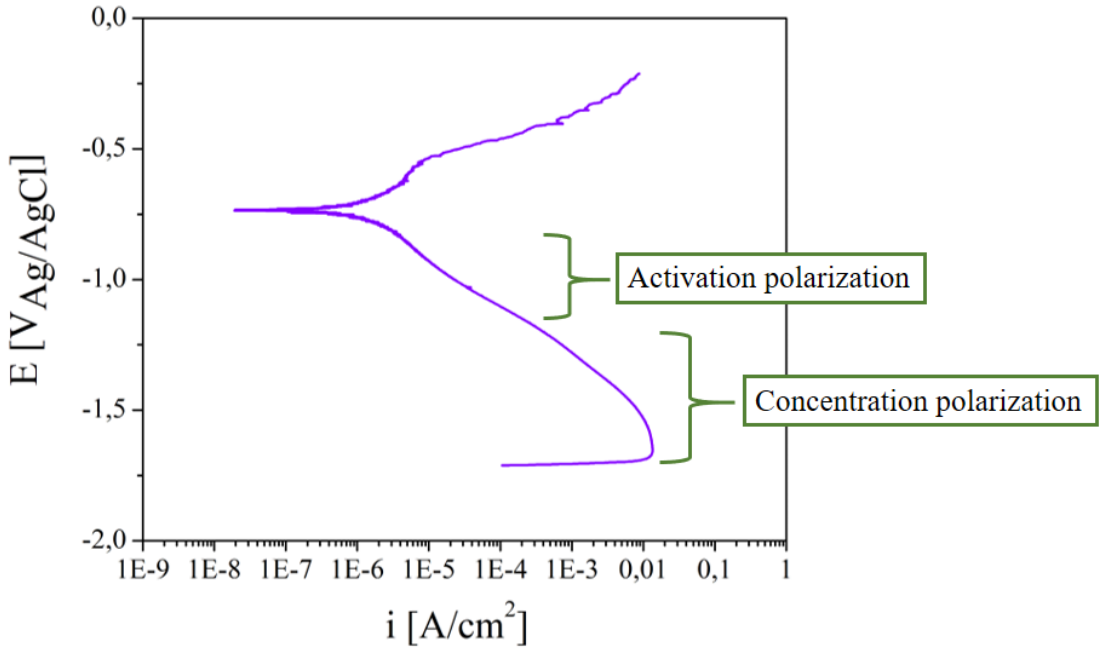

Figure 1. 4: Qualitative representation of the different polarization mechanisms[27].

Lastly, the Ohmic overpotential refers to the resistance caused by the electrolyte solution. This one can be neglected if, during experimental tests, the reference electrode is positioned near the working electrode.

1.3 The Tafel expression

The cell's kinetic data can be studied, in a strict empirical way, with the Butler-Volmer equation (1.45) [4]. Furthermore, when working significantly high overpotential values, in a way that the ratio "$F\eta/RT$" is beyond the unit, then one of the two contributions for the mentioned equation is going to become negligible. This fact gives rise to the Tafel equation, discovered in 1905, which aims to logarithmically describe the relation between the current and the overpotential.

[27] Plot obtained as part of the polarization tests performed within this thesis' experimental chapter.

If one places within negative overpotentials, which is the cathodic area of the current-potential curve, then the anodic weight in the Butler-Volmer equation disappears, turning this expression into:

$$i = i_0 e^{\frac{-\alpha F \eta}{RT}} \tag{1.48}$$

rearranging this latter one in a logarithmic form (1.49) and at the general case of 25ºC working temperature (1.50):

$$\ln i = \ln i_0 - \frac{\alpha F \eta}{RT} \tag{1.49}$$

$$\log i = \log i_0 - 16.9 \alpha \eta \tag{1.50}$$

From (1.49) it is possible to derive the expression for the cathodic overpotential (η_A) written as a function of the flowing current density [7]:

$$\eta_C = \frac{RT}{\alpha F} \ln\left(\frac{i_C}{i_0}\right) \tag{1.51}$$

The equivalent anodic expression for the Tafel equation can be obtained as:

$$\eta_A = \frac{RT}{\beta F} \ln\left(\frac{i_A}{i_0}\right) \tag{1.52}$$

Both (1.51) and (1.52) equations can be written in a generic expression:

$$\eta = a + b \log i \tag{1.53}$$

where *a* and *b* are constant variables.

1.3.1 Polarization diagrams

One of the main parts of this thesis is evaluating the corrosion rate, in terms of flowing current density (*i*), when varying the potential. This can be carried out through Evans diagram like illustrated in **Figure 1.5**, obtained from a polarization test of the perpendicular section of an AlSi10Mg sample, generated by 3D printing, in a 0.6 M sodium chloride solution.

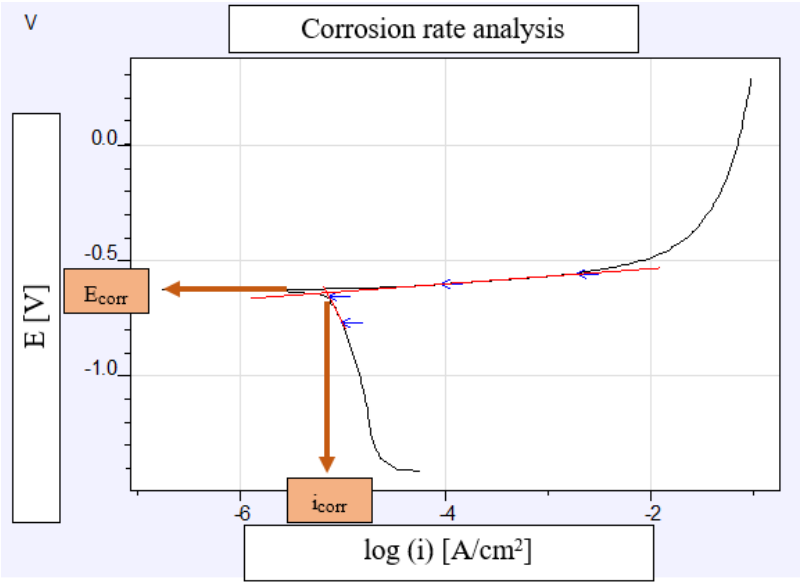

Figure 1. 5: Qualitative illustration of the characteristic values E_{corr} and i_{corr}.

In this diagram the overpotential values (η) are not presented; instead the applied cell potential is preferred but certainly in a range that depends on the equilibrium potential value, determined experimentally as the open circuit potential (OCP).

There are presented both the anodic and cathodic curves, the first one describing the potential displacing towards a positive potential and the cathodic one towards the negative direction. There are also designed the linear Tafel extrapolation straight lines (reported in red). These latter ones intersect at a characteristic value of potential, called the corrosion potential (E_{corr}); to which corresponds a characteristic value of current density called the corrosion current density (i_{corr}). Moreover, the value of E_{corr} corresponds to an overpotential (η) of zero, as the system is at its equilibrium point (OCP).

Therefore, Evans diagrams are fundamental in the studying of corrosion rate as it combines thermodynamic parameters (E) with kinetic ones (i). Nonetheless, when performing potentiodynamic tests there are certain matters to be taking into account when presenting results as they might make them unreliable. It is important that the sample geometry is properly controlled in order to assure a uniform current flow. Also, if the specimen has been subjected to current values presumably high they might present some degeneration.

On the basis of this helpful diagram, it is possible to determine the corrosion rate. Firstly, it is important to stablish the Tafel slopes from equations (1.51) to (1.53) as well as the data obtained experimentally. Nonetheless, not all the polarization diagram is described by the Tafel equation. When applying small overpotentials, also known as *micropolarization* [10], the slope starts to increase as the inverse reaction overcome 1% of the direct one, causing alterations on the electrode's surface relative concentrations noted in equation (1.44) [9]. However, when working with higher overpotentials it is possible to determine the Tafel slopes as this is the linear region on the Tafel plot (starting from overpotentials of 10 mV onwards) as seen in **Figure 1.6**.

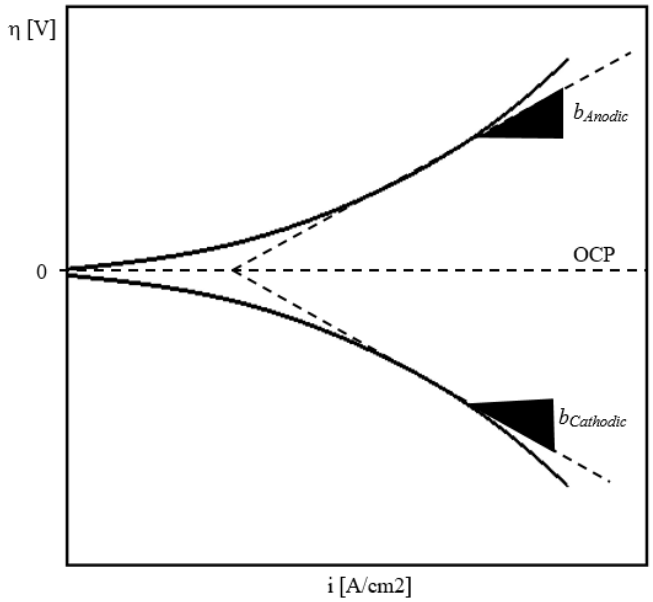

Figure 1. 6: Tafel slopes qualitative representation (Adapted from [7] with modifications)

Both anodic and cathodic Tafel linear approach have a slope, represented by *b* in equation (1.53), equal to:

$$b_{cathodic} = \frac{-\alpha F}{2.3RT} \tag{1.54}$$

$$b_{anodic} = \frac{\beta F}{2.3RT} \tag{1.55}$$

Another possible way to determine the corrosion rate (i_{corr}) is by implementing the *Stern-Gary equation* (1.56). This gives the value of the polarization resistance (*Rp*) as a function of both anodic and cathodic Tafel slopes as well as the i_{corr}. The mentioned resistance value derives from the Ohm's law as it is the slope of the potential-current density chart at the corrosion potential (E_{corr}) [7].

$$\left[\frac{d(\Delta E)}{di}\right]_{\Delta E=0} = Rp = \frac{b_a b_c}{2.303(b_a + b_c) i_{corr}} \tag{1.56}$$

The plot is linear with overpotentials η±10mV, this because a the logarithm of a generic variable *x* can be approximated to *(x)* when *x* tends to *0*.

The value of Rp can be determined with impedance testing where [6]:

$$R_p = Z_{\omega \to 0} - Z_{\omega \to \infty} \tag{1.57}$$

This latter equation means that, due to the characteristic reactive nature of the corroding surface, the polarization resistance is equal to the difference of the resulting impedance at fairly high and low frequencies [11]. In the following section the basis for this equation is explained.

1.4 Electrochemical Impedance Spectroscopy (EIS) method

A second approach for studying a metal's corrosion behaviour is by performing an EIS experiment. It differs from the polarization tests because the equilibrium shifting is performed around its vicinity and not far from it, like in voltammetry tests. Moreover, the system's response is known as relaxation or transient state as it evolves one again towards a new equilibrium state [12]. This characteristic response, which is a function of time, is the practical result.

1.4.1 Main impedance concepts

In order to provide a practical insight on this electrochemical technique, some basic aspects ought to be settled. In essence, an impedance experiment consists of using a signal generator to create a particular input signal [8]. As a result, an output signal will be generated. The transfer function is the expression that links these two signals together and, by means of appropriate instrumentation, is presented as dependent of frequency magnitudes, instead of time values, using the Fourier transformation as well as phase-sensitive detection. Particularly, if the mentioned transfer function happens to be the ratio between the potential and current then it is defined as *impedance* (Z).

When it comes to impedance mathematical representation, a real and imaginary component are often used. Taking the IUPAC convention as the standardization reference, the real part is denoted as **Z'**, whereas the imaginary part with **Z''**. Therefore,

$$Z = Z' - j.Z'' \tag{1.58}$$

The distinctive impedance response is usually modelled through an electrical circuit that assimilates to the electrochemical system's behaviour. Consequently, passive electrical elements characteristics should be introduced first. A resistor has the following expression as its fundamental quality:

$$E(t) = R.I(t) \tag{1.59}$$

which is similar to equation (1.25). Meanwhile, a capacitor is characterized by equations (1.60) to (1.62):

$$C = \frac{dq(t)}{dE(t)} \tag{1.60}$$

$$I(t) = \frac{dq(t)}{dt} \tag{1.61}$$

$$I(t) = C\frac{dE(t)}{dt} \tag{1.62}$$

Once the electrical circuit is defined, the impedance obtained is defined as:

$$Z = \frac{\Delta E}{\Delta I} \tag{1.63}$$

Furthermore, for a pure resistor and a pure capacitor, equations (1.64) and (1.65) define the corresponding impedance:

$$Z_{res} = R \tag{1.64}$$

$$Z_{cap} = \frac{1}{j\omega C} \tag{1.65}$$

being ω the angular frequency, measured in [s^{-1}].

These previous expressions were obtained from a sinusoidal voltage input like follows:

$$E(t) = |\Delta E|\cos(\omega t) \tag{1.66}$$

For which the current response would be:

$$I(t) = |\Delta I|\cos(\omega t + \phi) \tag{1.67}$$

being the terms |ΔV| and |ΔI| their respective magnitude values and ϕ the phase angle measured in degrees.

Taking into account these expressions, it is possible to suggest that the impedance will have only a real value when the input and output elements are in phase and will have only an imaginary part (null real part) when there is a phase difference between them.

Using the polar format to convey the impedance it is possible to obtain the following equations:

$$Z = |Z|\exp(j\phi) \tag{1.68}$$

$$|Z(\omega)| = \sqrt{Z'(\omega)^2 + Z''(\omega)^2} \tag{1.69}$$

$$\phi(\omega) = \tan^{-1}\left(\frac{Z''(\omega)}{Z'(\omega)}\right) \tag{1.70}$$

As well as expressions (1.66) and (1.67), it can be expressed using geometric format:

$$Z'(\omega) = |Z(\omega)|\cos(\phi(\omega)) \tag{1.71}$$

$$Z''(\omega) = |Z(\omega)|\sin(\phi(\omega)) \tag{1.72}$$

By means of these expressions it is possible to represent the magnitude and phase angle as functions of the angular frequency in the so called *Bode plots*.

1.4.2 Usual plotting representation

Considering mass transfer as well as reaction kinetics as the main reasons for describing electrochemical behaviour, plots focusing on low frequency response as the most suitable.

An important requirement when performing this experiment is to assure the studied system remains, during the entire time of collecting data, in a steady state condition [13]. This, however, is not easily achieved as EIS tests take several hours to be performed. As a consequence, problems like the rise of an oxide layer, presence of reaction products within the electrolyte, among others, may arise. Therefore, the system proceeds far from a steady state condition.

One of impedance representation method is through the Nyquist type of graphic. Here the real and imaginary terms of the impedance are plotted in what is called a complex plane [8]. Each of the imaginary and real components correspond to a singular frequency data; therefore, a graphic like **Figure 1.7** could be obtained.

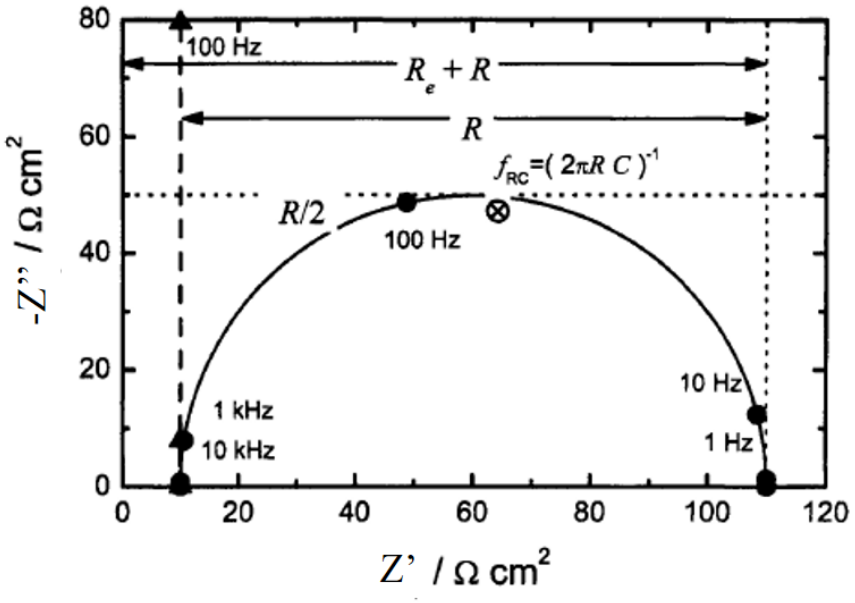

Figure 1. 7: Nyquist representation for *Re* of 10 Ω.cm^2, *R*=100 Ω.cm^2 and *C*=20μF/cm^2 (Extracted from [8] with modifications)

This plot has as its basic RC circuit the **Figure 1.8** where *Re* is the electrolyte resistance, and *R* and *C* a resistor and capacitor in parallel. The latter one can resembles to a double layer capacitance, as described in *Section 1.2.2*, or a film capacitance as well. On the other hand, a resistor contemplates the effect generated by an oxide or porous layer, can also represent the polarization resistance R_p, or even a charge-transfer resistance R_{ct}.

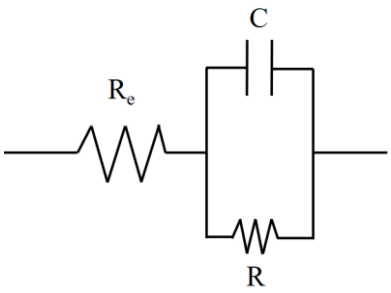

Figure 1. 8: Equivalent RC circuit employed for fitting impedance data.

On the basis of this latter circuit it is possible to develop a model that fits better the experimental data. Subsequently, important electrochemical characteristics can be obtained. First of all, in **Figure 1.7**, two real asymptotes correspond to *Re*, at high frequencies, whereas at low frequencies it equals *Re* + *R*. Additionally, the peak in the imaginary negative value reflects the system's characteristic relaxation frequency (f_C), which is measured in [Hz = cycles/s] and is related to the characteristic angular frequency through the expression: $\omega_C = 2\pi f_C$.

The latter parameter defined is also related to the characteristic relaxation time ($\tau_D = 1/\omega_C$) that can be defined as follows (Equation 1.73) and represents the necessary time for ideally charge the double layer:

$$\tau_D = C.R \tag{1.73}$$

The aspect of the curve could be useful to describe the principal mechanisms involved. A basic case of perfect semicircle shows a single activation energy type of mechanism, whereas two picks seen would indicate two characteristic time constants. More complex shapes require a more profound study.

A second kind of representation which is usually used is the Bode plot, earlier introduced on the previous section. The data is also plotted using the RC circuit at **Figure 1.8**. When presenting frequency values it is important to do it in a logarithmic way in order to better see the behaviour at low frequencies.

Taking into account the magnitude and phase angle definitions as well as the additive operations carried out in typical RC systems, it is possible to obtain the following expressions:

$$|Z| = \sqrt{\left[R_e + \frac{R}{1+(\omega RC)^2}\right]^2 + \left(\frac{\omega CR^2}{1+(\omega CR)^2}\right)^2} \tag{1.74}$$

$$\phi = \tan^{-1}\left(\frac{\omega R^2 C}{R + R_e(1+(\omega RC)^2)}\right) \tag{1.75}$$

Therefore, following these, **Figure 1.9** can be explained. The impedance magnitude response to a frequency that tends to infinite values tends to R_e as well as it tends to $R + R_e$ when $\omega \rightarrow 0$ in **Figure 1.9-a.**

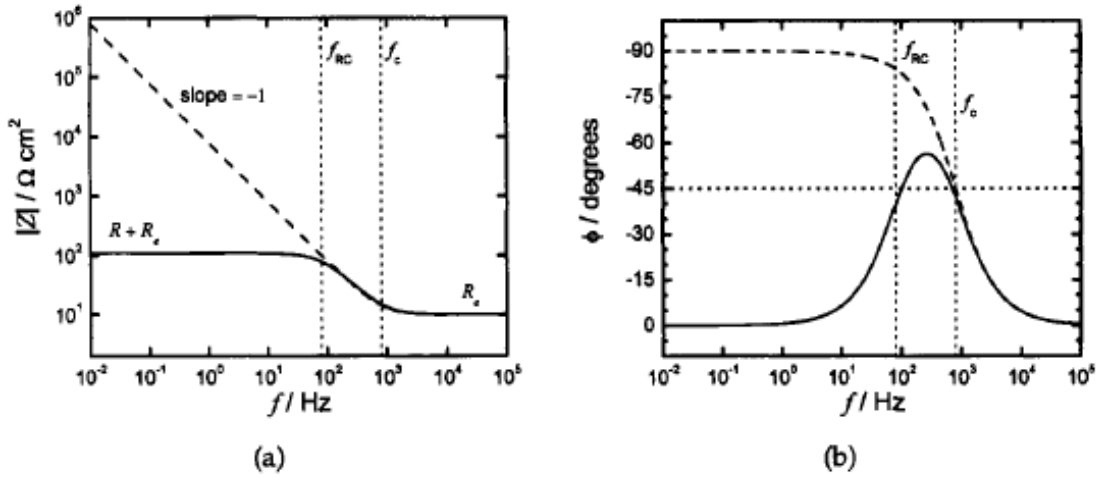

Figure 1. 9: Bode graphics for identical *Re*, *R* and *C* values as Figure 1.7 (Extracted from [8])

The phase angle is equal to zero at very low and very high frequencies. In the first case, this situation suggests that the current and the potential are in phase. Regarding the second case, null phase angles are found due to the predominant value of *Re* in the Equation (1.74). In addition, phase angles are particularly sensitive to fundamental system's parameters. Therefore, comparison between the entire experimental data is more accurate through these kind of plots.

This mentioned comparison is possible to be performed thanks to the identification of characteristic frequencies. For the case of a capacitor in parallel with a resistor, the impedance response (imaginary and real part against frequency) in **Figure 1.10** is obtained.

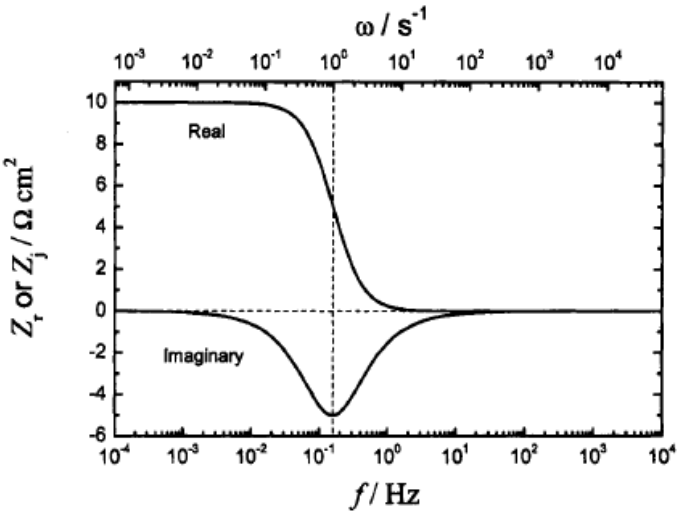

Figure 1. 10: Real and imaginary impedance trend when varying the frequency (Extracted from [8])

On the basis of this graphic the characteristic frequency (f_C) is determined by the minimum value for the imaginary component which corresponds also to the real component inflection point. As explained before, this is inversely proportional to the time constant.

In each of the previous plots the frequency was represented in a logarithmic scale in order to emphasize and see clearer the system's behaviour at lower frequency values.

1.4.3 Introducing modelling fitting procedure

As it was explained in the previous section, once the impedance data is obtained, the next step is to hypothesize the representative circuit model. This latter one usually consisting of a specific interconnection of resistors and capacitors.

The software that is used to perform the fitting uses an iteration procedure *named Non-linear least squares fitting* (NLLS) between the impedance spectrum from the proposed model and the experimentally obtained data, that is, the experimental spectrum [13].

Basically, the program starts with an initial value for a certain parameter, evaluates the obtained fitting result and determines whether there was an improvement in describing the experimental results with the initial model. This process, iteration, continues to be applied until a certain number or until a satisfactory result is obtained.

Even though the iteration procedure is carried out by a software, there could be serious errors in the yielded model caused by noise in the experimental data, non-physically-electrochemically-representative circuit model proposed, or even a not-accurate initial value for certain parameters.

Among the large existing EIS theory, there is often the mention of the (KK) Kronig-Kramers mathematical relations [11]. These consist of a series of integrations considerably laborious to carry out. Their purchase validate that the tests were conducted over the linear region within a wide frequency range, from zero to infinity. Moreover, the possibility of resolving these integrals confers the opportunity of obtaining the impedance imaginary component from its real one, or vice versa, as well as obtaining the polarization resistance R_p (introduced in *Section 1.3.1*) from a KK relation that derives from equation (1.58).

Nonetheless, the method that is usually applied is the *complex non-linear least squares* (CNLS). By performing this in order to acquire a fitting model, it is possible to assure that the KK expressions are satisfied and so they are no longer explicitly included in the modelling analysis, as long as an electrochemical compatible circuit system exists.

One of the main advantages of this technique is that all the experimental data is processed simultaneously. Therefore, it is possible to obtain satisfactory values for the desired parameters which takes into account the whole available information.

In its essence, CNLS analysis starts with two theoretical models which are expressed as dependent of angular frequency and specific parameters P as: $\zeta_k(\omega, P)$. These two functions can represent the imaginary and the complex parts of the impedance, or its magnitude and phase angle as well. It depends on what is the analysis goal and they will be specified in equation (1.76) with the superscript a and b. It is well known that for each angular frequency value (ω_i) a set of Z' and Z'' is obtained, therefore the analysis goal is to diminish as much as possible the sum (S_m) of every squares function as follows:

$$S_m = \sum_{i=1}^{n} \left\{ w_i^a \left[\zeta_{ei}^a - \zeta_k^a(\omega_i; P) \right]^2 + w_i^b \left[\zeta_{ei}^b - \zeta_k^b(\omega_i; P) \right]^2 \right\} \tag{1.76}$$

where each data point (ζ_{ei}^a and ζ_{ei}^b) will have associated a specific weight (w_i^a and w_i^b).

One of the main drawbacks of this technique is determining the minimum absolute value for the parameter *S*. Nevertheless, it can be sorted out by correctly estimating the initial values for the specified parameters.

2. ADDITIVE MANUFACTURING

With this term an innovative, yet still growing, technology for the sintering of three-dimensional parts layer after layer is referred to [14]. Among numerous articles, papers and books, a great number of authors have also named this technology as: additive-layer manufacturing (ALM), layer-based manufacturing (LBM), 3D printing, rapid prototyping (RP), direct metal laser sintering (DMLS), and so forth.

An appropriate and standardized set of definitions can be found within the International Standard document ISO/ASTM 52900:2015 [15]. On the basis of this principles, the acronym AM is appropriate to designate additive manufacturing and therefore, will be used along this thesis.

One initial characteristic of the final product is to be considered "near net shape"; which, according to the mentioned standard, suggests a product which will not need many, or any, further treatment to be considered appropriately dimensioned to final usage.

This processing technology may involve several different raw materials, as ceramics, polymers, metals or composites. Nonetheless, it is clear that fabricating a polymer, or even a polymer-based composite item results simpler as for selecting the appropriate process variables which will lead to a satisfactory final result [16]. This is not always the case for metal or ceramic-based materials. Therefore, the AM approach becomes of great importance when complex shape parts are required by different kinds of industries or field applications. Moreover, their manufacturing frequently presents higher costs than polymers. Particularly, in this thesis the focus will be on the metal sintering of the alloy AlSi10Mg.

In the automotive sector the introduction of light-weight materials is not always a problem, these can even be submitted to temperature treatments in order to reach stiffness requirements. Nonetheless, formability remains quite a big challenge as many parts possess a complex shape. It is from this fact that the SLM process gains interest in vehicle manufacturing. When using this technology with a prototyping approach easier customization can be achieved for the instant possibility of entering modifications in the computer-aided design.

Moreover, the use of SLM materials like AlSi10Mg does not only entail the benefits at a production level, like efficiently achieving complex-shaped parts, but mostly the less environment impact that its usage may generate. For example, a reduction of 10% in the weight of a car produces a decrease of 6.5% in fuel consumption. Consequently, for every 100 kg of weight that is reduced, CO_2 emissions are lesser by 8 g per kilometre of exhaust pipe [17]. It is demonstrated how the future prestige of an automotive company can certainly be dependent on progressively ensuring a lesser CO_2 contamination. Moreover, at a performance level, durability and safety are correctly guaranteed. Interestingly, the greater advantages are mostly wanted mostly for electric vehicles, for which the driving range is usually restricted.

2.1 Procedure characteristics

This profitable process can be carried out adopting different procedure variations, but each of them certainly different from the traditional cast process. This latter one typically consists of melting the metal of interest, which normally has a low melting point like the aluminium does, and injecting it in a properly conformed mould [18]. There are several methods by which the injection can be performed, like pneumatic or hydraulic-driven systems; and

several techniques involving different kind of moulds, like sand casting, shell mould casting, plaster casting, and so forth. Particularly, it is possible to perform almost any of the available process variations, restricted nonetheless by the available size reached, inherent properties prerequisites and design features.

One shared characteristic in every AM process is their starting point, that is, the initial 3D model upon which the AM machine is going to work from. A software is commonly used for setting this geometry [19] therefore creating, what is extensively known in the literature as computer-aided design (CAD). Modelling is actually quite unrestricted as almost any desired component, if pictured, can be then reproduced. Furthermore, if it already exists then its shape can be scanned in order to obtain its digital model data and reproduce it by means of the 3D machine. This procedure is called "3D scanning or digitalizing" in the mentioned Standard ISO/ASTM 52900:2015.

A second shared characteristic is the manufacture mechanism, which is based on making a layer after layer. In order to better understand this, a building platform, above which the fabrication begins, is consider to have a specific coordinate system [15]. This one is composed by an *x* and *y*-axis for the base surface, whereas the *z*-axis will indicate the height growth. Clearly, this system is orthogonal as shown in **Figure 2.1**. The clarification of this arrangement is important as afterward, on the assessment of corrosion behaviour, a distinction is made on whether the evaluated surface is perpendicular or parallel to the so defined *z*-axis.

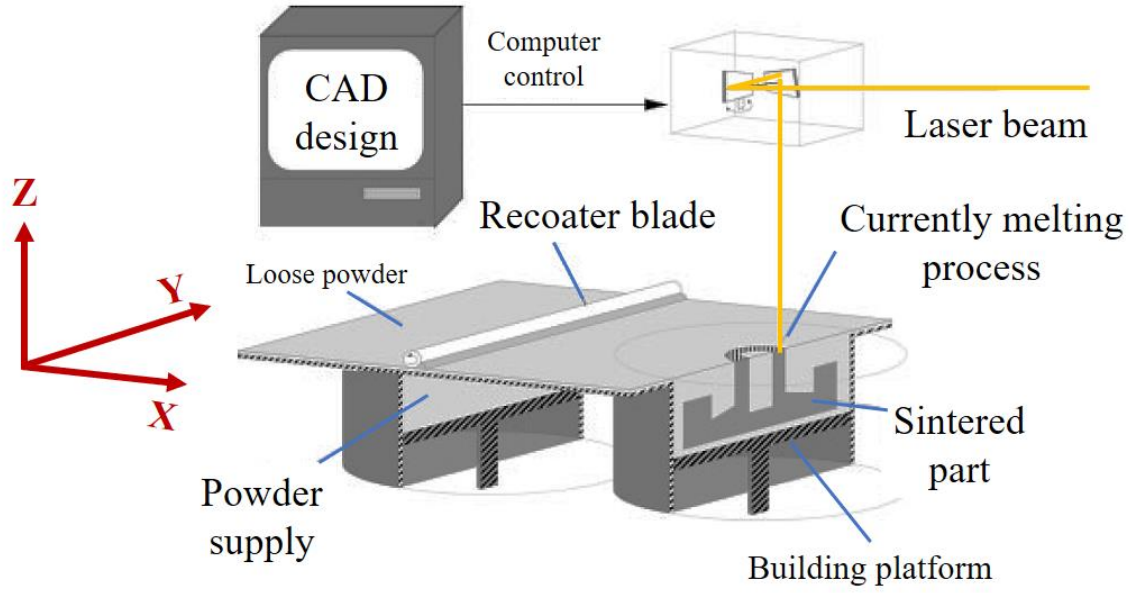

Figure 2. 1: Schematic representation of SLM process (Adapted from [20] with modifications)

Depending on the nature of the employed raw material the appropriate AM methodology is selected. Therefore, for the case of metal processing the following can be pointed out [21]:

i) Binder jetting

ii) Powder bed fusion (PBF)

iii) Directed energy deposition

iv) Sheet lamination

Moreover, each of these techniques are appropriate to certain types of alloy material. Great developments and research has been made mainly for PBF. This technique simultaneously includes two secondary methods: electron beam melting (EBM) and selective laser melting (SLM) [22]. Both of them start the operation with the deposition of a powder layer, called powder bed, which is then melted following the instructions of the CAD. The way in which the thermal energy is supplied for accomplishing the metal fusion is what differentiates each of the mentioned methods.

In EBM the source of heating is certainly the electron beam, whose operating system is confined within a vacuum chamber (pressures around $1.31x10^{-8}$ atm can be reached). The main purpose of generating the vacuum is to ensure possible oxidation and/or contamination as less as possible. The execution of this manufacturing concerns mainly titanium alloys.

Secondly, SLM is the processing technique of interest for the alloy under investigation; although it is also used for specific types of stainless steel and other aluminium alloys. In this case, the laser is performing the melting operation and its input energy is an important parameter that can and will be manipulated, along with other parameters, in order to better control the following cooling rate as well as the resulting material microstructure. Once the laser has followed the melting track, rapid cooling follows. Numerous research works have been conducted regarding the parameters controlling this part of the AM operation and their subsequent effects. Such parameters include laser traverse speed, hatch spacing (distance between two consecutive single-track melting), powder bed temperature and its thickness; like depicted in **Figure 2.2**. Usually, this system works within an inert atmosphere like nitrogen or argon gas, which prevents corrosion to happen. Moreover, the oxygen absence is secured by maintaining a positive pressure in the chamber.

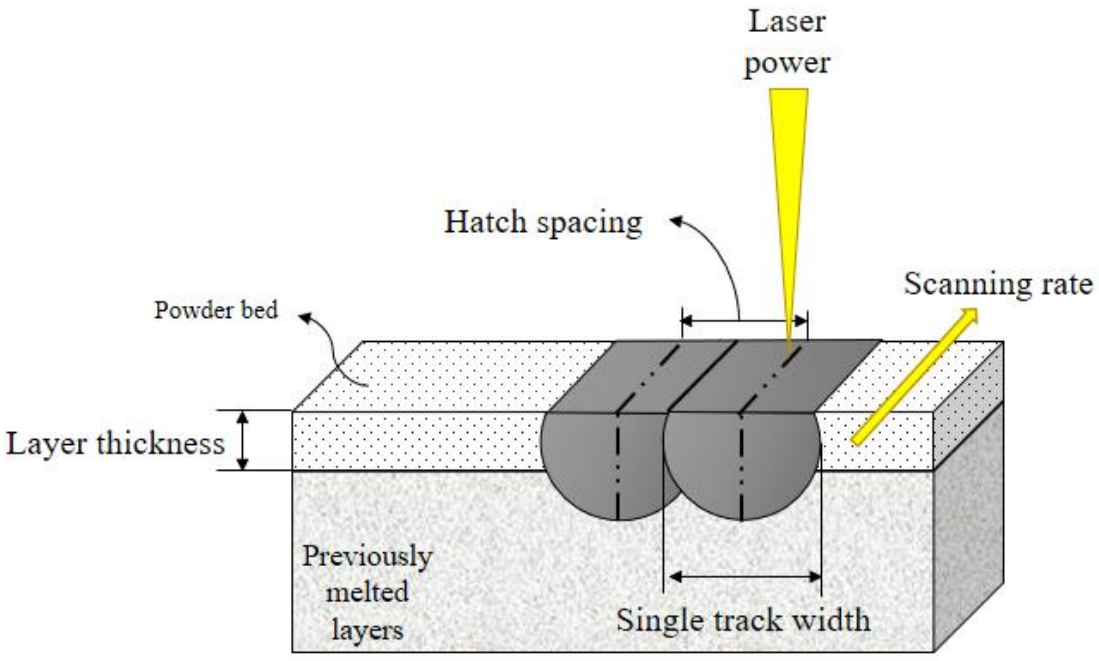

Figure 2. 2: Representation of the main parameters studied for SLM process (Adapted from [23] with modifications).

As seen in the previous picture, each of the single-track generated by the laser is characterized by its specific width (usually around 100 μm) [24]. After a layer is selectively melted, the working platform is directed downward in order to allow the following powder bed to be placed upon the finished one [25]. This process is handled by an appropriate recoating device, like depicted in **Figure 2.1**, which also determines the height of the powder layers. Once again, the beam is in charge of producing the proper layer design as well as the consolidation between two consecutive layers. This means that the melting procedure is performed not only over the last placed powder bed but also the previous cooled one, generating a joint molten pool.

Finally, when all of the intended layers where selectively melted and fused, the remaining powder that was not melted but formed part of each of the laid powder beds ought to be removed. Consequently, the finished 3D part is obtained [23].

2.2 Physical phenomena during manufacturing

It becomes quite important to give an introductory insight on the alloy physical changes during the additive processing, as it will certainly affect the resulting microstructure and its tendency to corrosion.

2.2.1 Laser features and consequent outcomes

As a first feature of any laser beam used in SLM technology, the Gaussian distribution in energy delivery is presented [26]. Such factor produces the well-known conformation of molten pools, like the arc-shaped elements depicted in **Figure 2.3**, as the maximum intensity is reached in the centre of the beam therefore generating higher depths in the central zone. This makes it possible to create a continuous finished part by linking each of the tracks with the surrounding ones.

Regarding the specifications of the beam, the initially employed laser was of CO_2 nature but later on replaced by the lesser wavelength characterized Yb: YAG fibre laser. This is the denomination for yttrium aluminium garnet (YAG) based on ytterbium (Yb)-doped, therefore belonging to the high power lasers category [27]. The purpose for using this type of laser is the improved absorptance level for metallic powder in the wavelength region that it works over [23].

When the powder bed begins to be melted by the laser, the energy transference depends mainly on the metal powder conductance (k) as it is at its solid state [24]. Subsequently, as there is a part of the previous layer that shall be melted again, the heat transference is now evaluated in terms of the ratio k/A, where A represents the absorptivity of the metal powder. Furthermore, this latter parameter changes upon powder's granulometry, shape, apparent density and physicochemical characteristics. Considering the total absorbed energy, a part lies within the loose powder material located in the surface; whilst the remaining energy is directed through the pores, hence interacting with gas particles. The heat transfer mechanisms comprise the usual conduction, convection and radiation.

Many investigations have been carried out to give an insight into powder absorptivity values. It was found that it higher values compared to bulk absorptivity. This was explained by understanding that the powder bed characteristic of reflecting the incident laser was additionally crossing deeply on the layer, therefore absorbing better the incident energy [23].

The interaction of the laser with the powder depends also on the thickness of such layer, as well as the powder size distribution [24]. If these two parameters are selected in order to equilibrate the incident radiation, then the single tracks will have a uniform aspect with stable molten pools. Conversely, at low scanning speed, higher or lower amounts of energy shall produce different kind of defects which produce unstable zones. For the case of increasing energy, some deviations and inconsistencies might arise on the single-track appearance, as well as higher volumes of melted powder accompanied with the increasing of its temperature. It should be noticed that the irregularities are produced because of steady production of vapours and boiling of powder bed. Instead, when the laser power is not enough, then multiple drops characterize single tracks aspect.

An important aspect, which has been considered constant for possible comparison, is the scanning speed. Along with the laser power will determinate a range of values for which a continuous track and suitable layer binding can be sintered, as both determine the amount of energy that is going to receive a given powder volume. It is clear that for each type of alloy powder, several experimentations are performed in order to find the correct parameters to set in the 3D machine and obtain the desired characteristics.

2.2.2 Temperature gradient and consequent outcomes

One characteristic that differentiates AM processing from casting is the cooling process that the molten metal experiences. Whereas for casting samples it is possible to consider uniform cooling rates over a given volume over time, it is not the case for AM specimens for which it variates spatially.

In additive procedures, the sample goes through several cycles of accelerated heating and melting, followed by rapid solidification and cooling [28]. This means that the solid phase transitions take place particularly fast, leading to non-completely-finished microstructural transformations.

Basically, when the energy per unit of powder volume increases (whether because of increasing laser powder and/or low scanning speed), then larger molten pools are generated and cooling rates diminishes. In other words, greater width or depth of the melting pool are generated, like depicted in **Figure 2.3**. At a microstructural point of view, grain sizes increase and coarsening levels as well. This means that if the cooling rate is increased, whether by an increase on the thermal gradient or by higher solidification rates, determined by the scanning speed, then finer microstructure will be achieved [26]. Moreover, higher hatch spacing can also produce lesser cooling rates because of greater heat accumulation over time and temperature peaks.

As a consequence of the described phenomena, residual stresses are reported on the so manufactured samples. Even if the identifying process of cooling and heating zones over time and space is a complex task to perform, an initial assessment can be here outlined [29]. When the laser beam melts a certain powder zone then three main zones can be differentiated. These are the melted area (M), the widely known heat-affected zone (HAZ), and finally the non-affected area (NA) like represented in **Figure 2.3**.

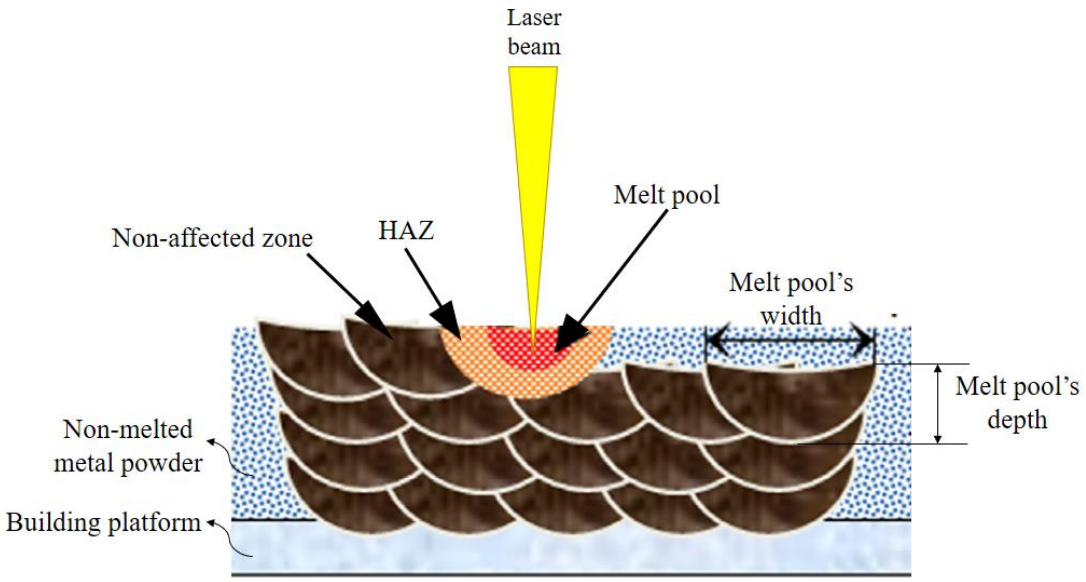

Figure 2. 3: Schematic representation of melt pool characterization (Adapted from [26] with modifications)

The temperature gradient can be represented in the following **Figure 2.4**, where Tp, Tm and Tr stand for the material's plastic point, melting temperature and room temperature respectively.

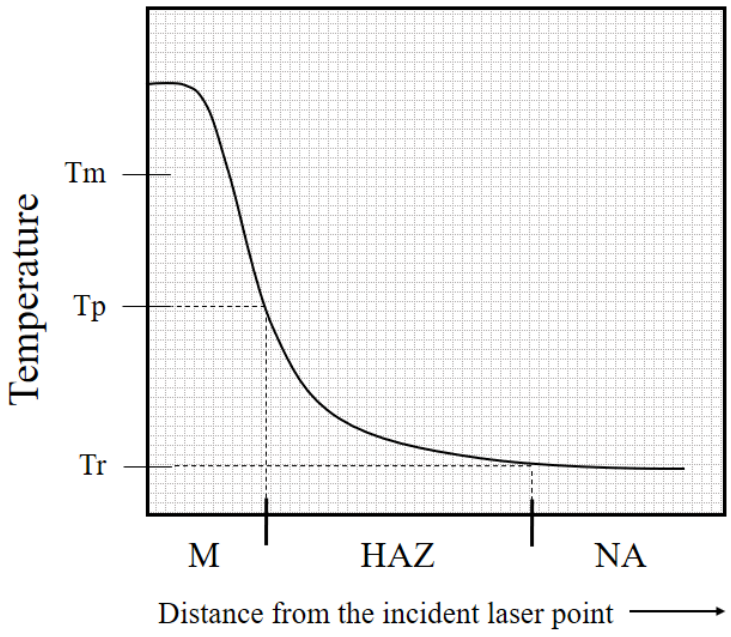

Figure 2. 4: Qualitative representation of temperature gradient in SLM process (Adapted from [29] with modifications)

As melting of the M zone occurs, the HAZ tends to expand but always restrained by the NA zone, creating compressive stress in the HAZ and tensile ones in the subsequent NA zone. Meanwhile, no tensile stresses are present in the M zone as it exceeds the Tm. Afterwards,

cooling begins to take place in the M zone, which actually experiments tensile stress due to the further compression of the HAZ. If solidification continues though, the third zone NA will present compressive stress as the adjacent regions, other HAZ and M zones, will further compress it.

This stress drawback has been assessed in numerous papers searching methods to reduce it [23]. Among the solutions found, many reported that previous powder bed heating could reduce nearly a half of the remaining stresses, whilst subsequent heat treatment provides higher reduction efficiency. More recent works reported that the conducted scanning strategy would produce even more decreasing. Specifically, selected zone scanning was proposed where square areas were scanned perpendicularly from each other.

2.2.3 Vaporization and consequent outcomes

Much attention has been drawn to unwanted effects from alloy laser welding, and so the possible volatilization of certain species was proposed in many studies [30]. As a process which performs high-temperature laser procedures to metals, the additive technology can relate to this effect as well.

For the special case of the AlSi10Mg alloy, it is known that magnesium has a melting temperature higher than the aluminium, but also lower than the aluminium boiling point. This means that, as temperature rises the magnesium will be the most volatile one, causing its evaporation from the molten pool and therefore producing the keyhole effect. This one can progress into inducing porosity in the material and deteriorating its mechanical properties.

Moreover, excessive vaporization might cause following condensation within the laser window and decrease the absorptance efficiency of the laser energy [20]. Working under high pressure conditions of inert gas might mitigate this problem.

2.3 Corrosion in AM samples

2.3.1 Main influencing characteristics derived from AM

As a common characteristic for SLM parts, porosity can be firstly introduced [31]. Two sources of porosity arise, whether it is the one present within the initial metal powder because of trapped gas or the one that surrounds them. Anyway, thanks to parameter optimization during additive processing, this undesirable feature can be quite diminished by adopting the optimum scanning strategy, increasing the laser power and/or reducing the scanning rate.

The negative effect that pores have in corrosion resistance will expressly be exemplified in the following *Section 2.3.2*. In general terms, pitting corrosion is enhanced by the presence of exposed pores in the surface under attack. This because of the decrease of the pH that usually occurs within this micro-sites, enhancing thereby the deterioration of the passive film. The diameter and internal morphology of these pores also influences on the re-passivation ability of the metal, making it certainly more difficult as this exposed size increases or as it becomes more convoluted internally. Certain heat treatment operations, inclusion of singular alloying elements or high-pressure plastic deformation have been proposed as methods to diminishing the porosity in AM parts.

A second feature affecting corrosion behaviour are the wide-known molten pool boundaries. Such sites have, as will be better elaborated when later presenting polarization

results, high potential to undertake pitting attack. This is linked to the particular characteristics that distinguish them from the rest of the semi-circular formation. Due to rapid heating and cooling stages a non-equilibrium limiting region is formed; which characterizes by specific constituent's depletion, several residual stresses and a higher porosity levels. All of which consequences contribute to increasing the corrosion rate.

The so mentioned fast heating and cooling proceedings engender as well the anisotropy characteristic of every additively manufactured material. Moreover, this irregular solidification process that takes place is different along the Z axis, as it is usually faster than the other directions. A simple explanation can clarify this phenomenon: the underlying layer, which has already been solidified, enhances the heat transfer mechanism if examined along the building direction. As a result, distinctive mechanical and corrosion properties as well differentiate both XZ and XY planes. Broadly speaking, many titanium and aluminium AM alloys studied showed higher corrosion resistance in the XY surface due to dissimilar physical configurations.

Lastly, the surface roughness (SR), granted by additive procedures, undoubtedly affects the corrosion performance. It is known that 10 to 30 times greater roughness than milling manufactured parts. The balling effect usually is in part responsible for such characteristic, as it produces molten droplets which float at the surface of the molten track. Another phenomenon contributing to SR is the gas expansion that becomes more significant as the powder bed thickness increases, thus creating more inconsistent molten pools.

Some studies show that surface roughness lowers the corrosion resistance and polishing methods can be used in order to improve this property. As it is known, preferential oxidizing attacks occur at those sites in the passive film which present defects or irregularities. This explains why the increasing number of cavities and superficial defects, commonly generated by AM techniques, accelerate the corrosion rate.

2.3.2 Particular cases of AM corrosion

Several metal alloys are currently used in additive technologies, for which corrosion studies are certainly needed. For this purpose, microstructure characterization will consistently be used to explain the characteristic corrosion phenomena that differentiates it, at a certain extent, from the cast counterpart. Broadly speaking, 3D printing generates a material with finer grain size compared to casting manufacturing, having additional precipitation of second phases and distinct distribution of certain solutes; all outcomes of the rapid solidification rate along with the noticeable temperature gradients.

In some cases, like 316L stainless steel additively manufactured, the higher corrosion resistance compared to wrought alloy is attributed to consequences of the rapid cooling rate during sintering process [22]. This rapid process made MnS particles to be practically absent, but instead emerged Mn-Si oxide inclusions. It is considered a favourable consequence as it has been evidenced that their presence contributes to pitting nucleation; but, when co-segregated with oxygen or silicon, pitting is clearly diminished. Moreover, if submitted to annealing process, the pitting potential does not particularly vary from the as-printed sample; making thereby feasible to reduce the residual stresses and have better mechanical performance without reducing its corrosion resistance.

This enhanced corrosion performance has also been evidenced in other studies [32], where SLM as well as laser metal deposition (LMD) 316 L alloy presented lower corrosion rates than the wrought sample. This was mainly attributed to the nobility of the alloying elements, like Cr, Ni, Si, Mn and Mo that were present in higher quantities at the border of the cells.

Meanwhile, Fe concentration at these particular sites was quite low. As a consequence, the corrosion attack was not focused on these boundary positions but actually they were the ones responsible to prevent, at a certain extent, the propagation of further corrosion to the metal. Moreover, higher resistance oxide layer was linked to the finer distribution of alloying constituents that presented SLM with respect to LMD specimens, whose grain sizes were as ten times larger, therefore generating a more compact and homogeneous passive film.

Nonetheless, there exists some contradictory results among research which evidence lower corrosion resistance in AM samples than wrought stainless steel [33]. In this study, Laser Engineered Net Shaping (LENS) generated 316 L parts with less durable passive film, having also lesser re-passivation potentials when compared to the values for wrought parts. This difference was here ascribed to Cr and Mo major concentrations at grain boundaries.

This issue was accurately cleared in quite recent studies [34], where not only potentiodynamic experiments contributed to elucidate this phenomenon but also EIS tests, which successfully evaluated the passive film generated. It was concluded that in AM specimens, a higher film quality was produced. However, lesser potential on intrinsic film restoration was revealed because of the molybdenum segregation at grain boundaries in agreement with Zietala, M *et al.* (2016) results [33]. This indicated lesser pitting resistance of AM samples with respect to wrought metal, but higher general corrosion-resistance properties linked with the finer-grains microstructure of the laser-sintered part.

Another important parameter to take into account when evaluating corrosion is the porosity degree that is typically generated during SLM processes but considered very poor for wrought alloy [22]. It was found for 316L steel that as porosity increased, the corrosion process was thermodynamically enhanced (higher E_{corr}) while pitting potential diminished more sharply. This means that corrosion resistance diminished and thereby the corrosion density current increased. An explanation that was proposed at a microstructural level was an *ion-diffusion barrier* which arises above the exposed area of the pores and enhances the entrance of chloride anions inside the pores and provoking the film's breakdown. Identic conclusions were depicted by a different alloy, that is the selective laser sintered Ti-Mo parts, for which, as porosity was increased by the Mo content, the corrosion rate also increased [35].

Some studies on Al-Cu-Mg alloy consider as an advantageous effect the finer spreading of precipitations throughout the microstructure [36]; stating that the consequently homogeneous distribution of pitting nucleation can contribute to a lower potential difference between the Mg precipitates and the surrounding Al-matrix. Nonetheless, if stress aging is more severely applied, then coarser precipitates will form at the expense of solutes present in the bordering aluminium matrix, therefore leaving lesser Mg concentration at these sites and increasing the potential difference. Hence, the corrosion resistance will be reduced.

As a final example of AM alloy group whose corrosion performance was studied is Ti6Al4V. Contrary to the previous presented cases, some research [37] report higher corrosion resistance of cast counterpart related to SLM parts. Even if different electrolytes were assessed, like H_2SO_4, NaCl or NaOH, results always showed higher corrosion rates for SLM materials due to the higher porosity grade when compared to the cast ones. This is the exceptional case where, higher uniformity in the cast constituent phases (α and β titanium grains) enhances corrosion resistance as the SLM part typically presents acicular martensitic morphology which are prone to pitting attack because of the meta-stable status that it presents. The type of passive film that both parts produce is quite different because of the higher porous grade in the SLM layer. This fact was explained to the porosity level in the part as well, but also to poor density achieved in sintered parts.

Further corrosion evaluation of Ti alloys was addressed in Sander G., *et al.* (2018) review [22] where certain differentiation was found on whether the XY or XZ surfaces of the SLM samples was exposed to the corroding environment. In aggressive conditions, 1M HCl solution, it was possible to determine higher corrosion rate in parallel (XZ) planes, correlated to the formation of less protective passive layer [38]. At a microstructure level, this detrimental behaviour was attributed to higher concentration of α'Ti-phases and lesser β'Ti constituent than XY surface. Accordingly with these results, heat treatment was found to diminish corrosion resistance because of lowering the α'Ti-phase content as well as grain refinement consequences.

3. ALUMINIUM-BASED ALLOYS

Among the earth's crust, aluminium represents the most abundant metal with 8% in weight, and the third element after oxygen and silicon [39]. Pure aluminium began to be used at the end of the nineteenth century, when its extraction mechanism was discovered in the USA by Charles Martin Hall and in France by Paul T. Héroult. As a lightweight material, it was initially used in the automotive industry, electric power distribution and aircraft industry. Nowadays its applications have certainly grown, to such an extent that its part of many of our everyday smart-devices. Moreover, it is a metal for which its recycling has especially been encouraged, giving birth to a secondary aluminium industry as its feedstock it is not the usual natural one but scrap.

Many contemporary structural applications would have not been possible if pure aluminium was used, as it is a rather weak material. Therefore, aluminium-based alloys are preferred. These are composed by adding different chemical elements which will enhance aluminium chemical, mechanical and structural properties. In fact, they represent up to 10% (referring to weight percentage) with less than 1.5% of eventual impurities.

Taking into account this thesis' particular alloy of investigation, it is known to be constituted by silicon, magnesium, manganese, iron, titanium and less than 0.01% of copper and zinc. The presence of silicon (9.7%), a semiconductor, diminishes the aluminium melting temperature as well as intensifies the fluidity as molten alloy which is desirable for casting processing. On the basis of this amount of silicon, the apparent low of amount of Mg (0.44%) defines the characterizing strength and is therefore an important constituent [40]. An element with an auxiliary effect is the manganese (0.38%) as it attenuates the adverse effect of iron. This latter element diminishes the mechanical performance of the alloy, particularly elongation, fracture and fatigue resistance.

3.1 Physical properties

One of the main features of aluminium alloy is its considerably superior strength per mass unit [41]. In other words, it forms part of the light-weight materials which are suitable for aerospace or automotive applications, among others [42]. Indeed, to comprehend better this favourable differentiation, we have the steel with a density three times more than aluminium, whilst mild and stainless steel present twice as much [43]. Therefore, their density makes them less suitable than aluminium alloys when using in transport, mechanical engineering and power distribution applications [44].

Pure aluminium particularly has a good thermal and electrical conductivity, as twice as much as copper. Therefore, it is possible to employ aluminium or its alloys for many processes involving heating or cooling, not only in food industries as it is a non-toxic material, but also in petroleum, automotive and other fields. The alloys will differ from pure aluminium in this conductance property depending on the chemical composition and on the following temper process as well. Because of the higher electrical conductivity, aluminium also replaced copper in energy distribution implementations, having additionally the property of providing and interesting material for undersea or underground cable protection.

In pursuit of fulfilling different application requirements, several types of aluminium alloys have been developed over time. For this reason, it is possible to classify them into eight major categories or families depending on their constituent's composition range. Some of these families will be characterized by higher corrosion resistance but lesser mechanical or

welding properties, for instance. Moreover, the corrosion mechanism can vary as the composition and microstructure do.

In the previous section it was mentioned that AM technology made it possible for complex geometry shapes to be manufactured. Nonetheless, it is also important to make an observation on an important characteristic for aluminium, which is the facility of manufacture that is has. Therefore, a variety of semi-finished products can be obtained by casting technique, extrusion of specific profiles necessary for particular employments, or rolling technique to produce flat elements like metal plates or sheets. Furthermore, joining procedures like welding, bolting or riveting are appropriate for aluminium making it possible to assembly finished parts in less time and costs.

Once an aluminium-alloy product has been manufactured, it rarely needs further surface processing [39]. Generally, posterior mechanical polishing, wire-brushing or sand blasting are satisfactory for application. Nonetheless, if further surface treatment is necessary for usage then aluminium is suitable for submitting chemical, electrochemical or paint finishing. Many of them are applied as a way of further preserving the product's aspect, diminishing the possibility of corrosion, increasing mechanical properties like superficial hardness or even improving the product's appearance [44].

From the environmental protection point of view, aluminium comprises a recyclable material. This reprocessing becomes interesting as the necessary energy for melting aluminium represents only 5% of the one spend for obtaining this metal from it natural sources. In fact, Italy (along with Germany) is nowadays the third country in the world to recycle more amount of aluminium, concentrating its entire aluminium production in 100% recycled metal [45]. According to the last year's statistics (2019), Italy has recycled 51400 tons of aluminium, 70% of which has already been reintroduced on the market.

3.2 Corrosion resistance

An entire subsection is dedicated to this physical property as it represents a main area of interest for being able to accomplish this thesis' goal. When assessing corrosion properties, it is important to clarify that it not only depends on the alloy properties, that is composition and microstructure; but also depends on the environment to which it is exposed and the exposure duration [39]. There exists a very extensive research on this topic, from which all report the aluminium undoubtedly resistance to corrosion. Correspondingly, this important feature is accomplished by the protective oxide layer that its formed when corrosion is promoted by several factors.

Examining related literature on thermodynamics, it is known that aluminium electromotive force indicates a particularly reactive metal; existing only two other more reactive metals (beryllium and magnesium) with structural applications. Therefore, the oxide layer that acts like a barrier against corrosion is the explanation for its particular resistance behaviour. This barrier is known to have dimensions of 4 to 10 nm high, increasing this thickness when exposed to higher temperature conditions and being able to restore the entire coating if eventually damaged. Nonetheless, if such exposure conditions become highly aggressive to the metal, then corrosion may happen as the recovering of the film will not be as completely finished as desired.

In particular, when immersed in an aqueous solution, the following oxidizing and two reduction reactions occur [44]:

$$Al \rightarrow Al^{+3} + 3e^{-} \tag{3.1}$$

$$3H^{+} + 3e^{-} \rightarrow \frac{3}{2} H_2 \tag{3.2}$$

$$O_2 + H_2O + 4e^{-} \leftrightarrow 4(OH)^{-} \tag{3.3}$$

Firstly, in the equation (3.2) it is important to clarify that protons come from the water equilibrium reaction that is present in any solution, where a water molecule is in equilibrium with the proton as well as the hydroxide anion. Secondly, the oxygen reduction in equation (3.3) is characteristic of neutral media as the case of natural water, or seawater.

As a result of the ions obtained as a corrosion product, the alumina is formed ($Al(OH)_3$). It is characterized by being insoluble in water, therefore it appears as a white gel precipitate in pitting corrosion type.

This natural corroding film is constituted by two overlapping layers, like represented in **Figure 3.1**. The first one, immediately above the metal, has an amorphous structure and given its dielectric characterization this zone is widely known as barrier layer. Commonly, the formation of this barrier takes less than a second; that is why it will always be present as soon as exposed to oxidizing environments. Its final dimensions will depend on the exposure temperature, being its height no more than 4 nm.

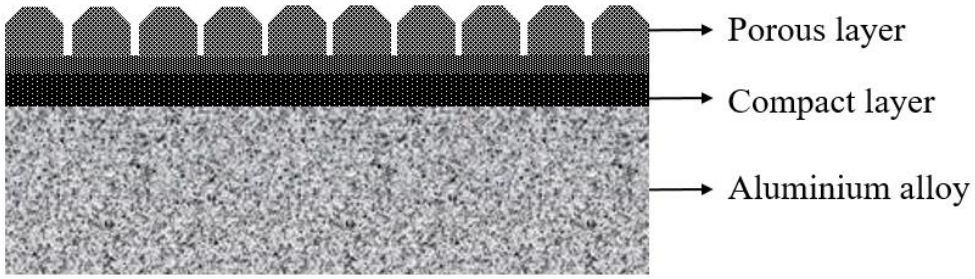

Figure 3. 1: Schematic representation of passivation film (Adapted from [39] with modifications)

Right thereafter this barrier film, a second and less compact layer is formed. This one characterizes by a higher hydration level than the barrier film. Moreover, its dimensions are also greater, growing with increasing temperature and relative ambient humidity. When immersed in water, aluminium oxide present on this layer will evolve into bayerite (monoclinic Al trihydroxide) and boehmite (orthorhombic Al oxide hydroxide) when temperature exceeds 70ºC.

Research has provided evidence for mechanisms influencing corrosion rate. Upon this, it is known that the barrier layer, as it is rapidly reconstructed after eventual disruption, does not have an impact on the global corrosion rate. Instead, the rate control is going to be in charge of the second protective layer. More clearly, three mechanisms are taken into account: external film's dissolution rate, evolution into bayerite and finally its progressive formation.

It was reported in literature that alloying constituents deviate, to a certain degree, the corrosion behaviour recently described. Actually, the layer formation rate can be affected by some metal additives which have a stronger tendency of oxidizing, therefore increasing the diffusion resistance and decreasing the oxidizing rate. In the same way, magnesium positively influences the corrosion resistance by the formation of mixed oxides. Conversely, the addition of other elements, like copper, tend to diminish corrosion properties.

Nonetheless, it should be taken into consideration that the corrosion behaviour of aluminium alloy depends also on the solution's pH into which is immersed as well as the potential to which it is exposed. Hence, it results practical to resort to Pourbaix plots, which describes that passivation will be present, instead of corrosion attack, under neutral pH values and potential values between –2.0 V and 1.5 V with reference to the standard hydrogen electrode (SHE). These conditions are in concordance with experimental conditions carried out in the "Materials and Experimental Methodology" section of this thesis.

The experimental part of this thesis will also focus on heat treated samples, for which it is important to note that they will present a different corrosion mechanism due to the several changes in microstructure that the metal overcomes through this treatment. In general terms, heat treatment alters the distribution of some of the constituent elements, therefore producing some variations on stress corrosion or even on intercrystalline phenomena.

3.2.1 Typical forms of corrosion

If there exists an aspect that identifies aluminium corrosion, it would be that it is usually a localized form of alteration. Therefore, pitting corrosion is going to be briefly discussed as it is prone to happen when the alloy is exposed to liquid environments.

Corrosion develops principally in those zones where certain discontinuities weaken or diminishes the film resistance, this is why it is called localized corrosion. Such effects arise because of intermetallic presence (Al_3Fe), some defects on the coating formation which renders it thinner, or even its eventual damage. The interest for these defects stems from the anodic properties that they get in relation to the rest of the metal, meaning that oxygen and water reduction or hydrogen reduction (equations 3.2 and 3.3) will develop in these areas. Meanwhile, in the cavity zone chloride anions will enter and aluminium will rapidly oxidize forming the complex chloride intermediate $AlCl^{-4}$. This because the aluminium dissolution continues by originating cations Al^{+3} localized at the bottom of the pit, which therefore enhances an electrical field drawing in further chloride anions and formation of the complex intermediate.

Subsequently, the hydrolysis of aluminium chlorides follows with the following chemical reaction:

$$Al^{+3} + 3H_2O \rightarrow Al(OH)_3 + 3H^+ \qquad (3.4)$$

This gives rise to a lower pH at the bottom of the pit (pH<3) making the surroundings optimal for the continuing of localized corrosion. The hydroxide that is formed will precipitate as the reduced H_2 microbubbles drive it outside of the pit cavity, creating white gel formations at the exposed metal surface. The progression of the pitting differentiates from the initiation period because the metal will no longer interact merely with the solution, but mostly with the several intermediate compounds that continuously change the surroundings [46].

As a way of graphically representing pitting, a photo is below presented (**Figure 3.2**). It was obtained from an immersion test performed on a cast sample of AlSi10Mg composition,

within a 0.6 M sodium chloride solution. After two days of immersion, a quite uniform pitting attack was seen; and, compared with additive manufactured samples, these corrosion products were visually noticed sooner.

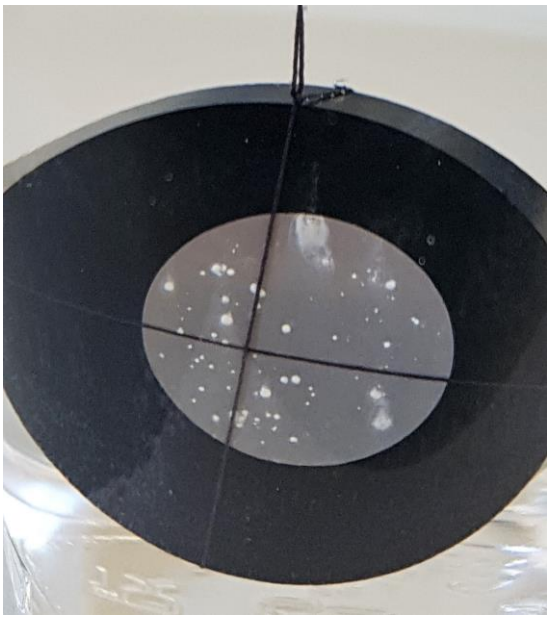

Figure 3. 2: Pitting corrosion after two days of immersion on 0.6 M sodium chloride solution.[28]

Several studies have concluded that the many alloying elements give rise to heterogeneity across the alloy, which follows with more severe and faster attacks. This is the case of copper or iron constituents, which decrease cathodic polarization, therefore reaching the pitting potential (E_{pit}) and initiating pitting corrosion [39]. This particular potential value gives an indication of the conditions under which pitting occurs on passivated metals, hence varying its value according to the solution pH, chloride concentration, working temperature and metal composition.

Even more so, irregular pitting aspects are expected along with variations according to the applied potential [46]. For instance, some can be hemispherical characterized at lower potentials and become coated with some porous film as the potential increases.

Some studies have been conducted in order to determine the variation of the pitting depth over time, that is, how much it would penetrate into the metal. It was found that a rapid increase characterized the first corrosion times; whereas growing diminished as time progressed. Even more, it is possible that the initiation of pitting would not take place but after days of exposure. This means that, if after a certain exposure time (weeks) a significant pitting depth is encountered, then it would not grow for the following dozens of years.

A second type of corrosion that is going to be seen during electrochemical tests is crevice corrosion. This is typical of those zones where there is a metal junction or where there is contact of a metal with a non-metallic material [39]. The latter case is the one present in the

[28] Photo taken by this thesis' author during immersion tests performed at Politecnico di Torino-DISAT (2019).

employed samples given the assembly made with silicon. It is characterized by the complete usage of the available oxygen within the crevice zone, with a further increase in aluminium cations concentration as the oxygen diffusion will be hindered. Such increase of positive ions will generate a particular chloride anion motion into the localized corrosion zone, enhancing further corrosion. The following hydrolysis reaction will occur, giving rise to an acidic pH between 2 and 3:

$$Al_3Cl + 3H_2O \rightarrow Al(OH)_3 + 3H^+ + 3Cl^- \quad (3.5)$$

The proceeding of this phenomena could be seen during immersion tests performed on AlSi10Mg samples obtained by additive manufacturing. After two weeks of immersion in a 0.6 M sodium chloride solution the corrosion product that was observed is depicted in **Figure 3.3**.

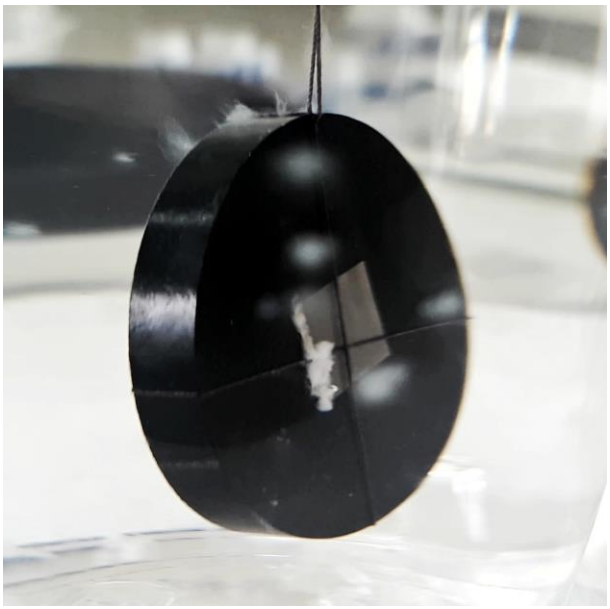

Figure 3. 3: Crevice attack on an AlSi10Mg sample obtained by AM technology after two weeks of immersion.[29]

As it can be seen, the crevice corrosion arises right on the contact zone of the metallic and non-metallic part, like it was similarly described before. This may result of a non-perfect sample mounting process. As the process results were not entirely accurate, the process probably left some porous zones between both sides.

[29] Photo taken by this thesis' author during immersion tests performed at Politecnico di Torino-DISAT (2019).

3.3 Automotive application

In most of the cases, automotive parts are made of steel and cast iron [47]. Nonetheless, new materials can always be considered to replace them if a number of criteria are achieved. One could argue that the most important feature that a material has to possess in order to be included in mass production is to be affordable, if it offers any superior advantages. The case of aluminium is quite advantageous as for the consequences deriving from being a light-weight material, among which there is the higher efficiency in fuel consumption, thereby the decrease of CO_2 emissions, and enhanced overall performance. However, in terms of costs is not actually lesser than iron or steel if considered the costs of raw material, further manufacture process, design and eventual testing. The sector in which aluminium alloys can encounter a certain improvement in costs is in the production branch. In this, thanks its higher machinability, achievement of practically finished-parts and less energy consumption for the melting of the metal, additive manufacturing technology can be considered an affordable method to include in automotive production.

If considering the last decade, several data [17, 48] the employment of aluminium in automotive applications has markedly increased, expecting to continue this trend in the following years. According to information published by *Ducker Frontier* [1], in 2019 the average cast, sheet, extruded and forged aluminium content in cars was 179.2 kg, expected to increase by almost 20 kg by the year 2025, remaining the predominant aluminium conformation that of cast.

Currently, the prevailing aluminium parts in automobiles comprise power train, that is engine, fuel system and liquid lines; wheels suspension and chassis, and finally the car body [48]. The age-hardenable 6xxx series of aluminium (Al-Mg-Si alloys) are usually employed in automobile body sheets. These must warrant bake hardenability, dent resistance, formability, hemmability, high lustre paint finishing and proper corrosion resistance [49]. If higher strength is accomplished by such hardenable alloys, then less thick panels can be manufactured, less raw material used, if there is not a decrease in dent resistance [48]. Still, formability remains a challenging issue, therefore giving rise to the importance of adapting additive technologies to the manufacturing of these parts. Meanwhile, non-age hardenable 5xxx aluminium series (Al-Mg-Mn) characterize by a superior strain hardening thereby offering great formability and strength in the alloy. Its use in automotive parts involves the hot-and-cold rolling of sheets and hydroforming of tubes. Even if such high content of magnesium allows the mentioned beneficial manufacturing properties, it also enhances inter-granular corrosive attacks, leading to eventual cracking. Therefore, a critic compromise had to be taken in order to guarantee strength and formability and less susceptibility to corrosion.

Wide-used extrusion process is often the chosen technique to produce space-frame models as well as certain secondary structures like chassis' components, bumpers or even crash elements. The alloys employed are from the age-hardening series 6xxx and 7xxx because of quenching transformations occurring throughout the extrusion procedure.

The most used manufacturing technique for automotive components is casting. In the past, cast iron engine blocks were fairly used. Nowadays, these were replaced by cast aluminium alloy, with Al-Si-Mg-Cu-Fe composition, as it presents suitable strength and endurance properties. Moreover, intake manifolds as well as transmission housings are also produced by aluminium alloys for reducing the entire engine weight [50]. The feasibility resides on the good sealing capacities for fluids, good thermal conductivity and mechanical resistance. Other than engine blocks, particular chassis components and cylinder head parts include cast current applications [48]. Furthermore, space-frames are considered to be potentially produced by this technique as nearly complex parts are achievable. It is therefore relevant that the corrosion

behaviour of AM samples ought to be compared with cast counterparts, as most of the aluminium volume in automobiles are manufactured by this method.

A further advantage of using aluminium parts in automotive industry is its unique and great potential on recycling [50, 51]. Cost-effective benefits are expected from the selection of this path if manufacturing with re-melted aluminium parts. Therefore, this seems to be a solution to the less-costly production of steel parts. Ideally, a rigorous selection of alloying type ought to be performed within vehicle recycling establishments. Nonetheless, two main issues should be firstly settled, which are the formulation of new alloys suitable to submit recycling process and refining the selection and sorting process in order to guarantee an optimal future performance. The first matter should be certainly linked with producing the AM raw material, that is powder metal alloy with all the required parameter that it has to meet. Meanwhile, the second matter implies a previous disassembly action which certainly entails further costs and thereby might give rise to a no longer cost-effective process.

3.4 Casting samples

As it was previously introduced, alloying constituents are included in aluminium in order to primarily enhance strengthening properties. Among the various possible components, it is possible to classify them as: principal, dopants or impurities [40]. For this thesis alloy sample, AlSi10Mg, silicon is the principal constituent as it is present in greater proportion by comparison with the rest of the metal elements. With regard of the different existing alloys, magnesium, copper or even zinc can stand for the principal component.

It is known that the inclusion of such alloying elements is possible because of their characteristic solubility on aluminium. Nonetheless, most of them do not exceed 1% of weight. This is the case of magnesium, manganese and iron. The rest of the constituents present markedly lower solubility in aluminium, around 0.01%, which is the case of titanium, copper and zinc.

In literature it was widely reported that principal constituents are characterized by eutectic diagrams with aluminium. These plots comprise a two-component representation, three or even four constituents. It is evident that the studied sample has more than two components; nonetheless, as a first approximation it is satisfactory to begin the study with a binary representation (**Figure 3.4**).

This graphic gives an idea on how the AlSi10Mg sample represent a hypoeutectic alloy given the silicon weight percentage, which is less than the eutectic one. Like every phase diagram, it shows the phases that are on equilibrium with each other at a specific temperature [52]. Such equilibrium is not always reached during manufacturing techniques, as they are not characterized by particularly slow heating or cooling procedure. Nonetheless, it is possible to understand more complex phase diagrams beginning with this binary simpler one. In fact, important information is acquired: for instance, the aluminium and silicon solidification temperatures (660ºC and 1414ºC respectively), the solidification phase sequence and the maximum solubility (1.65 wt.% of silicon in aluminium) at the eutectic characteristic temperature, whereas at room temperature is almost null.

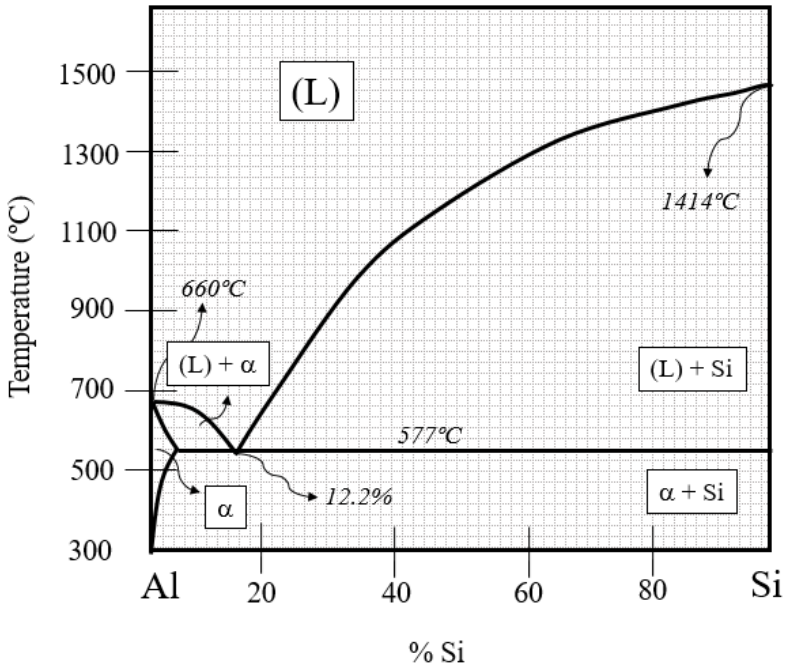

Figure 3. 4 Qualitative representation of binary phase features in Al-Si alloys (Adapted from [40] with modifications)

In general work to date on metallographic examinations [53], it was found that cast AlSi10Mg microstructure consists principally of an α-aluminium solid solution with a discontinuous β phase made by silicon, like presented in **Figure 3.5**. The aspect for the α phase is of dendritic characterization, whereas the eutectic silicon has an acicular or needle-like facet [54].

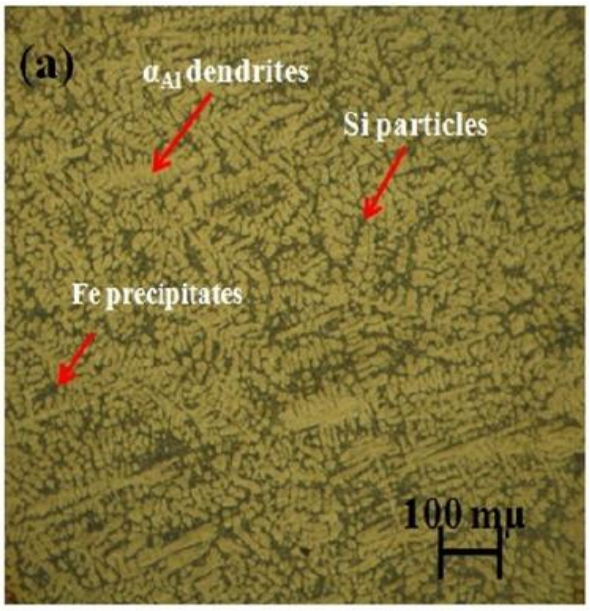

Figure 3. 5: Optical micrograph of as-cast aluminium alloy (by Sokkalingam, P. *et al.* in "Rheo-Die-Casting of Al-Si-Mg Alloy and Al-Si-Mg/ SiCp Composites: Microstructure and Wear Behavior" licensed under CC BY 4.0)

As it is well known, microstructure influences the material's properties. In this case, the acicular formation of Si has adverse effects as these zones are prone to unleash destructive failing, for being a stress concentration area, or enhance crack propagation. A used technique for diminishing this brittleness effect is adding sodium (Na) or strontium (Sr) on the melting process.

Further information was provided by other investigations [53, 55] taking into account the phases comprising the remaining metal constituents. The presence of iron evidenced the formation of many secondary phases like *β-Al_5FeSi*, but in a lesser quantities with respect to *α-Al* and silicon as it was seen from X-ray Diffraction (XRD) spectrum. This intermetallic component presented "script-type" aspect, varying its shape upon iron content. Because of iron negative effects on the alloy's properties, manganese (Mn) is usually added to reduce iron phase presence on the final microstructure. As another consequence of this inclusion, *α-AlFeSiMn* phase is formed (verified with Energy-dispersive X-ray spectroscopy EDS analysis) which renders better corrosion resistance and mechanical features.

Finally, the magnesium (Mg) component forms the intermetallic *π-AlFeMgSi* as well as *Mg_2Si* phase. According to literature data and given the mentioned compound weight percentage, the eutectic phase composition is: α-Al + Si + Mg_2Si(β) with an eutectic temperature (T_e) of 555ºC [40]. As it can be seen, the T_e slightly differs from the binary diagram shown in **Figure 3.4**, which is 577ºC, because this latter one does not take into consideration Mg as a third component. Combining XRD spectrum results with EDS performed in certain research [55], it can be concluded that at high magnifications silicon and magnesium are mostly dissolved and uniformly scattered within the aluminium matrix, therefore indicating no silicon precipitation. It was also investigated [52] the consecutive effects deriving from magnesium addition. It was found that it acted changing the morphology on aluminium dendrites which, for 0.45% of Mg content, was making them more lengthened.

3.5 AM samples: as-printed

It is commonly mentioned as a first processing parameter used to differentiate cast from SLM, the cooling rate; which for the first case is close to 10^2 ºC/s [56], whereas for additive technique is between 10^6 and 10^8 ºC/s [57]. Consequently, this relatively rapid cooling, and heating, process will stablish the material's microstructure and further mechanical properties.

As it is widely reported on SLM microstructure papers, the as-printed parts exhibit the typical sintering-produced molten pools. These present a repeated arc-shape arrangement when analysing the part's surface that is parallel to the building direction (**Figure 3.6-a**), whereas it is quite irregular when examining the cross-sectional surface [26] (**Figure 3.6-c**). The reason for this dissimilar shape is the laser beam's intensity, which is particularly higher in the core zone and progressively diminishes as displacing away from it.

By performing further magnifications with FESEM, it is possible to better understand the microstructure that characterizes the molten pools, like presented in **Figures 3.7** and **3.8**. These depict a particularly fine cellular-dendritic arrangement, which are characteristic of the dendritic spread exhibited by the α-Al matrix. As it was previously introduced, the cooling process will certainly differ from casting. This is evidenced when considering the silicon presence within this characteristic microstructure. According to research information [58], as the α matrix is formed, the solidification front will tend to expel silicon particles away into the liquid; therefore, increasing in the liquid the concentration of this solute. As described in the previous section, from the binary equilibrium plot, silicon solubility on aluminium is

considerably low. Nonetheless, this detrimental characteristic is surpassed by the high cooling rates, which consequently reduces the expected quota of silicon displaced from the aluminium and thus generating the typical cellular presentation.

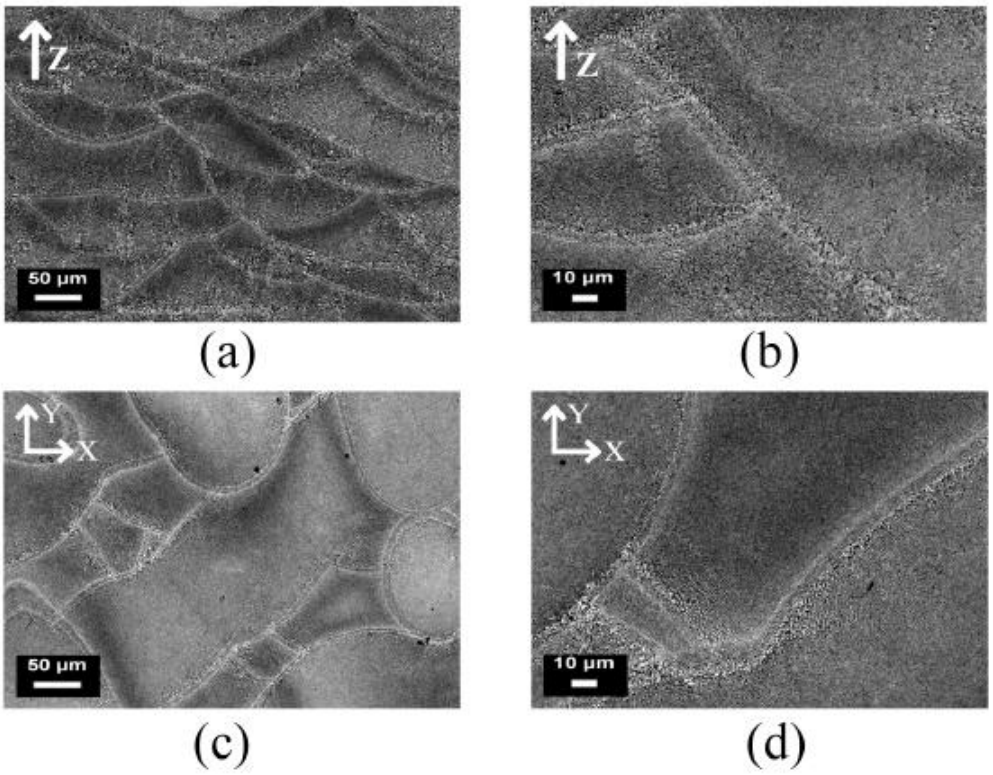

Figure 3. 6: Optical micrograph of surface parallel (a and b) and perpendicular (c and d) to the building direction (by Trevisan F. *et al* (2016), in "On the Selective Laser Melting (SLM) of the AlSi10Mg: Process, Microstructure, and Mechanical Properties" licensed under CC BY 4.0)

The so mentioned silicon displacement will apparently introduce these particles within cellular boundaries. This was ensured by several EDS elemental composition representations [55], which located Si mainly in the boundaries vicinity. By means of this valuable test, the magnesium distribution was also studied. It was found that it was more uniformly distributed than aluminium or silicon [26] throughout the entire microstructure. However, its presence along with ferrous presence [55] was mainly appreciated on particular facing sites within the cellular boundaries. This was attributed to the known reaction with silicon to form Mg_2Si, precisely at this limiting zones, enhancing strength properties.

By examining the varying dendrite morphology that is present on a single sample, three different zones are found according to its placement at the molten pool. These are: the heat affected zone (HAZ), the limiting boundary and the core [57]. As transformations due to the laser heating and melting are seen in XY plane as well as the one perpendicular to the building direction, both studies are presented in **Figures 3.7** and **3.8**; where the number **1** indicates the core zone, the number **2** the heat affected zone and finally the **3** the boundary zone.

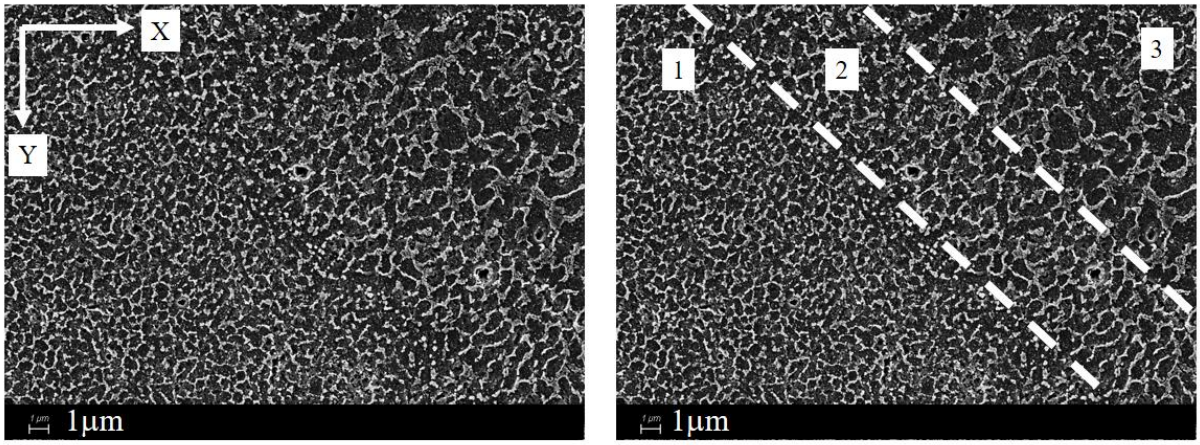

Figure 3. 7: FESEM micrograph on XY plane of AlSi10Mg sample made by SLM technology.[30]

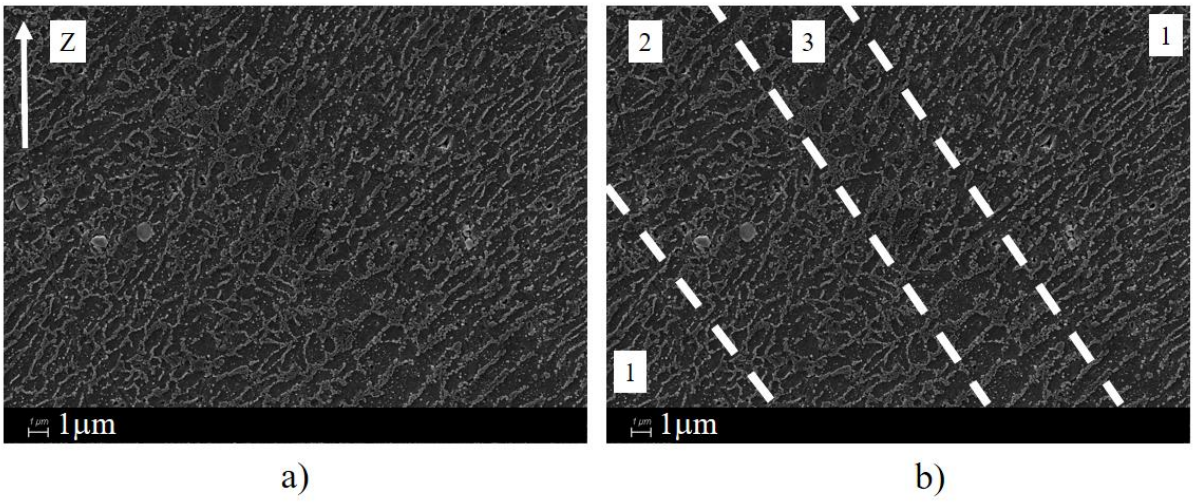

Figure 3. 8: FESEM micrograph along the building direction of AlSi10Mg sample made by SLM technology.[31]

From **Figure 3.7** it is seen how the core presents a considerably finer dendrite structure, with a more rounded lattice structure with respect to the boundary area, where the dendrites turn into more elongated structures presenting even several disruptions in the matrix. In the **Figure 3.8** a similar progressive pattern is seen. Nonetheless, the dendrites seen from this view are thoroughly different as, even in the core zone, they are quite elongated. What clearly differentiates the three zones is the spacing between each dendrite arm, being higher in the zone 3 and narrower as displacing to the zone 1.

[30] Micrographs taken as part of this thesis' *Experimental Results and Discussion* chapter.

[31] Micrographs taken as part of this thesis' *Experimental Results and Discussion* chapter.

3.6 AM samples: heat treated

Every layer-by-laser sintering process creates a quite varied temperature gradient along the whole structure. This phenomenon together with the thermal expansion capacity, plasticity features and the potential to stress distribution will create several residual stresses [59]. Some authors [29] have developed certain investigations on stress distribution after SLM processing, finding that those parts of the finished element close to the building platform present compressive stresses. Concurrently, the upper area remaining stresses are of a tensile characterization. When evaluating this distribution as a function of the scanning track lengths, it was found that if shorter segments could be achieved by performing sectioned area scanning, then residual stresses can considerably be diminished.

Nonetheless, it results difficult to completely characterize and understand the cooling sequence as the laser melting process can be fairly complex. As a consequence, various temperature gradients will be generated throughout a melted layer that will certainly change, or evolve into other ones, as the consecutive upper layer is melted. The adopted scanning strategy will further alter this cooling progression, as it was explained in the former paragraph.

Among the consequences that these, principally macroscopic, stresses may produce there are: shape alteration of the component, if supporting structures are used throughout the melting process then some detachments or loss of material's integrity might be produced. For this purpose, previous base structure heating was suggested as a manner of decreasing the probability of cracks develop [60]. As possible future undesirable consequences, the most important is the possible collapse [59].

Certain investigations were conducted in order to optimize the cooling sequence control, therefore adapting the AM processing parameters to critical regions whereas the delivered energy per volume unit is kept constant. Despite these attempts on redistributing the residual stresses where at a certain extent satisfactory, the conventional stress-relieving with heat treatment remain a favourable option.

It is interesting how an all-encompassing study on metal's microstructure and its main size parameters can predict and also explain the consequent mechanical performance. In fact, it is a key instrument into designing the material processing steps, and therefore meeting the expected requirements for its implementation. This is how an initial and well known effect of every annealing treatment is to refining grain size, which leads to an increase in strength (σ) [58]. The following Hall-Petch (HP) equation simply describes this effect:

$$\sigma = \sigma_0 + k_{HP}.d^{-1/2} \tag{3.6}$$

In the latter equation σ_0 represents the lattice resistance for dislocation movement, k_{HP} the HP slope characteristic of each material and d the average crystallite dimension.

By means of Rietveld peak refinement from XRD data, it is possible to obtain aluminium and silicon crystallite size as well as α-Al lattice parameter. The results from research conducted by Prashanth, K. G. *et al.* (2014) are summarized in **Table 3.1** hereafter.

Table 3. 1: Rietveld and XRD results conducted by Prashanth, K.G. *et al*. (2014) [58]

	Crystallite size [nm]		Lattice parameter [nm]	Free Si content [wt.%]
	Al	Si	α-Al	
Cast			4.0522	~10
SLM: as-built	118	8	4.0508	~1
SLM: heat treated (annealing at 450ºC for 6 hours)	218	142	4.05225	~8

On the basis of these results, it is proven that SLM processing generates a super-saturated α-Al matrix, given the low percentage of free silicon and a lowered lattice parameter. When the SLM sample is heat treated then the lattice parameter increases again and resembles that of casting. This is in agreement with the silicon rejection from the α matrix, nonetheless slightly lower that for the cast case evidencing that SLM process has enhancing properties on silicon solubility.

Moreover, in the mentioned research, it was found that the amount of expelled silicon increased with annealing temperature, as well as silicon particle size; whilst Si particle's density exponentially decreases. These two last parameters were also evaluated on hatch overlapping and its cores as well, presenting higher values on the overlaps. Therefore, it was illustrated that as heating took place, Si-rich boundaries overcame progressive silicon agglomeration, therefore increasing its dimension. Across the hatch overlapping however, this particle density is greater with respect to the core, as it can be detected in the **Figure 3.9** where the last picture at the right represents a microstructure under higher temperature:

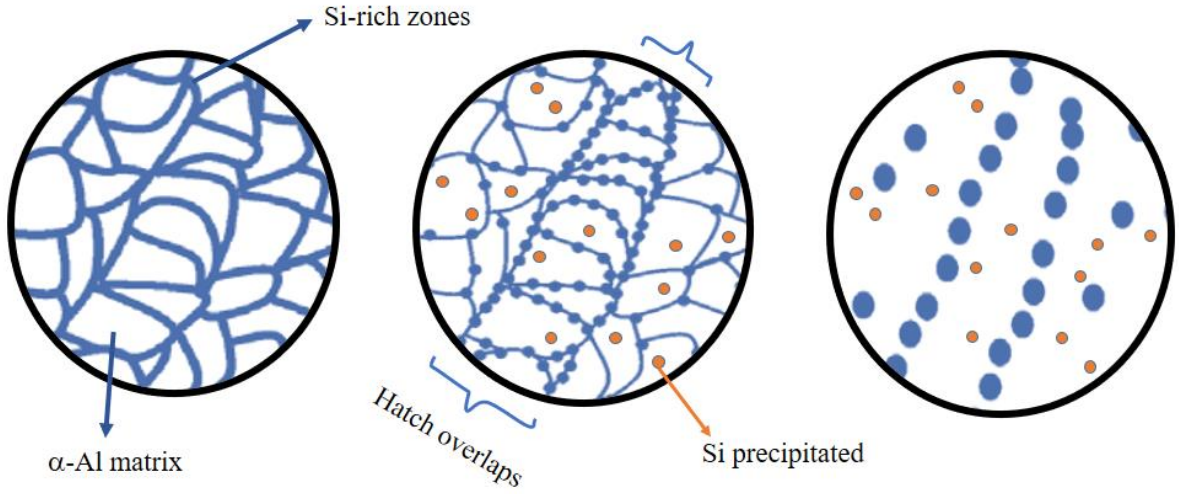

Figure 3. 9: Schematic representation of silicon distribution during heat treatment (Adapted from [58] with modifications)

A feasible explanation for this trend is that, as hatch overlapping means that this zone has been re-melted during laser sintering, then in a certain way it has experienced repeated localized heat transformations. Hence, it is more likely to induce silicon agglomeration.

The aforementioned silicon expelling during annealing treatment is seen within the columnar α-Al grains [61], like depicted in **Figure 3.9** coloured in orange. Whereas these are characterized as *fine* silicon particles precipitated within α-matrix, the other Si particles across the boundaries are termed as *coarsening* silicon. It is noteworthy the role that fine Si plays, as it is believed they weaken the grain boundary migration, also known as grain boundary pinning by particles, therefore diminishing the coarsening of the microstructure as a consequence of recrystallization or grain expansion.

As previously introduced, the intermetallic phase of Mg_2Si in SLM samples was not sufficiently present to being appreciated in certain composition studies due to the intrinsic cooling process. Nonetheless, recent studies [62] verify the increased presence of this intermetallic, through XRD patterns, when annealing process is performed to as-printed AlSi10Mg samples.

A brief final insight on mechanical properties derived from such microstructure changes is opportune to provide, as a way of genuinely appreciate the reason of performing heat treatments. Making a comparison to the as-built sample, annealing processing allows to diminish the hardness value in 30%. Increasing the magnitude of the heat treatment, like reached temperature, yield strength is decreased whereas fracture strain diminishes, thus generating a more ductile alloy [58]. Moreover, similar studies revealed that mechanical features actually vary according the direction that is tested [28, 61], that is the X-Y surface or along the Z direction; phenomenon that is widely known as anisotropic behaviour. For as-built specimens, yield strength is lower along Z direction as well as tensile elongation. Identical contrasted characteristics were found for the annealing specimens, but presented overall lesser values in strength and higher percentage of elongation, therefore enhancing the material's ductility.

4. MATERIALS AND EXPERIMENTAL METHODS

This chapter is dedicated to presenting the main characteristics of the raw material (powder) that was employed in the manufacturing of the AlSi10Mg samples as well as describing the procedure carried out in the multiple electrochemical tests.

4.1 Samples' specifications

The metal of interest that is the core of this thesis is, as introduced before, an aluminium alloy known as AlSi10Mg. Its manufacturing beholds a particular technique that is the Selective Laser Melting. Therefore, the raw material from which it is possible to carry out this kind of 3D printing is a particular powder.

To start with its chemical composition, specifically expressed as weight percentage (wt-%), the descriptive **Table 4.1** is presented by indicating range values.

Table 4. 1: Chemical composition of AlSi10Mg raw powder

Chemical element [wt-%]	***Al***	***Si***	***Mg***	***Mn***	***Fe***	***Ti***	***Cu***	***Zn***
Minimum	Balance	9.00	0.20	0.20	-	-	-	-
Actual	Balance	9.70	0.44	0.38	0.20	0.01	<0.01	<0.01
Maximum	Balance	11.00	0.45	0.45	0.55	0.15	0.05	0.10

The powder is produced by the wide used metallurgic technique of gas-atomization [63]. Briefly, it consists of fine droplets dispersion generated by an inert gas passing through an atomizer [64]. Depending on the machine's parameters as well as the gas parameters (gas rate, temperature, density, viscosity) it is possible to settle a specific particle size distribution.

Based upon the possibility to manufacture alloy powder with specific dimension, in this thesis the samples that were used came from 30 μm powder. In order to better differentiate them from casting samples, from now onward the as-printed SLM ones are going to be designated with the acronym ***AP***, whereas the ones that submitted heat treatment hereafter detailed are designated with the acronym ***HT***.

4.1.1 Additive Manufacturing specifications

The SLM manufacturing process was carried out by *EOS M 290* additive-manufacturing machine. The source of radiation is an Yb-fiber laser, characterized by laser power of 400 W which allowed optimal details resolution.

The selected bed powder height was 30 μm, which experienced a scan melting rate of 1300 mm/s with a hatch distance of 0.19 mm. After a single layer was completed and the

building platform descended, the following layer was sintered with an orientation angle of 67º with respect to the former layer. High purity inert gas was supplied in order to minimize undesired oxidation effects.

The three-dimensional parts that were sintered were cubes, whose side dimensions were 20 mm, like illustrated in **Figure 4.1**.

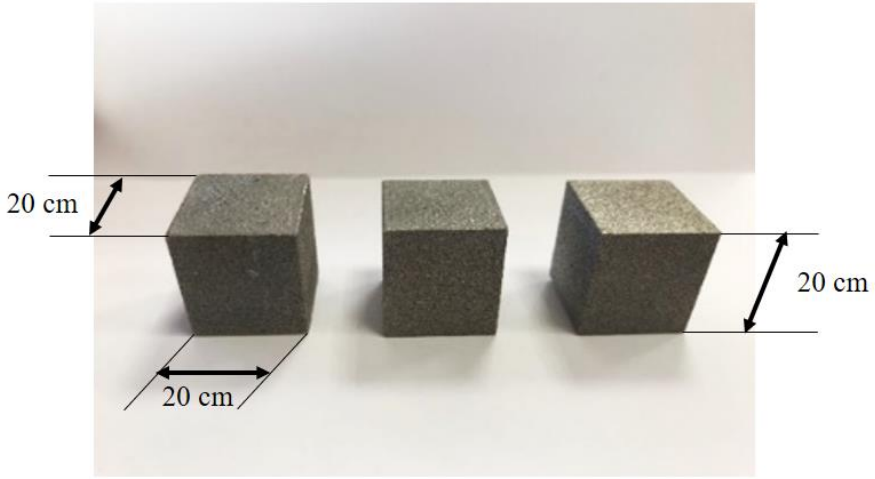

Figure 4. 1: Illustration of AlSi10Mg specimens generated by additive technology.

4.1.2 Heat treated SLM samples

Not only as-built SLM specimens were employed in this study, but also heat treated samples. The specimens consist of 30 μm-powder based sample sintering that submitted a progressive temperature increasing, specifically 200ºC per hour, reaching 300ºC. Afterwards, an isothermal process followed, that is 300ºC during 2 hours. Finally, it experienced a gradual cooling in furnace. The thermal history can be depicted with the **Figure 4.2**.

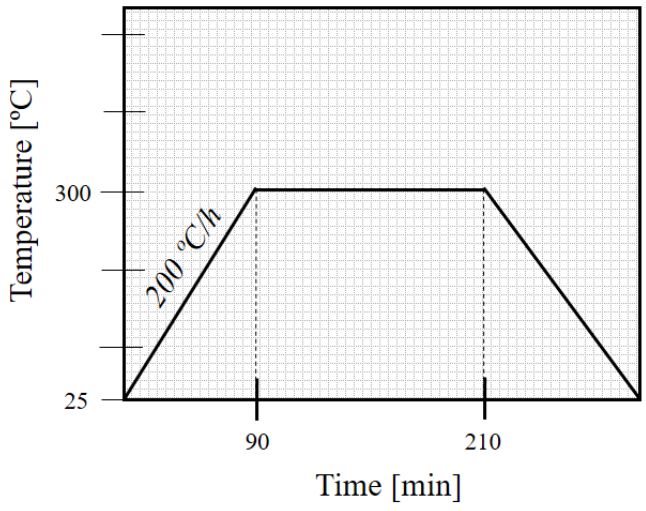

Figure 4. 2: Thermal history for heat-treated specimens.

4.2 Presentation of the selected samples

As one of this thesis main goal was to evaluate the influence in corrosion of the way a SLM material is sectioned then, for every ***AP*** and ***HT*** sample, two more were generated: one perpendicular and the other parallel to the metal's building direction like seen in **Figure 4.3**. To better distinguish both of them, the even numbers will indicate that it is a parallel sectioned sample, whereas the odd will designate the perpendicular ones.

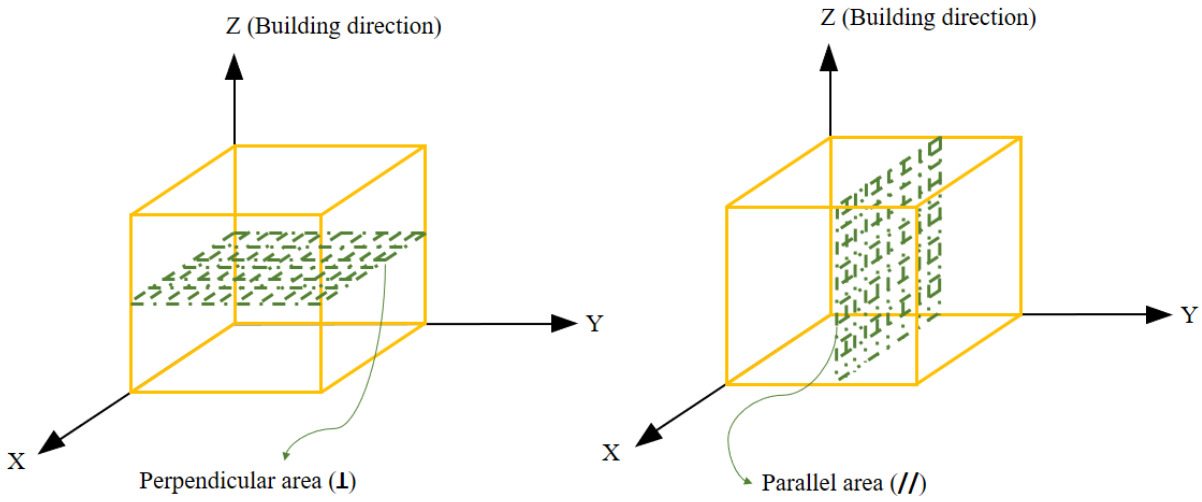

Figure 4. 3: Schematic representation of sectioned perpendicular and parallel area.

In order to provide a clearer presentation of the different samples, the **Table 4.2** is provided.

Table 4. 2: AlSi10Mg samples used in electrochemical tests.

Sample's designation	Typology
1-C	Cast
2-AP	//
3-AP	⊥
4-HT	//
5-HT	⊥

Over the course of this thesis' experimental tests, some of the initial samples suffered deterioration on its protective sheath (the making and purpose of the sheath will be explained in *Section 4.3.2*). Therefore, they ought to be replaced with another one identically built and sectioned. It is clear that this new sample would have a different exposed area, necessary

parameter for the forthcoming analysis. Nonetheless, all of the similar built and sectioned samples, even though they differed only on this area value, were considered as to be one due to the hypothesis of replicable data, which allows future research to obtain similar results if conducted in similar manner.

4.3 Working electrode preparation

4.3.1 Sectioning

In order to properly set the electrochemical cell instrumentation inside a beaker, the alloy sample should be adequately prepared. This means that the dimensions of the starting sample, which initially were 20 mm^3 for SLM samples like depicted in **Figure 4.1**, ought to be diminished using a cutting machine.

By proceeding like this, rectangular samples from 0.6 to 1.5 cm^2 of exposed area were created, with a height of nearly 0.5 cm. Regarding the cast samples, that is the ones not manufactured by SLM, circular and higher exposed area samples were produced (3.14 cm^2) whereas the height remained, in general, the same.

Furthermore, this operation was performed to obtain both parallel and perpendicular surfaces and thus, study if and how it influences the corrosion mechanism.

4.3.2 Mounting

Once the dimensions where as desired, it was necessary to create an appropriate insulating sheath surrounding it. There are several reasons why this mounting procedure is advantageous to be performed [65]. One of them is to ease the future handling of the sample as it will be submitted to polishing, cleaning, electrochemical tests and polishing again. Apart from this, it is important to study a constant surface dimension over the several tests, and this can be accomplished by creating the mentioned sheath as only a surface, rectangular or circular, will be exposed.

Firstly, a wire was attached to the sample by means of a silver glue that ensured the continuous passage of current (essential requirement in the cell's assembling). Secondly, the resin preparation was made and then poured in a specific silicon mould that contained the previously prepared sample at the bottom of the mould. This proceeding is known as *cold mounting*; which is preferred over *hot mounting* in samples because the consecutive high temperature effects are not desired. After waiting a couple of minutes for the appropriate resin solidification, the result illustrated in **Figure 4.4** was obtained.

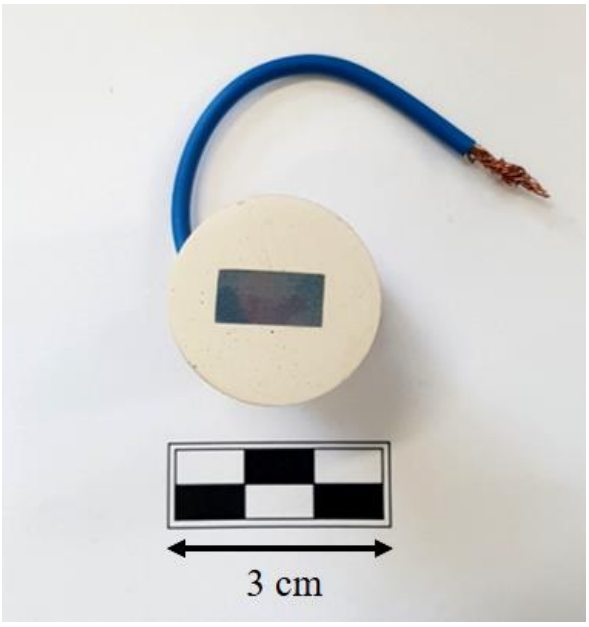

Figure 4. 4: Finished sample assembly

4.3.3 Polishing

On the basis of experimental research conducted [22] it is known that corrosion behaviour differs whether a polished or unpolished surface is attacked. It was found that this difference was related to the surface morphology, specifically the characterizing roughness, and the consequently quality of the oxide coating that is formed. Hence, these results are not linked with the microstructure and its effects on corrosion.

Therefore, it is evident that the electrochemical tests cannot be performed with as-received specimens without a further treatment to the exposed surface. In fact, polishing is the universal employed technique. Its main goal is to obtain a uniform and smooth surface that is suitable for a corrosion study, free of any corrosion products remaining, which can even affect the sample up to a considerable depth. If these remain before initiating a new test, then the results will no longer be reliable.

The instrument used for this goal is the polishing machine "Mecatech 234" (**Figure 4.5**). The operation was performed manually.

Polishing a sample consists of using a series of special polishing clothes or abrasive papers which are mounted in the mentioned polishing machine. They are characterized by its grain designation and there are many grit standardizations as the American or European ones, but in this thesis the latter one is going to be used (Federation of European Producers of Abrasives: FEPA).

In order to perform a successful polishing, the first abrasive papers that should be used are the coarse ones, followed by the ones with finer grits. Usually, the first used is the P300 in order to easily remove a significant part of the corrosion remains. Afterwards, the progressive papers used where P800, P1200 and P2000 which provided a more uniform surface, at a microscopic level.

The samples used for polarization tests did not submit further polishing. Conversely, those destined for impedance tests were polished also with P4000 followed by polishing clothes together with not only a special diamond solution with 1 μm particles but also a lubricant

reflex lube. The result of this last polishing differs in the final surface result, which is shiner and gives a mirror finishing.

Figure 4. 5: Illustration of the polishing machine used along this thesis' sample preparation. (Extracted from Presi catalogue [66])

4.3.4 Cleaning

The last operation for samples preparation is the ultrasonic bath. It is typically used on medical, electronic, optical and industrial applications for obtaining a highly effective cleaning result [67]. It consists of a tank filled with a sufficient quantity of water. The sample to be cleaned is immersed in a beaker containing a methanol solution, which is then immersed in the water bath. The explained configuration can be better seen in **Figure 4.6**.

Figure 4. 6: Ultrasonic bath configuration used for the sample cleaning.

In order to obtain a suitable cleaning result, the ultrasonic bath was conducted over three minutes at least. Afterwards, the sample was appropriately dried with compressed air and it was ready to submit the electrochemical tests.

4.4 Potentiodynamic tests

As it was introduced in the first chapter of this thesis, polarization tests are conducted in order to assess the metal's corrosion rate. This is possible because every corrosion process involves electrochemical reactions occurring at the interface between the metal and the electrolyte in which it is immersed in. The rate at which it develops depends on the equilibrium between the anodic and cathodic reactions. Both of them are characterized by a theoretical anodic and cathodic current and, by means of a potentiostat, it is possible to assess their sum when varying the applied potential.

Firstly, the open circuit potential (OCP) value is determined. This refers to the equilibrium potential achieved by the studied metal when no external electrical connections are present. With the aim of providing enough time for the stabilization of the equilibrium potential, it was performed during sixty minutes.

Secondly, the potentiodynamic polarization tests were carried out at a scan rate of 0.5 mV/s, being the starting applied potential: "OCP – 1.0000 V" and ending potential "OCP + 0.7000 V".

4.4.1 Electrochemical cell configuration

A potentiostat is used to vary the potential at a constant scan rate, measuring the resulting corrosion value and making use of a recording method to have afterwards these results available. For this thesis the potentiostat used was: Ivium-n-Stat multichannel electrochemical analyser.

The characteristic adopted configuration is a three-electrode electrochemical cell, composed by a working electrode (WE), a reference electrode (RE) and a counter electrode (CE). These three elements are immersed in an electrolyte solution which, for this particular thesis, is going to be a 0.6 M sodium chloride solution. This solution is commonly defined as artificial seawater because of its equivalent chloride weight percentage to the seawater. Nearly 250 mL are poured into an appropriate beaker. **Figure 4.7** graphically describes the positioning of each cell element.

The working electrode is clearly where the studied electrochemical reaction occurs. The reference electrode employed is the silver/silver chloride (Ag/AgCl) electrode which characterizes by a constant potential through time while no current passes through it [68]. Its use derives from the impossibility of using a SHE, which defines E^0 in *Section 1.1.1*, because of potential undesired reactions in the cell. Hence, a well-defined system with known potential vs. SHE is used to establish the new zero of the potential values (E). The counter electrode, also known as auxiliary electrode, is used to close the cell's circuit; this means that the current flows from the WE, through the electrolyte, to the CE. The one used was a platinum wire, which is an inert conductor.

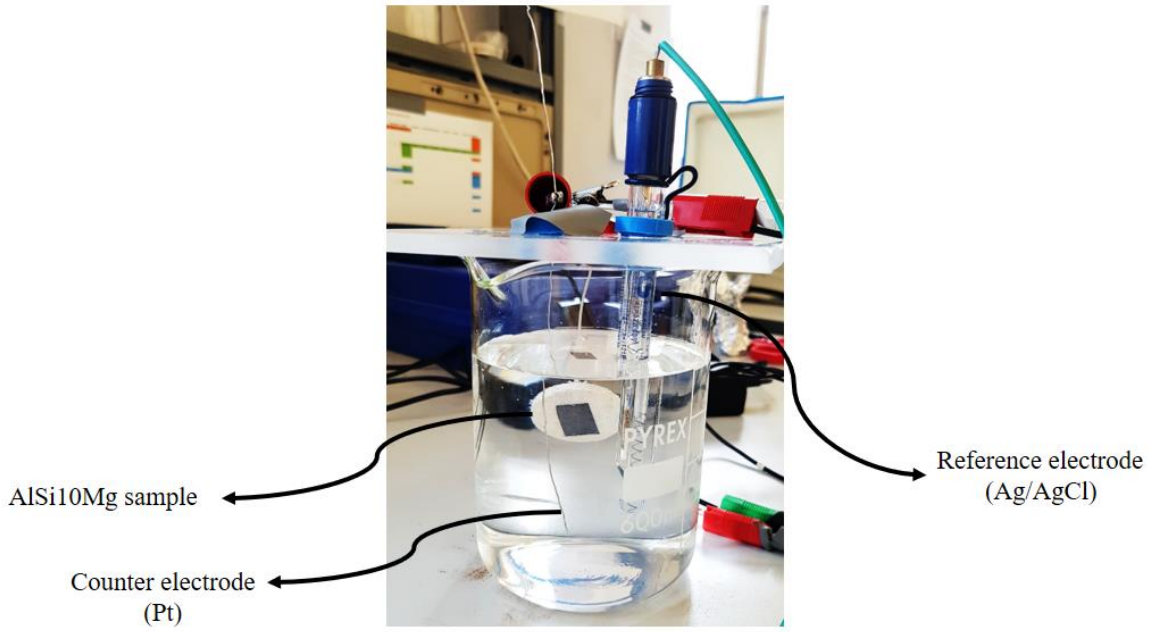

Figure 4. 7: Electrochemical cell configuration used for potentiodynamic tests.

The controlled and variable potential is established between the WE and the RE [69], applied by the voltmeter represented with a **V** in the **Figure 4.8**. Simultaneously, this generates flowing current between the WE and the CE, which is measured by the ammeter designated with a **G** in such figure. Both voltmeter and ammeter basically constitute the potentiostat apparatus.

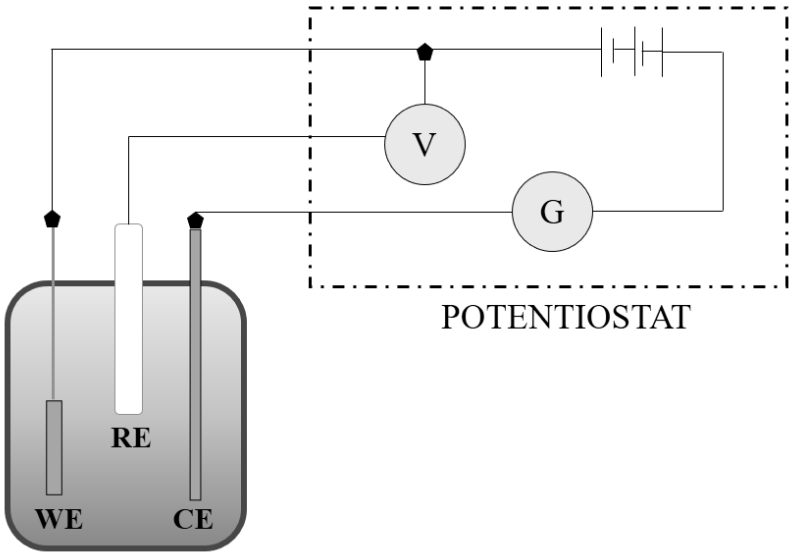

Figure 4. 8: Basic schematic representation of the electric circuit in electrochemical cells (Adapted from [69] with modifications).

It is important to notice that the selection of this electrolyte is due to the corrosion pitting that is commonly observed when working at a pH range between 6.5-7.7 and up to 80ºC, which largely comprises natural environments such as seawater, surface body of water and moist air [44]. Moreover, taking into consideration other oxidizing agents that could be used, chloride anions are the preferred ones for its particular potential to tear the naturally-formed coating apart due to its small dimension (close to that of oxygen) and good mobility. One feature that derives also from its size is the possibility to replace oxygen in the alumina network, thereby making it less resistant and enhancing the dissolution of aluminium. There exist other solutions which can affect more severely the corroding surface, like H_2SO_4, but are not entirely suitable to evaluate the corrosion behaviour of a metal due to its highly aggressive potential.

It is known that chloride concentration certainly affects the corrosion response, whether contributing to higher pitting depths or even increasing its density. Along with other parameters, like solution temperature, pH, moving or stagnant status, determine the resulting corrosion resistance. Nonetheless, these do not vary along this thesis electrochemical tests, therefore the corrosion rate will be only influenced by the microstructure characterization.

4.5 EIS tests

Impedance analysis are usually employed to obtain further and complementary corrosion information, to the ones obtained by potentiodynamic tests, because of its high sensitivity characteristic in generating and analysing varying frequency and phase signals [69]. Nonetheless, this information is focused mainly on evaluating the protectiveness of the naturally-formed passive film, reason why a representative RC circuit is proposed in order to fit the experimental data.

The same three-electrode cell configuration is used, but this time the imposed signal is a sinusoidal potential to the WE, then measuring the ac current which will present the same frequency value but a different phase value. Thus, by means of these two variable-in-time parameters it is possible to obtain the impedance value with equation (1.63) [8, 11]. For this purpose, a frequency response analyser is necessary. The scheme in **Figure 4.9** is presented as a representation of the configuration in EIS cells:

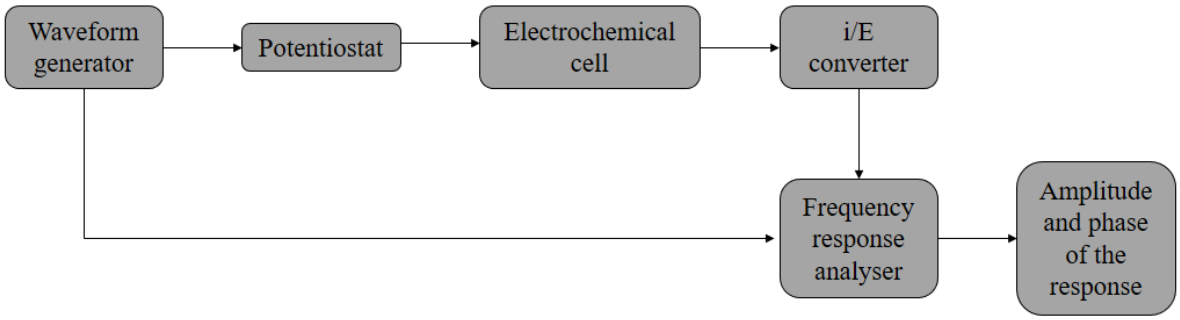

Figure 4. 9: Schematic representation of EIS experiments (Adapted from [9] with modifications)

For the electrochemical impedance experiments carried out in this thesis, the spectra were acquired with the application of a sinusoidal AC. This one presented a low frequency range of

10^{-2} to 10^{5} Hz, selected with the aim of not prolonging the experiment's duration as much [10]. Simultaneously, the imposed stimulation sinusoidal voltage between the WE and the RE was of 0.01 V.

4.6 Ancillary instrumental material

4.6.1 Field Emission Scanning electron microscope

Also known with the acronym FESEM, represents a wide use electron microscope type in not only in metal microstructure characterization but also in many other fields like cell biology, where a detailed study of a surface is needed. Even the characterization of textures is possible thanks to the electron beam utilized to regularly scan the material surface [70]. The scanning procedure consists basically on the reaction of the surface to this beam by producing a high-energy backscattered emission and a low-energy secondary electrons emission both directed to a detector. An important condition that arises from the functioning system of a FESEM is that the material has to possess electrical conductivity [71] to provide such responses.

Among the basic elements that constitute the FESEM equipment, the one placed at the top of the electron column would be the electron gun, under which places an anode through which the electron beam begins its path [70], as **Figure 4.10** shows. Even if several elements are there depicted, only an insight of the parts essential to understanding the functioning of the FESEM is going to be provided in this thesis.

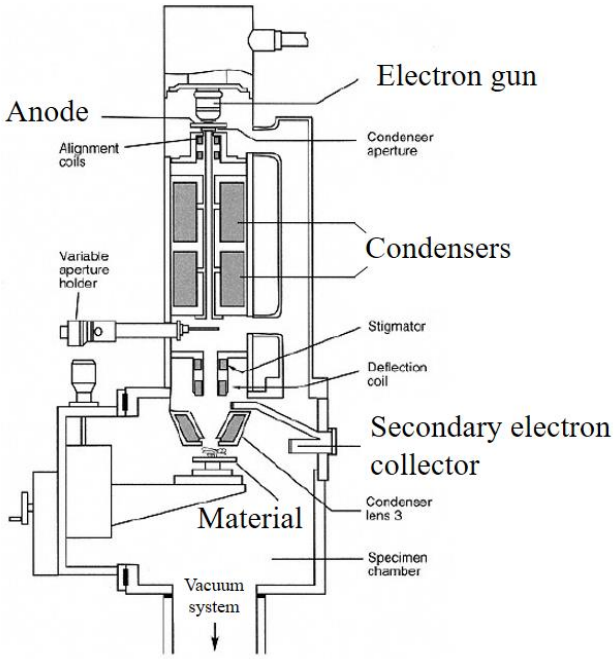

Figure 4. 10: Diagram of FESEM principal equipment components (Extracted from [71] with modifications)

Follows the anode constituent a series of electron lenses that accurately guarantee a small and concentrated path for the beam [71, 72]. These perform the scan deflection function of a

FESEM, essential because the beam produced by the mentioned gun has a spot size too large to ensure good quality image; therefore, a demagnification step solves this problem. Once the beam passes through all the required lenses it reaches the material of interest up to a depth of a micrometre, this latter one generates a special response upon which the image is being made. The superficial layers of the specimen generate secondary electrons, varying always as the electron beam reaches different points of this surface. The electrons arrive to an appropriate collector and are then processed creating a singular series of pixels, image elements, on a monitor and characterizing that singular point on which the beam had initially struck.

Throughout the entire column a vacuum condition is provided to prevent the presence of different gas molecules present in air that adversely influence the electron beam's passage towards the material and the electron response pathway to the collector.

5. EXPERIMENTAL RESULTS AND DISCUSSION

5.1 Microstructure characterization

To outline the main characteristics of each sample's microstructure, the Scanning Electron Microscopy was employed due to the high resolution imagining that it provides.

5.1.1 Cast sample

For this case, FESEM micrographs of both low (**Figure 5.1-a**) and high (**Figure 5.1-b**) magnifications are here presented.

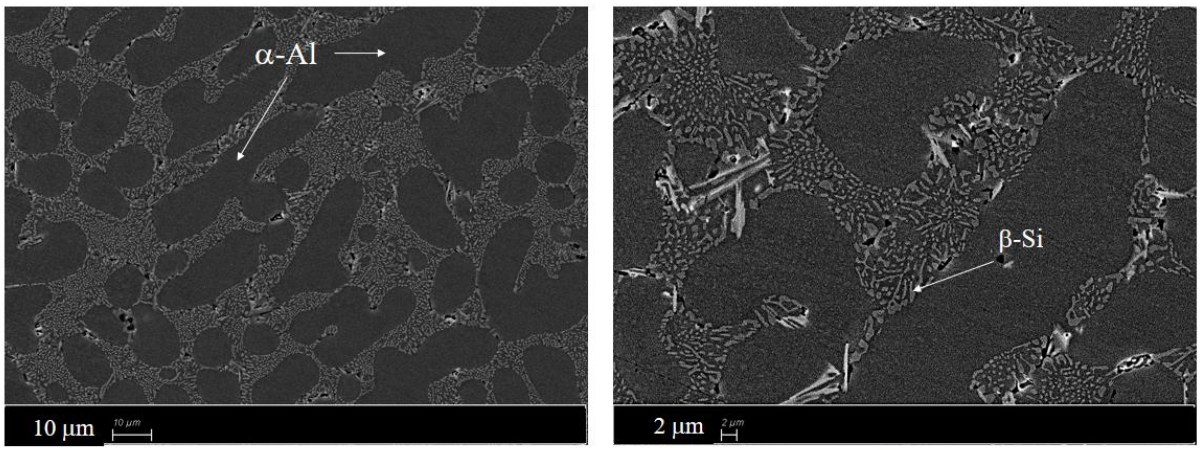

Figure 5. 1: FESEM images depicting cast microstructure at lower (a) and higher (b) magnifications.

At lower magnifications it is clearly seen the primary α-Al phase depicted as large continuous rounded configurations, some of these are quite equiaxed and others are more elongated. As an average diameter for the equiaxed elements 16 ± 4 µm is deducted, whereas the second ones have a length of 37 ± 12 µm. Meanwhile, the eutectic silicon phase is depicted at higher magnifications like an acicular discontinuous phase, placed at the boundaries of the primary phase. Although the detrimental ferrous phases are formed because of the slow cooling rates in comparison with SLM samples, these are not observed at the present magnifications.

If even higher magnifications are performed (**Figure 5.2**), the characteristic microstructure of the silicon-rich phase seems to present small rounded conformations with diameters of less than a micrometre and quite elongated thin structures of 12 µm long. The importance of showing further detail on this eutectic phase is to completely appreciate the discontinuities that it presents, being thereby not entirely acicular and presenting even larger conformations. Moreover, the large number of pores, also detrimental to corrosion resistance, are distinctly shown.

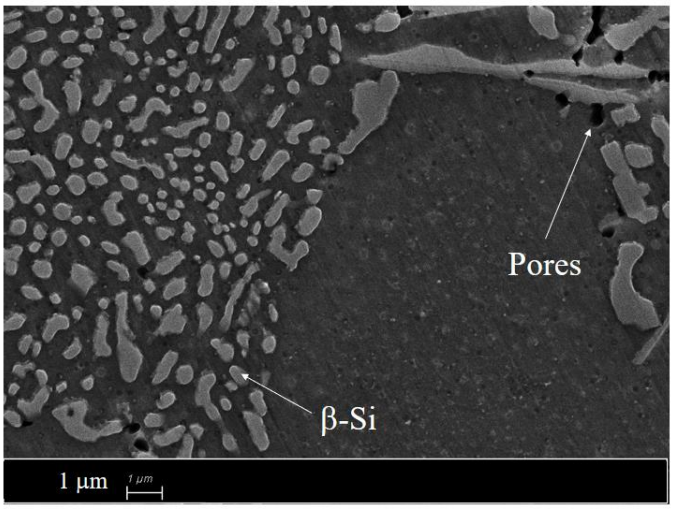

Figure 5. 2: Higher magnifications on cast microstructure.

5.1.2 AM sample: as printed

At lower magnifications it is possible to see the morphology characteristic of the molten pools. **Figure 5.3** illustrates FESEM micrographs obtained for as-printed samples, both in the parallel and perpendicular to the building direction surfaces:

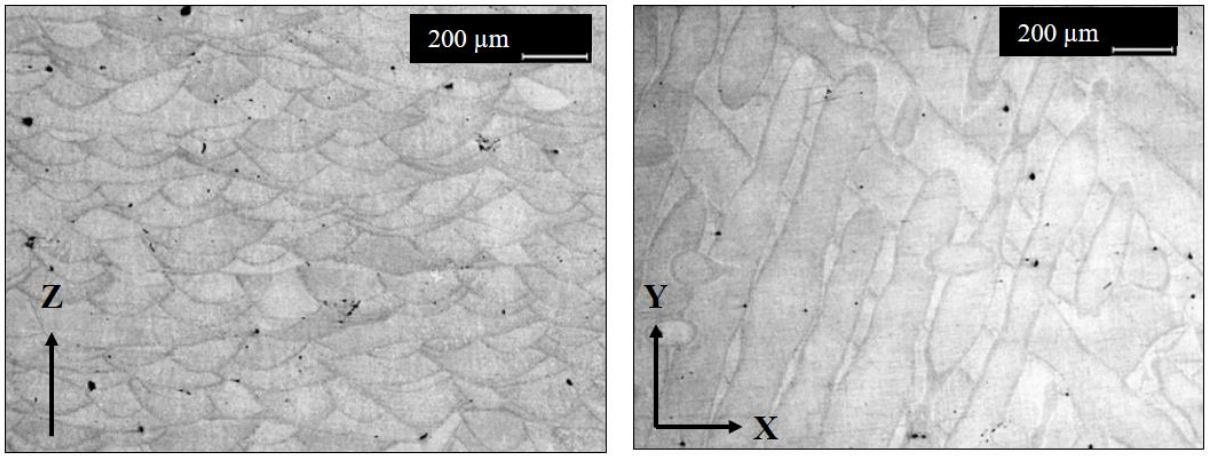

Figure 5. 3: Optical micrographs of parallel (a) and perpendicular (b) surfaces with respect to the building direction.

What is acknowledge from this last picture is the reflection of the scanning strategy that was adopted when sintering the metal part (**Figure 5.3-b**); which reveals the melting of a layer approximately perpendicularly with respect to the underneath one. In fact, this rotating angle was set to 67º. Moreover, each molten pool in **Figure 5.3-a** is not entirely exposed as there is often a certain overlapping with the adjacent melting track, just like with the next sintered layer above. This means that the mentioned zone is melted twice [58] or that it submitted an additional heating cycle with respect to the rest of the melted zones.

When analysing the XY plane, the melting tracks are not uniform and the downward layers can also be seen. This was addressed by some investigators [73] like a consequence of the different depths achieved by the several beam-melted tracks, which create different overlapping and therefore different microstructural aspects.

The melt pool formations are characterized by a depth of 115 ± 15 μm and width of approximately 142 ± 68 μm. The height of the powder bed (30 μm) and the hatch spacing (190 μm) used in the manufacturing phases explain the subsequent overlapping of adjacent molten pools as well as the appropriate junction or wetting with underneath layers. Some porosity was also individuated in both parallel and perpendicular surfaces, presenting dark colouration and nearly round shaped in **Figure 5.3**. These are mainly located at melt pool boundaries, where the irregular shape is considered to be a consequence of un-melted powder or non-perfect overlap between adjacent melted tracks [60]. Meanwhile, the more rounded pores are likely to result from previously entrapped gas. Other authors [26] attribute the porosity defects as a results of residual oxygen provoking aluminium oxidation. Even if the AM process is carried out at an inert atmosphere, there is commonly a quite low percentage of oxygen present that can certainly induce the formation of undesired oxides at the exposed surface.

As previously explained in *Section 3.5*, each molten pool shows a specific microstructure consisting of a columnar dendritic α-Al matrix in the parallel face (**Figure 5.4-a**) and more equiaxed in the perpendicular one (**Figure 5.4-b**), presenting higher concentration of silicon at grain boundaries and evenly distributed eutectic Mg_2Si. The α-matrix contains a small amount of silicon particles and it is actually a supersaturated phase [74]. If fitting the microstructure through Selected Area Electron Diffraction (SAED) technique, a face-centered cubic Al lattice and diamond-like cubic Si [75] were the specific characterizations found for this components.

Concurrently, this particular network becomes more expanded and even presents discontinuities at the XY molten pool boundaries, like depicted in **Figure 5.4-b**.

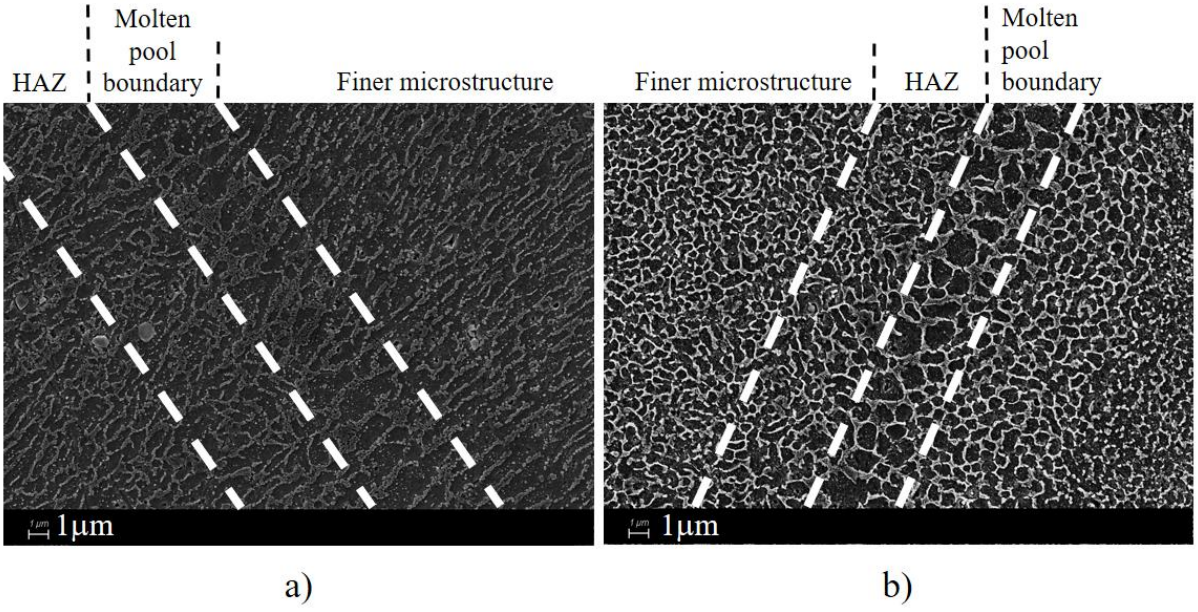

Figure 5. 4: FESEM micrograph of a) XZ plane and b) XY plane. Sample: SLM as-printed AlSi10Mg alloy.

It can be evaluated that the finer dendrite zone in the perpendicular plane presents a spacing of 0.48 ± 0.16 μm between each dendrite arm, whereas in the boundary zone it increased to 1.84 ± 0.88 μm. For the parallel plane the distancing was assessed not in the longitudinal direction but on how thick was the spacing between two parallel dendritic arms. The results were 0.48 ± 0.16 μm and 1.24 ± 0.24 μm for finer and coarser zone correspondingly. This differentiation was addressed by some authors [55] as a consequence of the different diffusion rates that overcome silicon when encounters diverse cooling process throughout the molten pool. Hence, lower cooling rates at the limiting zones explains the coarser microstructures. It is important to note that even if the two parallel and perpendicular finer zones presented the same spacing values, the aluminium cell in parallel surface have higher surface areas.

Furthermore, different dendritic morphology is seen between the XY and XZ planes. For the perpendicular one, nearly rounded dendritic cells are seen; whereas for the parallel plane they become more elongated. This phenomenon is explained by the characteristic way in which grains grow along the building direction (XZ plane), usually known as columnar. During this process, aluminium matrix makes use of the dendrite present in the finer zone as a way of growing epitaxially into the coarser grain zone, which tends to lengthen the dendrite arms towards the molten pool boundaries. Other authors [76] have reported this morphology to the thermocapillary convection within the molten pool and the heat dissipation phenomenon.

5.1.3 AM sample: heat treated

Some post-processing techniques are usually applied as a way of diminishing the remaining stresses and increasing the ductility [23]. In fact, research [56] has provided evidence for ductility increment, from 2% in as-built specimens to 17% in heat-treated at 300ºC for two hours. Meanwhile, the micro-hardness values decreased 127 ± 5 $HV_{0.5}$ to 81 $HV_{0.5}$. This ductility level was the highest found between several other treatments, like two-hours 450ºC, or with artificial ageing. Nonetheless, the resulting hardness was not the most desirable.

All these mentioned effects are directly related to the microstructure that arises from heat treatments applied to SLM alloys, like the FESEM image presented in **Figure 5.5**.

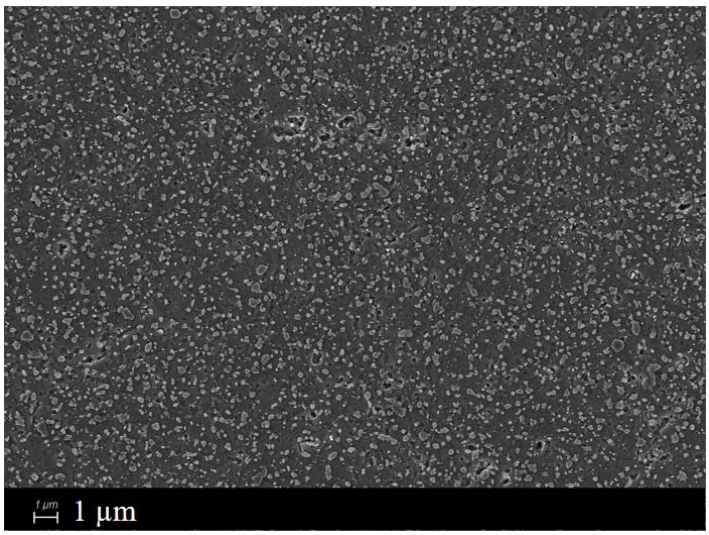

Figure 5. 5: FESEM micrograph of XY surface of heat treated SLM sample.

It is clearly seen that the microstructure has become coarser after annealing treatment, losing the characteristic interconnected dendritic coral-shaped network of silicon in additive aluminium alloys [56, 57]. By contrast, in HT specimens the previous silicon phase surrounding the supersaturated Al matrix form individual precipitates. These predominantly present a polygonal shape, like depicted in **Figure 5.6**, with a size that rises as the temperature in selected treatment is increased.

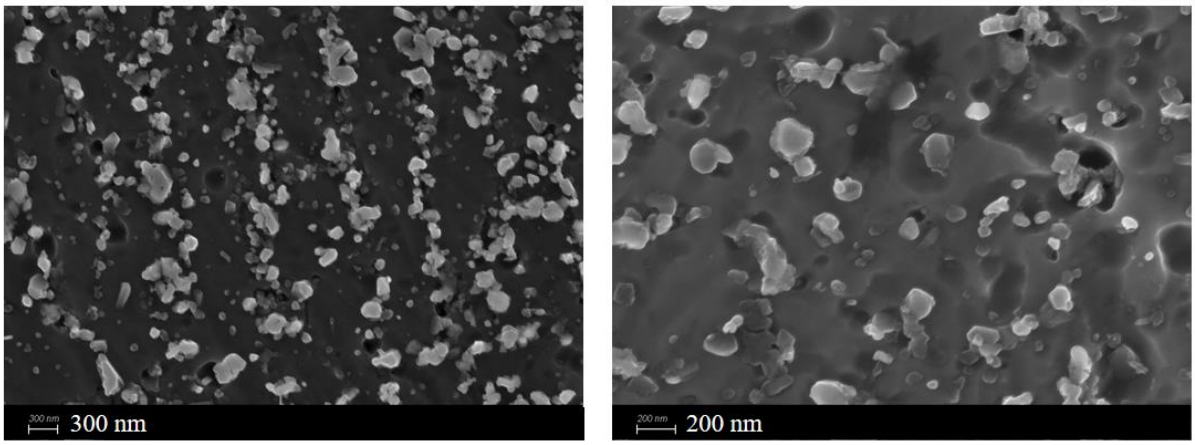

Figure 5. 6: High-magnification FESEM micrograph of HT specimen: XZ (a) and XY (b) surfaces.

According to the previously presented figure, isothermal 300ºC two-hours treatment generates precipitates with a diameter size of 160 ± 64 nm for perpendicular and 333 ± 166 nm for parallel planes. These results of shape and size are in good agreement with research conducted by Iturrioz, A. *et al* (2018) [56], in which 0.1 to 0.6 μm silicon particles were individuated. Moreover, the *coarser* silicon particles are clearly seen in XZ planes following hatch overlapping, whereas fine Si particles are seen within the α-matrix, just like depicted in previously presented **Figure 3.9**.

The microstructure at lower magnification levels is not presented here as, like previous works depicted [77], no considerable changes were noticed at melt pool characterization after annealing process to AM aluminium alloys.

Further characterization can be achieved by differentiating the silicon particle density throughout the molten pool formations. As previously introduced in *Section 3.6*, Si particle density and sizes increase along hatch overlaps and decrease within track cores [58]. This can be clearly seen in hereunder **Figure 5.7**, where the track cores present considerably smaller precipitate sizes than the centered zone. Even more, further differences can be seen in both parallel and perpendicular surfaces showing, like the AM surfaces, more elongated characterization for the XZ plane. In fact, this plane depicts a microstructure that is more similar to its original as-printed one, following more markedly the initial silicon matrix. In contrast, more isolated silicon precipitations are depicted in the XY plane.

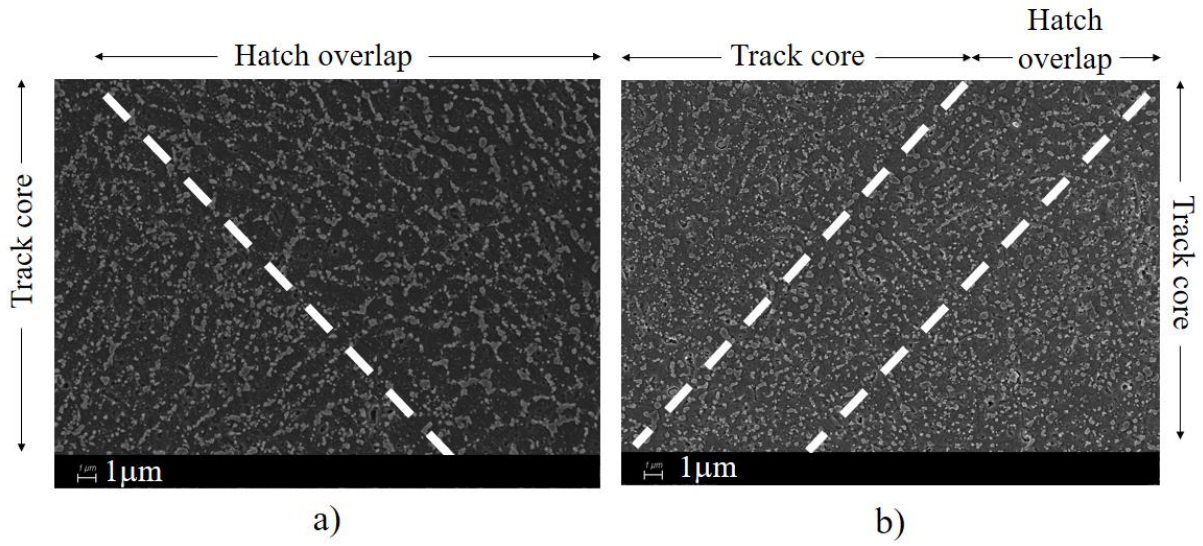

Figure 5. 7: Si particles density and size differentiation. FESEM micrograph on parallel (a) and perpendicular (b) surface of SLM heat treated aluminium alloy.

The mechanisms that undergo such mentioned precipitates was explored in prior studies [57, 58]. The different coalescence degree can be attributed to Ostwald ripening, which basically states the growth of large particles from smaller ones. This phenomenon is thermodynamically favoured as larger elements have lower specific surface, thereby proceeding into a lower internal energy system as particles increase their size. As a consequence, smaller particles prone to separate and diffuse towards larger ones. Moreover, interfacial disruptions in Al-Si interface create a local gradient in chemical potential with respect to the surrounding area; this furnishes the necessary energy for the atomic diffusion within solid state with consequent morphologic changes into spheroidal particles. This is what actually takes place in SLM specimens; where the molten pool cores present a finer microstructure which means finer matrix conformations compared to the boundaries network. This latter one is considerably coarser and sometimes even interrupted, circumstance which creates larger silicon formations.

It is essential to note that all of this spheroidal silicon precipitates do not only comprise the silicon content that was previously present surrounding the Al-matrix in as-built specimens, but also a fraction that formed part of the supersaturated cells. This was clearly addressed in studies conducted by Prashanth, K. G. *et al* (2014) [58] where a higher lattice parameter in the α- matrix was found for HT specimens, whereas the quantity of free silicon increased almost reaching that characterizing the cast sample.

5.2 Potentiodynamic tests results

The information that was obtained from these tests concerns the manner in which the current value changed according to the imposed potential variation. Even so, the initial step was performing sixty minutes of OCP determination, ensuring such time the reaching of the steady state as the equilibrium potential was achieved. In general, all the samples presented equal range for the OCP values, being around -0.7 $V_{Ag/AgCl}$.

In order to properly compare all the samples results, the resulting current *I* (which had ampere [A] as magnitude) ought to be evaluated over the working area of the exposed surface. Thus, the units for the hereafter plotted current density (*i*) were A/cm^2.

For every sample at least three repetitions in identical conditions were performed, following the objective/statistical approach. The plot in **Figure 5.8** was obtained for the cast sample.

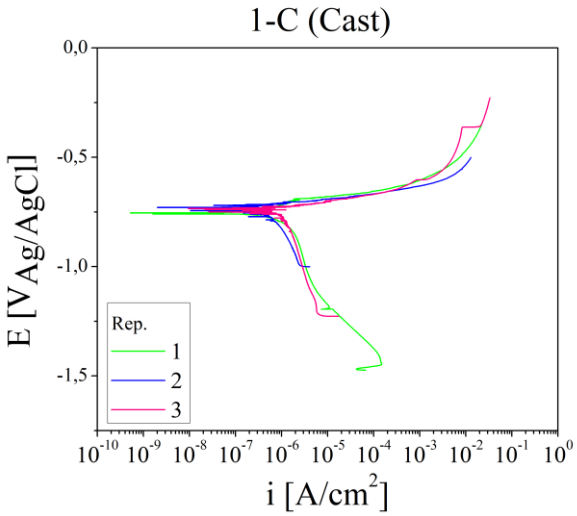

Figure 5. 8: Potentiodynamic response curves of Cast sample: 3 repetitions.

The cast sample showed dissimilar cathodic and anodic branches, as it will be seen henceforth, because the metal of interest is an alloy whereas for a bear metal the polarization branches would be symmetrical. Nonetheless, the three conducted repetitions present similar polarization characteristics. Conversely, for the AM samples more varied data is obtained like depicted in **Figure 5.9**.

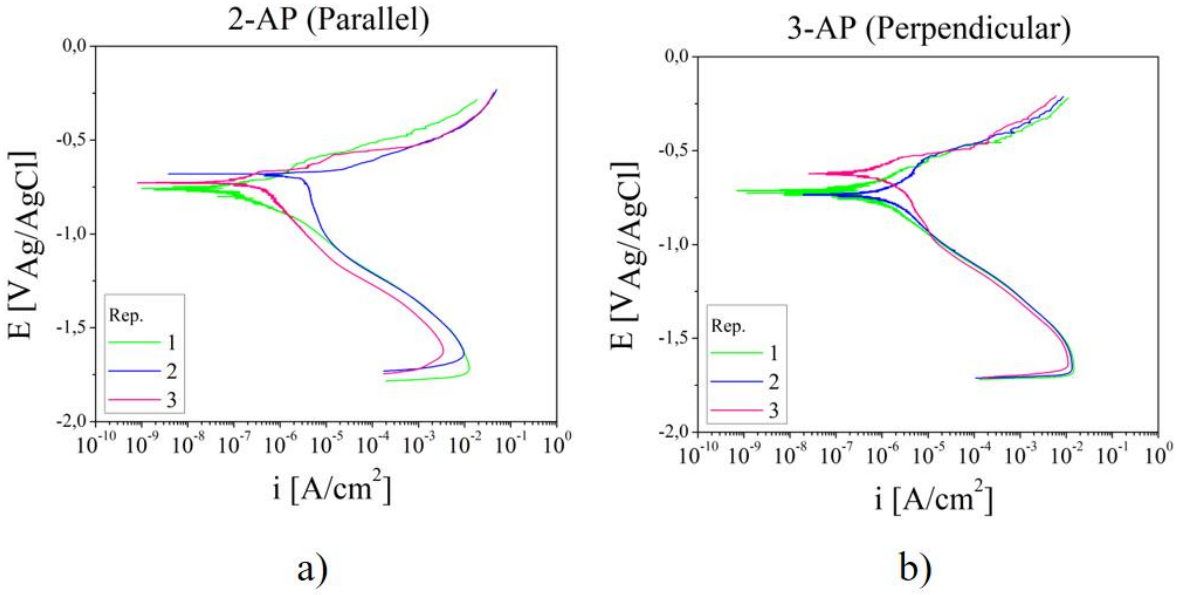

Figure 5. 9: Polarization curves for as printed samples: a) Parallel and b) Perpendicular planes.

Even if both plots show dissimilarities at a certain extent, perpendicular surface certainly displays higher variation, like the subsequent heat-treated case does; meaning that the repeatability of XY planes is higher than XZ planes. For heat treated specimens 4 repetitions were performed, obtaining the polarization plots illustrated in **Figure 5.10**.

The heat treated polarization curves, as well as cast curves, were in general more homogenous, among the different repetitions and both exposed areas, than the as-printed samples. Nonetheless, with the purpose of making comparison between them first repetition of the 2-AP sample and the second of the 3-AP one were considered as the representative ones. It results of interest to see if and how did the exposed surface influenced the corrosion behaviour of the AlSi10Mg. For this reason, the plots in **Figure 5.11** are presented.

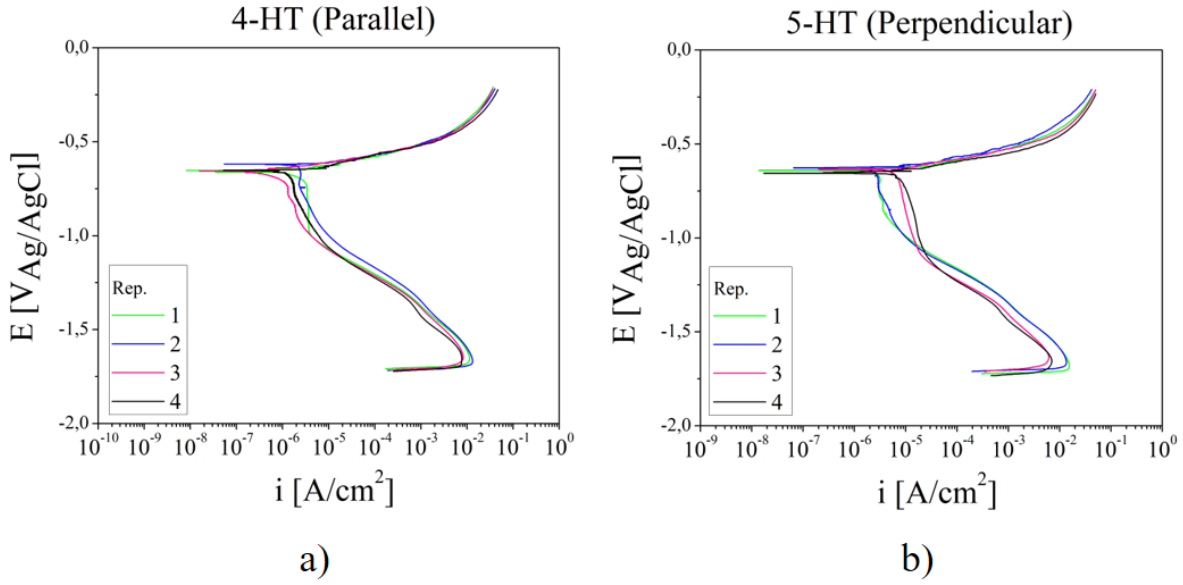

Figure 5. 10: Potentiodynamic response for heat-treated samples: a) Parallel and b) Perpendicular case.

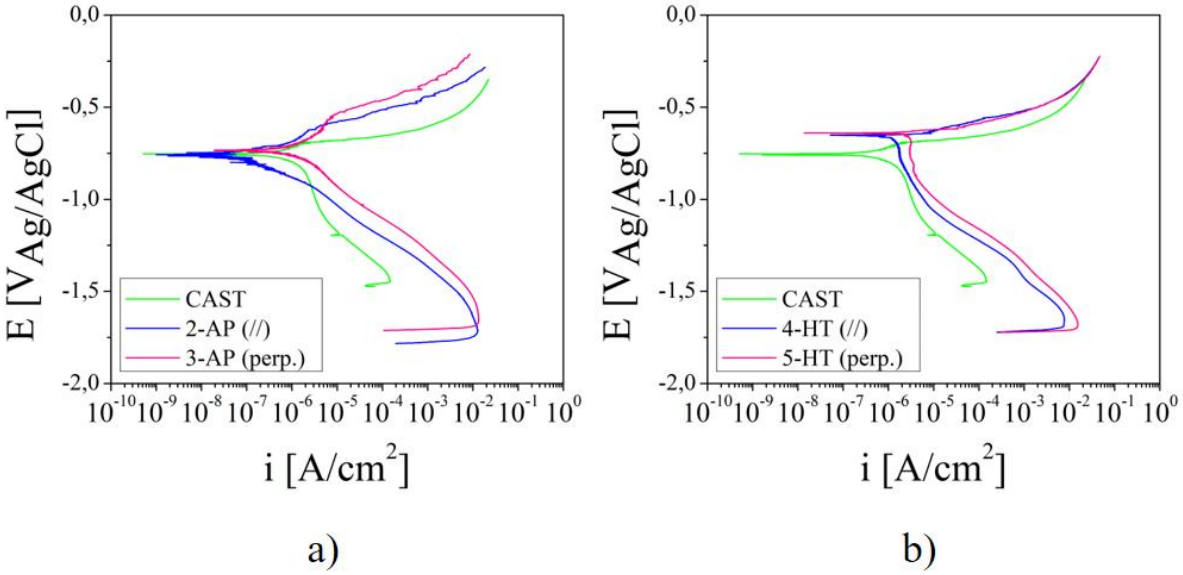

Figure 5. 11: Comparison of potentiodynamic response in a) As-printed and b) Heat-treated samples.

Compared with the cast specimen it is clear that additive manufacturing technology influences the polarization response, in part, by sharply elongating the cathodic branch towards higher current values. This branch showed, at more negative potential values, the concentration potential reflecting the diffusion control of the oxygen reduction. From – 1 V towards the OCP, the hydrogen reduction follows [78]. Moreover, both heat treated specimens show a similar shape which is different from the as-built ones; this implies that the corrosion process would develop through a different electrochemical characteristic mechanism [79]. The plot presented below in **Figure 5.12** graphically describes this differentiation.

It is clearly seen that HT specimens will present higher values of E_{corr} and i_{corr} compared to as built ones. Along with the different shapes presented, this evidence that heat treatment will certainly modify the alloy microstructure therefore modifying the corrosion progression.

Even if there are specific procedures for evaluating the corrosion resistance, a qualitative approach may be inferred from the last **Figure 5.12**. Every anodic branch, representing the metal corroding process, show how higher potential values must be applied for the same current response of as-printed samples compared to the cast. Therefore, higher corrosion resistance is given by AM samples. The heat treated specimens presented similar response, varying more noticeably the OCP value with reference to the cast example. Moreover, both AP and HT cathodic branches are quite similar compared to the anodic electrochemical behaviour, which certainly differs indicating that microstructure modifications will have a significant effect on the corrosion progress.

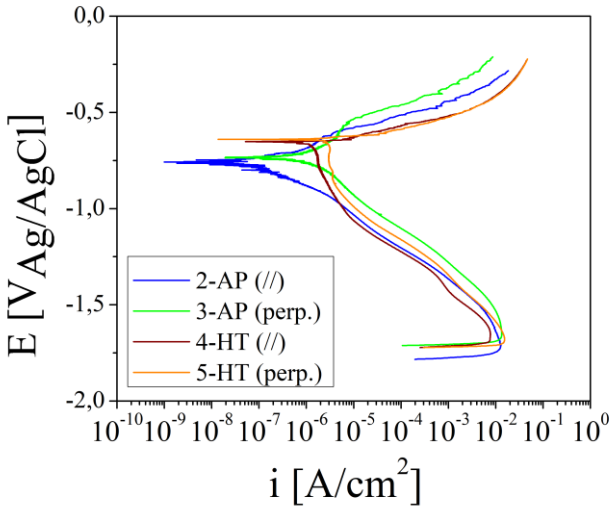

Figure 5. 12: Comparison of as-printed and heat-treated samples.

5.2.1 Tafel analysis

In line with the large number of corrosion research, Tafel Analysis was performed for each of the polarization curves. Like descripted in *Section 1.3*, by evaluating the Tafel anodic and cathodic slopes, along with the corrosion current (i_{corr}) it is possible to evaluate the polarization resistance. In the present study, the slopes were determined via the software *Ivium Soft*, simply by selecting two points for each cathodic and anodic branch. By inserting the specific exposed area, the values of E_{corr}, i_{corr}, *Rp* and both slope values are reported as analysis results. The user interface from the mentioned software is illustrated in **Figure 5.13**, when a Tafel analysis on sample 4-AP was performed.

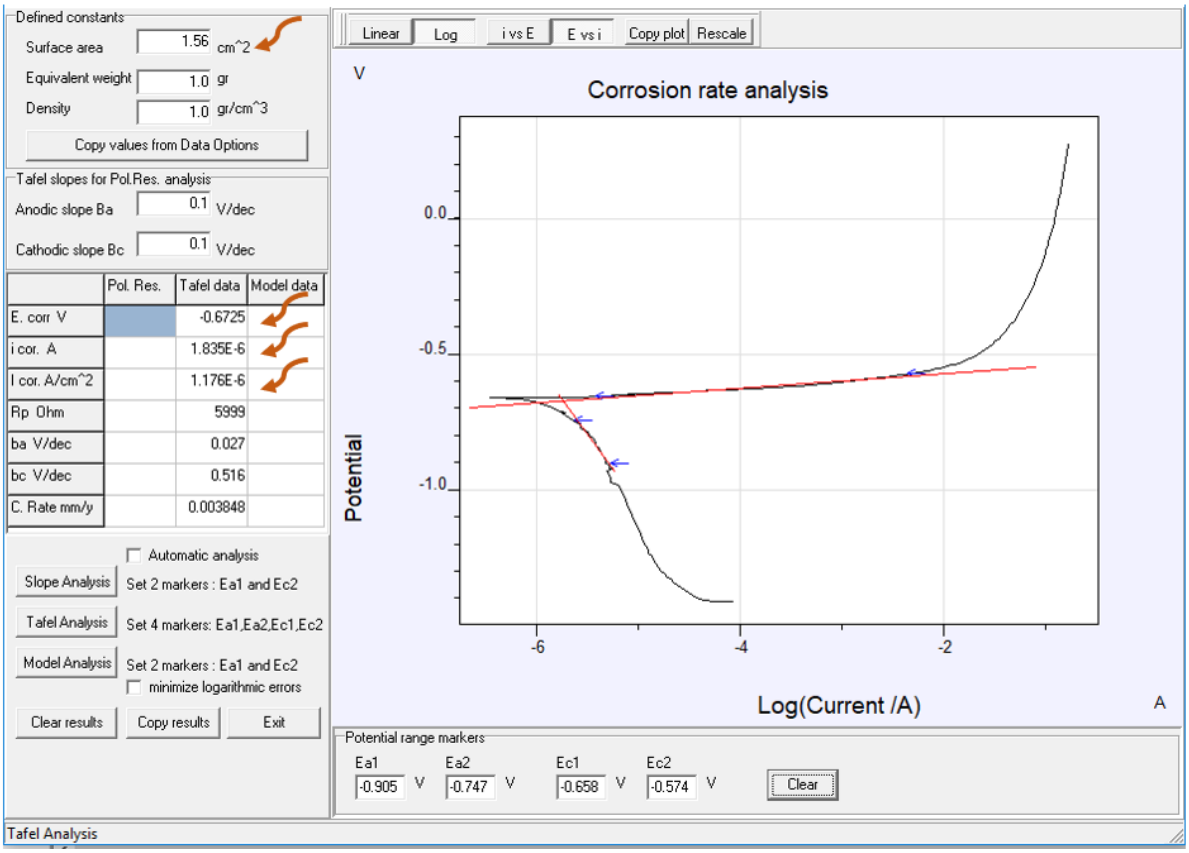

Figure 5. 13: *IviumSoft* user interface showing the Tafel analysis.

The useful information from this image are the i_{corr}, measured in A/cm^2, as the corresponding area value was previously introduced in the software, and the E_{corr} measured in V. The obtained results are summarized in **Table 5.1**.

Table 5. 1: Potentiodynamic results obtained from Tafel extrapolation analysis.

Sample	E_{corr} [$V_{Ag/AgCl}$]	i_{corr} [µA/cm^2]
1-C	- 0.750 ± 0.004	0.575 ± 0.067
2-AP (//)	- 0.739 ± 0.015	0.249 ± 0.128
3-AP (⊥)	- 0.678 ± 0.055	0.467 ± 0.170
4-HT (//)	- 0.652 ± 0.007	1.002 ± 0.473
5-HT (⊥)	- 0.641 ± 0.008	2.872 ± 1.331

The values for corrosion potential were, as introduced from OCP values, consistently around -0.7 $V_{Ag/AgCl}$. Nonetheless, cast sample exhibits the most negative value (-0.750 ± 0.004 $V_{Ag/AgCl}$); meaning that its corrosion is thermodynamically more favoured than for SLM specimens (-0.6885 ± 0.0655 $V_{Ag/AgCl}$), and certainly more than heat treated ones which presented the higher E_{corr} values of them all (-0.61 ± 0.049 $V_{Ag/AgCl}$).

When evaluating the kinetic factor, the values of corrosion current density are noticeably higher for heat treated specimens; whereas for as printed and cast they are quite similar. However, it is more illustrative to express this i_{corr} as a corrosion rate value (v_{corr}) measured in mm of metal penetrated per year (y). The following equation is employed; knowing that the specimen's density (ρ) is 2.68 g/cm^3, the exchanged electrons (n_e) in the dissolution reaction is 3/mol, the molar mass of the metal (M) is 26.98 g/mol and Kc is a conversion constant equal to 3.272 x 10^{-3} mm/(µA.cm.y) [79]:

$$v_{corr} = i_{corr} \frac{K_C.M}{n_e.\rho} \tag{5.1}$$

As a way of graphically present the obtained results, the plots in **Figure 5.14** were performed taking into account the medium and the standard deviation of each set of data:

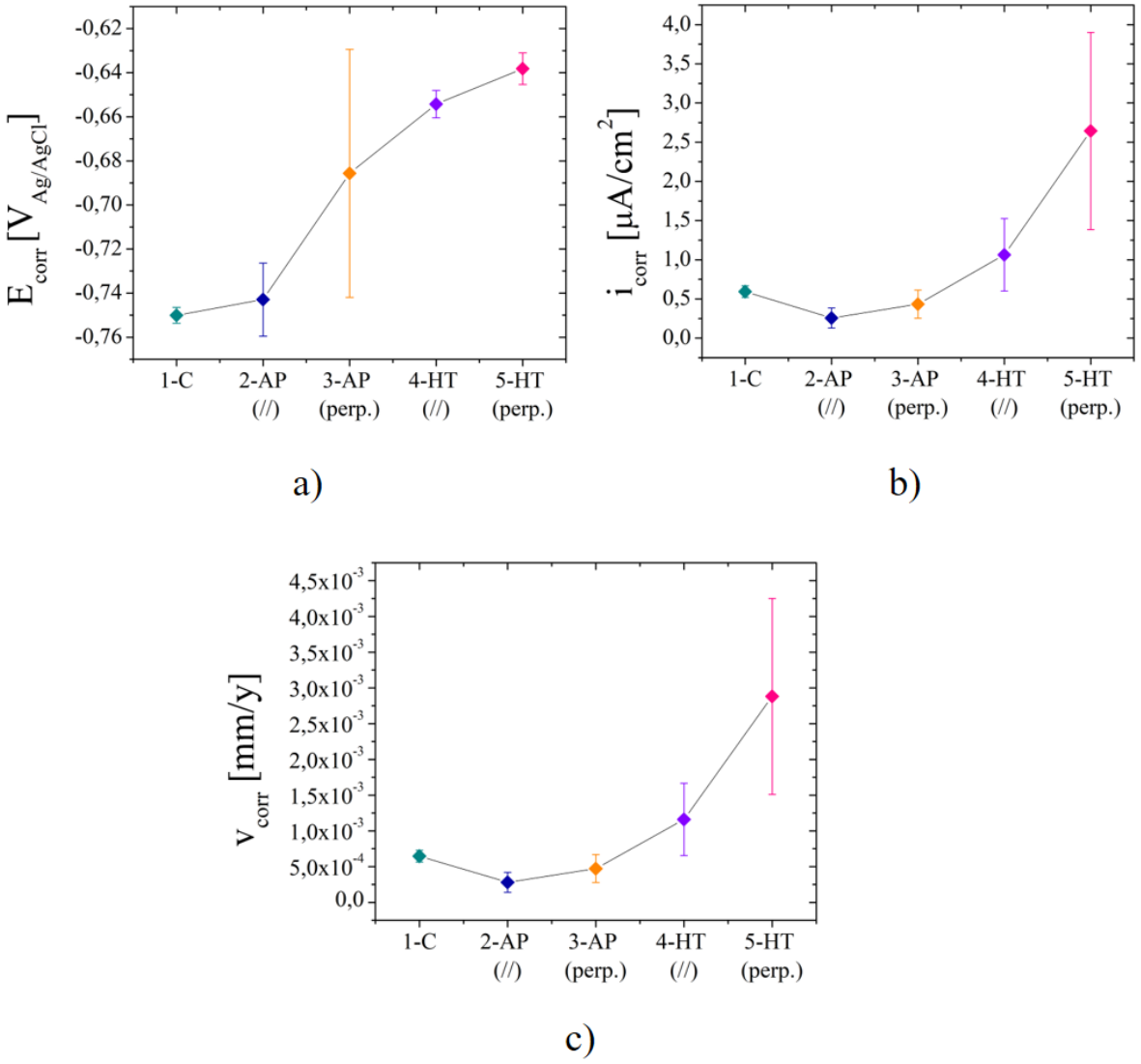

Figure 5. 14: Graphical comparison of all samples' results in a) E_{corr}, b) i_{corr} and c) v_{corr}.

Firstly, the corrosion rate values for SLM samples are lower than the cast metal; which is good agreement with some research [74, 80]. It is important to note that this is related to the particular microstructure that characterizes cast samples. In general terms, cast microstructure presents several intermetallic phases containing iron, like *β-Al5FeSi* and *α-AlFeSiMn*; and others including magnesium, for instance *π-AlFeMgSi*. These phases markedly increase the localized corrosion, as they are efficient on enhancing the breakdown of the passive film generated when exposed to corrosive conditions. Therefore, the resulting corrosion resistance is linked to the quality of the passive layer that is formed, regarding not only its thickness but mostly its composition and the eventual detrimental effects on corrosion response.

Moreover, certain studies [81] provided determinations through scanning Kelvin probe force microscopy (SKPFM), which made it possible to reveal the nobility of selected alloying elements within the α-matrix. The results reported higher nobility, i.e. less tendency to galvanic corrosion, of the Al-Fe-Si placed in the aluminium cells compared to the matrix itself, with values of +150 to +300 mV with respect to the Al-matrix. Similarly, interdendritic silicon eutectic particles presented higher Volta potentials with respect to the α-matrix, with voltage differences of 244 ± 50 mV.

The iron content in aluminium samples particularly has a critical effect on corrosion resistance. It is known that, even if present in lower quantities (0.20 wt% in AlSi10Mg sample) it forms a second phase due to its poor solubility in aluminium [82]. Iron is a noble metal, compared to aluminium, and therefore it was consistently reported that they influence on the anodic dissolution kinetics. This means that the intermetallic zones enhance the reduction of oxygen, which increases the pH in the vicinities. As a consequence, the surrounding aluminium matrix will be affected. In fact, the crevice zone limiting these intermetallic sites and the α-matrix are ideal for pitting initiation. As a way of supporting this trend, macroscopic corrosion morphology was previously presented in **Figures 3.2** and **3.3**, where for cast sample the pitting corrosion was particularly differentiated, but for AM-samples was not that evident as it presented mainly crevice corrosion. This last additive absence of pitting corrosion [60] was also addressed by other authors after performing potentiodynamic tests on non-polished surfaces, where no pitting attack was seen on FESEM low-magnification images.

The detrimental presence of Si-Mg segregations in cast aluminium alloys was documented by other authors [60, 22], who suggested a quite uniform distribution at higher magnifications. The greater corrosion rates of cast specimens can be attributed to the anodic sites that the presence of Si-Mg constituents generate, the irregular porosity, the higher content of free silicon and also the coarser dendritic aluminium microstructure.

Conversely, SLM processing generates peculiar and complex microstructures which principally characterize by a finer microstructure than casting produced ones. In this arrangement, the previously mentioned intermetallic phases might be present but in smaller amounts [80], specially the Si-Mg precipitates which certainly decrease corrosion properties. Moreover, the silicon content within the α-matrix is increased, producing that the driving force for the dissolution of the Al-phase is markedly diminished. This is apparently linked to the better corrosion resistance of AM samples, for which the rapid solidification process prevented the formation of such detrimental second phase.

Previous research made it possible to describe the preferential sites for corrosion in heat treated and for as-print samples as well [22]. It was exposed, by means of FESEM micrographs beneath the corroding surface, that for untreated specimens the pitting development followed molten pool boundaries; whereas a fairly uniform corrosion type

characterized the heat treated specimens. In agreement with some search results, parallel surfaces presented relatively lower corrosion potentials than perpendicular ones. This behaviour was seen not only for as-printed samples but also for heat treated, which suggests that there must be some feature that distinguishes perpendicular surfaces from parallel ones.

Some might attribute this difference between XY and XZ surfaces to the porosity density which, from low-magnification FESEM micrographs in **Figure 5.3**, is higher in XZ areas than XY. Together with the fact that parallel surfaces present higher concentration of molten pool boundaries [74] (preferred site for pitting nucleation); then what should be inferred is that parallel surfaces have greater possibilities or greater tendency to submit a corrosive attack. Surprisingly, this is inconsistent with general obtained experimental results. Actually, the main factor that contributes to a higher corrosion rate is the grain size as research has stated that, due to the nobility of silicon particles with respect to Al-matrix, rate increases as grain size decreases. If as-printed FESEM micrographs are analysed, the finer-dendritic zone of both perpendicular and parallel surfaces differ: the first one presents quite smaller grains whereas for parallel areas the grains are relatively elongated, therefore presenting overall higher grain areas. Even if these are not the preferred zones of corrosion attack, as some research may state [62], they ought to be considered as well as influencing factor on the overall corrosion response. As will be further explained hereafter, melt pool boundaries are the preferred sites for pitting initiation and therefore these grain sizes should be given higher importance. In fact, XY faces appear to have higher grain sizes as they are quite rounded if compared to the equivalent zone in the XZ plane. Nonetheless a more discontinuous silicon network is found for XY planes as well as a superior distancing between two dendritic arms, indicating that this is what ultimately enhances corrosion attacks.

Even if several properties enhance the corrosion resistance of SLM samples, there are others which decrease it thereby making these materials more vulnerable to corrosion attacks. By this last effect, the formed passive layer is referred to [60]; which is characterized by being less protective than the one that is formed during exposure to air conditions. It is because of this net result of either enhancing and detrimental effects, that the final corrosion potential is quite similar than the cast sample. In fact, if statistical analysis is made for the density corrosion current, then it is revealed that, at a 0.05 significance level, the population means of as-printed and cast are not significantly different.

A second detail that is worth explaining in order to understand more completely the corrosion response, is the preferred site for localized corrosion attack. We are talking about molten pool boundaries. These locations are characterized by a higher grain size in both parallel and perpendicular faces, compared to the HAZ and finer-dendritic zone. However, the fact that mainly differentiates it from the rest of the microstructure is the fraction that Al cells comprise within these vicinities, which is clearly higher. Hence, having coarser silicon particles, a matrix which is predominantly interrupted and vulnerable zones for sintering defects presence, make these boundaries more feasible to α-Al dissolution or to be corroded. Simultaneously, other research works [80] ascribe this preferential proceeding path to the higher porosity levels that this limiting zone presents when compared to the rest of the molten pool formation.

Meanwhile, previous observation of micro-cracks at this limiting zone was accurately attributed to the remaining residual stress from conventional additive procedures [83] and thereby confirms that it is a preferred zone for corrosion attack. Conversely, for 350ºC treatment, no localized micro-cracks were noticed after the same exposure time, providing further confirmation to a generalized oxidizing process in heat treated samples. These different trends are linked with the values encountered for the E_{corr}, as greater amount of

preferred sites are present in AP samples, whereas a more general corrosion type in HT is thermodynamically less favoured.

For the case of heat treated specimens, it was reported that annealing conditions have a direct effect on the oxide film that is formed in comparison to as-printed samples [39, 77]. Temperature procedures increase the thickness of the porous layer formed upon the compact layer, which is regularly generated within the first seconds of exposure to corroding environments. Although this might be seen as a favourable effect on corrosion resistance, because it is thicker and with higher crystallinity index, annealing processes also induce a porous and micro-cracked layer configuration. Therefore, corrosion would be kinetically more favoured for HT specimens as seen in **Figure 5.14-b**. The fact that the silicon content, previously being part of the α-matrix, is now forming part of the silicon precipitates (*coarser* Si) and free Si precipitates (*finer* Si) generates a primary phase which is richer in aluminium. Hence, the potential difference between this anodic phase and the nobler silicon conformation increase, thereby raising the corrosion rate. Moreover, the increased presence of the Mg_2Si phase, corroborated in certain XRD studies [62], do suggest that this evolution of precipitates effectively increases the corrosion rate by creating further microgalvanic couples with the α-matrix.

Conversely, when analysing their E_{corr} values (**Figure 5.14-a**) HT exhibited the highest values, which is in agreement with research results [79], indicating that the pitting initiation is thermodynamically more favoured. This is precisely in agreement with the kind of corrosion that HT samples show, which is mostly a uniform attack compared to the preferentially pitting attack for AP (molten pool boundaries) [77]. At a microstructure level, this higher uniformity in the attack is attributed to the also homogeneous microstructure, consisting of silicon precipitates instead of a more differentiating dendrite configuration like in as-printed. In spite of this apparent advantageous effect, it enhances the breakdown of the passive film indeed, causing higher corrosion rates like seen in **Figure 5.14-c**.

The different corrosion resistance between the parallel and perpendicular planes in HT samples can be ascribed to the differences depicted in both microstructures. Evidently, as the silicon particles form fairly separated individual conformations, like depicted in **Figure 5.7-b**, corrosion resistance is diminished. By contrast, parallel planes present a distribution of silicon precipitates which assimilates to its original as-printed conformation. Having a microstructure that is more regular, less interrupted or less scattered than the perpendicular plane reveals to be a condition that enhances the corrosion resistance.

5.3 Impedance tests results

For each AM-sample impedance measuring, data collection was performed after the first, third, fifth hours and each day for 7 days (168 h). In the course of this work it was noticed that the first five hours' spectrum were considerably diverse from the rest of the results, as shown in **Figure 5.15** with the Bode plots for the fitting results of the 2-AP sample.

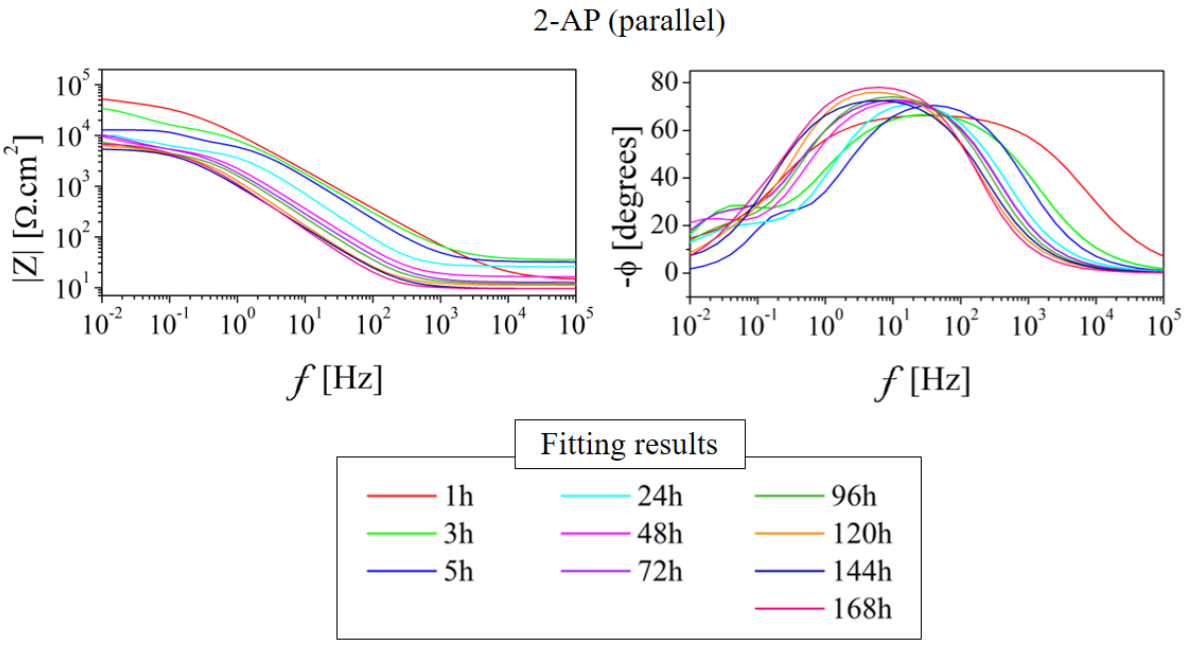

Figure 5. 15: Fitting analysis results for sample 2-AP using RC equivalent circuit presented hereafter in Figure 5.16.

Therefore, the key data that is going to be here presented along with the fitting analysis are the ones corresponding to 1h, 24h and 168h after initiation of the test, as they represent the initial, the final and the intermediate behaviour of impedance response. The so called "final" behaviour is actually a consequence of the almost stabilized process that the sample undergoes after a week of immersion; even if literature [77] suggests that the final thickness of such coating is reached only after weeks of immersion. Hence, the 168h-trend is presented as an approximation of the reached steady state.

Each fitting analysis was made using the same software as polarization tests, *Ivium Soft*, on the basis of the hereunder depicted equivalent RC circuit (**Figure 5.16**), like employed in many research works [60, 77, 78].

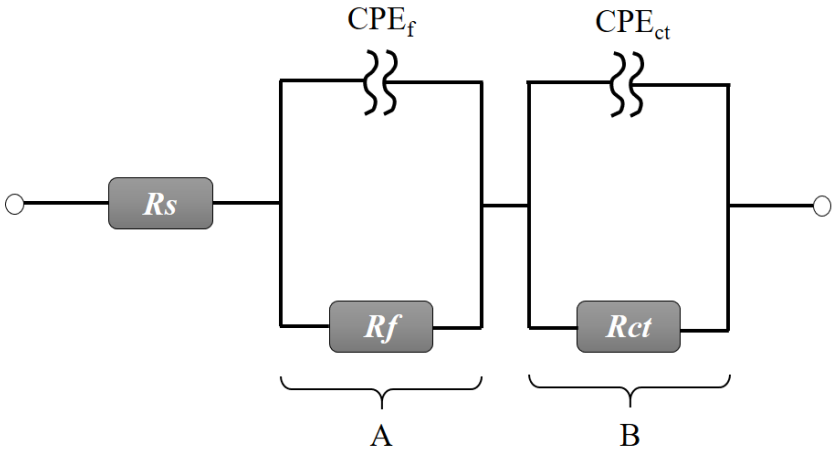

Figure 5. 16: Equivalent RC circuit used for running the fitting analysis on the experimental data.

Where *Rs* represents the Ohmic drop in the electrolyte, *Rf* and *Rct* are, respectively, the passive film and the charge transfer resistance. CPE stands for constant phase electrode, containing the corresponding subscript like the resistance connected in parallel with it. This particular element is utilized instead of a capacitor because of the non-idealistic behaviour of double layer at experimental tests [13]. Each CPE impedance value is often calculated with the following equation (5.2), being the exponent n_i an empirical dispersion coefficient whose amount is between 0 and 1, and *Qi* the i-th capacitance value:

$$Z_{CPEi} = \frac{1}{(j\omega)^{n_i} Q_i} \tag{5.2}$$

It is clear that this equation is similar to equation (1.65) presented in *Section 1.4.1*, where the ideal capacitor's impedance was shown. The difference nonetheless is the dispersion coefficient which, even if might indicate the non-ideal grade of the double layer due to non-uniformity in the exposed surface [37], an empirical base consideration for this variable is preferred [13].

Firstly, the Bode plots are going to be presented in **Figure 5.17**, using a scatter representation for the experimental data and a solid line for the modelling results. Moreover, the increase of time in data collection is indicated with an arrow. Overall, a good agreement between experimental data and the performed fitting analysis is found; presenting small discrepancies mostly at higher frequencies in ϕ-*f* plot. Nonetheless, as known to be the part of the plot exhibiting the *Rs* value, it is not considered that severe of an error as it is presumed to remain constant during the course of the immersion.

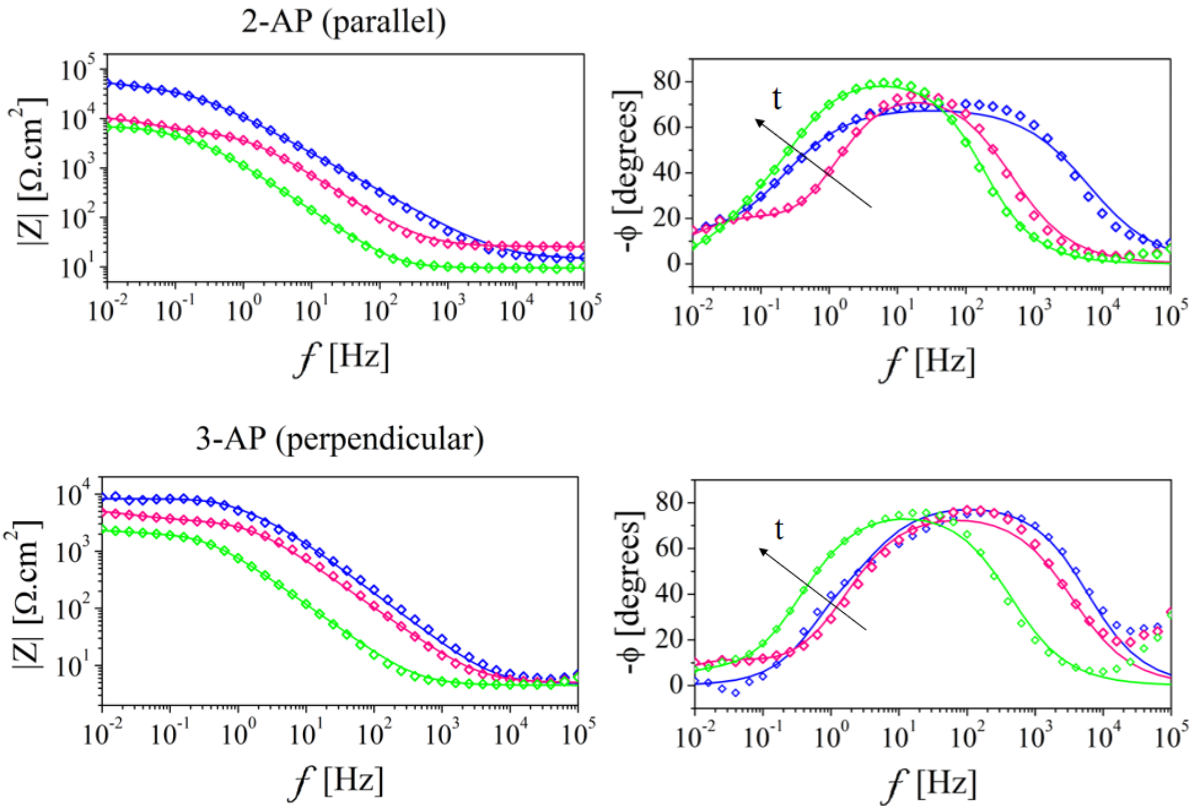

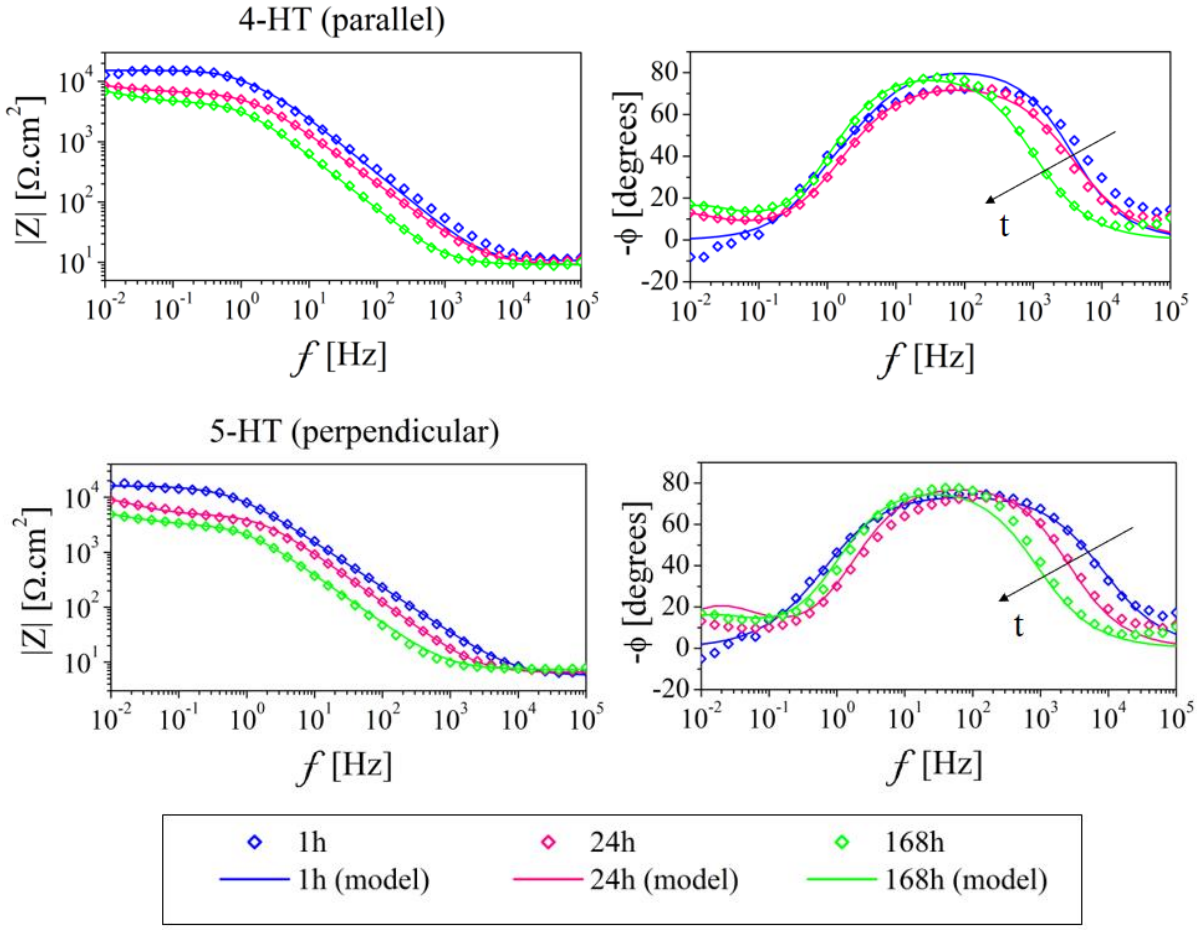

Figure 5. 17: Bode plots representation of the experimental data as well as the fitting results.

From the various Bode plots it is recognizable how the initial impedance magnitude (|Z|) is always higher than the subsequent hours' impedance. This is related to the initial passive state that the alloy presents, which was generated during the previous moments whithin air conditions before the immersion test began. As time passed, the alloy formed a passive layer which gradually achieved its stationary conditions. In agreement with this displacement, the phase angle vs frequency diagrams show a characteristic frequency (f_C) which shifts towards lower values, following the direction of the diplayed arrows.

Moreover, if comparing the first-hour trend with the final 168-h, like depicted in **Figure 5.18**, a more homogenous response is seen in early immersion times while it progresses reaching the final steady passivation state by the end of the test. At this point, more disparity is seen in the heat-treated samples from the as-built one. This is another evidence that supports the first choosing of the presented hours' trend in this thesis.

One common characteristic in all the diagrams is the impedance magnitude value at high frequencies, which is invariable as it represents the electrolyte resistance. This value can be afterward evidenced consistent hereunder when Nyquist plots are presented and also in **Table 5.2** for the fitting parameter of *Rs*.

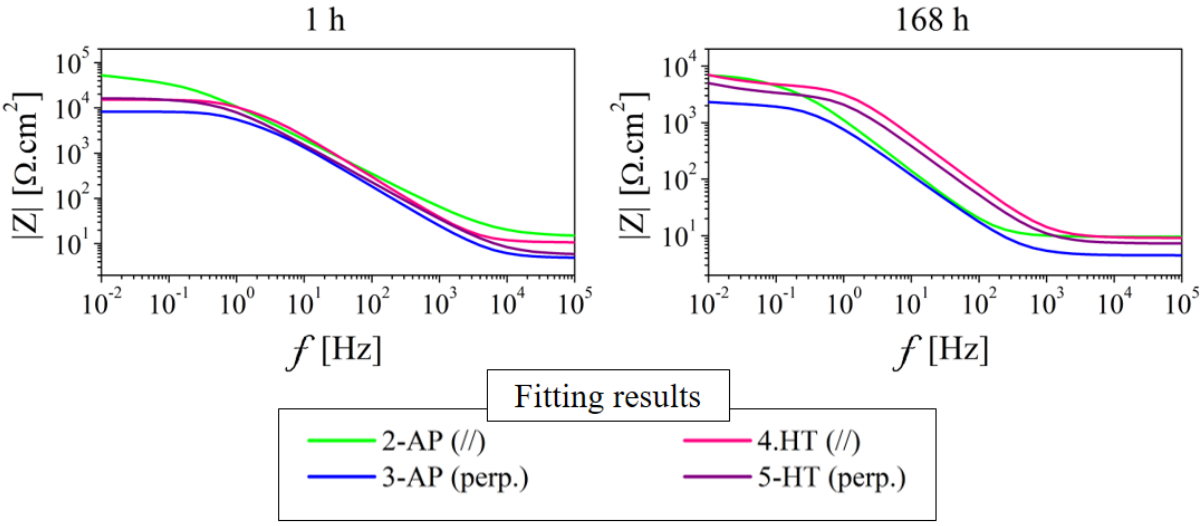

Figure 5. 18: Comparison between the first and last immersion hour in |Z| vs *f* plot.

Conversely, the |Z| value at low frequencies (10^{-2} Hz), which represents the total resistence imposed by the passive film, is seen higher for parallel samples with respect to its perpendicular counterpart, like depicted in **Figure 5.19**. This fact confirmates the corrosion potential values obtained in potentiostatic tests, where XY planes presented lower E_{corr} values than XZ ones. When comparing AP and HT samples it is seen that the corrosion resistance of HT is not lesser than AP, which is concides with research results [83]. The explanation for this behaviour can be elucidated with the E_{corr} values previously found. Heat treated samples presented less negative values than as-built, this means that as-built were thermodinamically more favoured to submit corrosion attack therefore presented a reduced global impedance value.

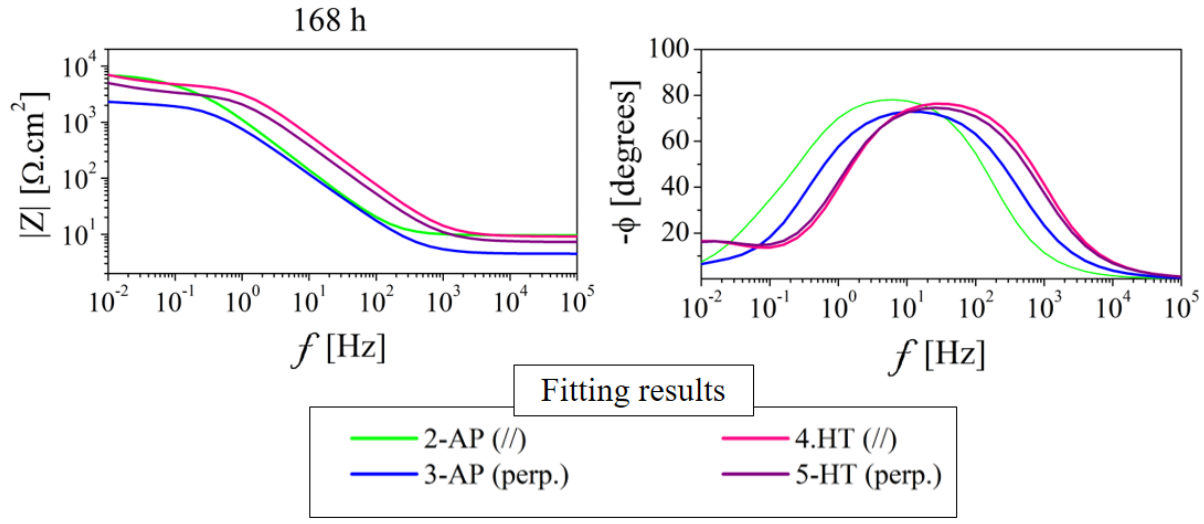

Figure 5. 19: Differentiation between as built and heat treated samples after 168 h of immersion – fitting results.

When analysing the frequency range between 10^0 and 10^3, both AP samples present simmiliar trend different from both HT components. The peaks for these latter specimes are clearly shifted towards higher frequencies with respect to as-printed ones, corresponding also to the change in slope at |Z|-*f* plot. This indicates that the time constant, $\tau_D \sim 1/f_C$, for heat-treated are the smallest. Some works [77] associate this time parameter to the dissolution of the Al-matrix in the vicinities of silicon particles. Hence, higher corrosion rates for HT specimens is here confirmed.

Even if the RC proprosed circuit comprises the equivalent representation of two resistive layers [8], the two generated characteristic time constants are is not quite evidenced in ϕ-*f* plots. Certain reaserch works [34, 77] explain that this phenomenon is actually due to the overlapping of the two characteristic peaks, here not distinguisable, not even after 168 hours of immersion. Nonetheless, a difference can be distinguished between the first-hour curve from the rest, and it is its higher elongation feature (noticeable in **Figure 5.15** and **5.17**). This less marked peak, or wider peak, is attributed to the intial passivation state that characterizes every aluminum alloy within a corrosive environment, like graphically representated in **Figure 3.1** of *Section 3.2*.

When evaluating the Nyquist plots in **Figure 5.20**, the double-layer circuit is more clearly reflected in the configurations for the 24 and 168 h cases. For this reason a second scaled-up adjacent diagram is consistently presented as a way of giving a higher magnification on the reduced semicircles of the 24 and 168 hours. The more defined shapes are better seen in these latter hours because, as immersion time passes, the protective layer is further similar to its final conformation. Therefore, the two time constants are fairly seen in these last cases, with superior definition in the heat-treated case.

In these diagrams, the two characteristic times are reflected by the two almost completely formed semi-circles, where the first shaping at higher frequencies reflects the *B* loop (*Rct* and *CPEct* in parallel) in **Figure 5.16**, and represents at the same time the interface between the electrolyte and the porous oxide layer. Some corrosion studies [60] support this interpretation by suggesting that this part of the circuit reflects the porosity's external covering effect as well as those susceptible areas (like the ones affected by the metal's discontinuities) by corrosion products. Hence, is related with a charge-transfer effect like described in *Section 1.2.1*. By contrast, the second loop (*Rf* and *CPEf* in parallel) reflects the diffusion area between this coating of corroded species and the area within pitting attacks. This means that lower frequencies can accurately assess the interface between the metal and the passive layer, whereas higher frequencies can properly evaluate the interface between the passive layer and the chloride solution.

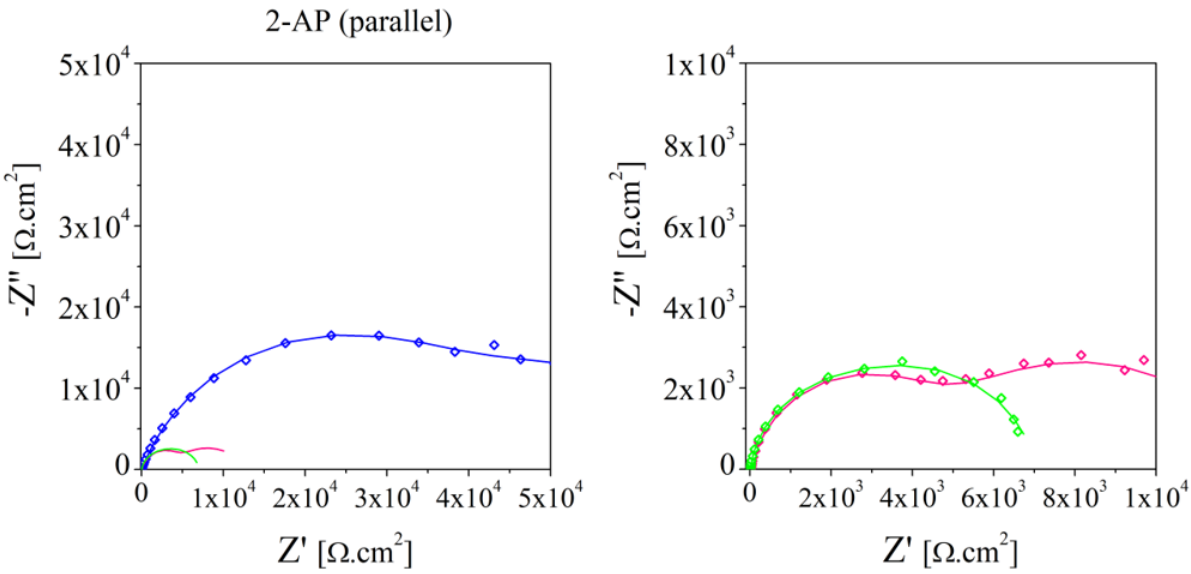
2-AP (parallel)
-Z'' [Ω.cm²]
Z' [Ω.cm²]
5x10⁴
4x10⁴
3x10⁴
2x10⁴
1x10⁴
0
1x10⁴
8x10³
6x10³
4x10³
2x10³

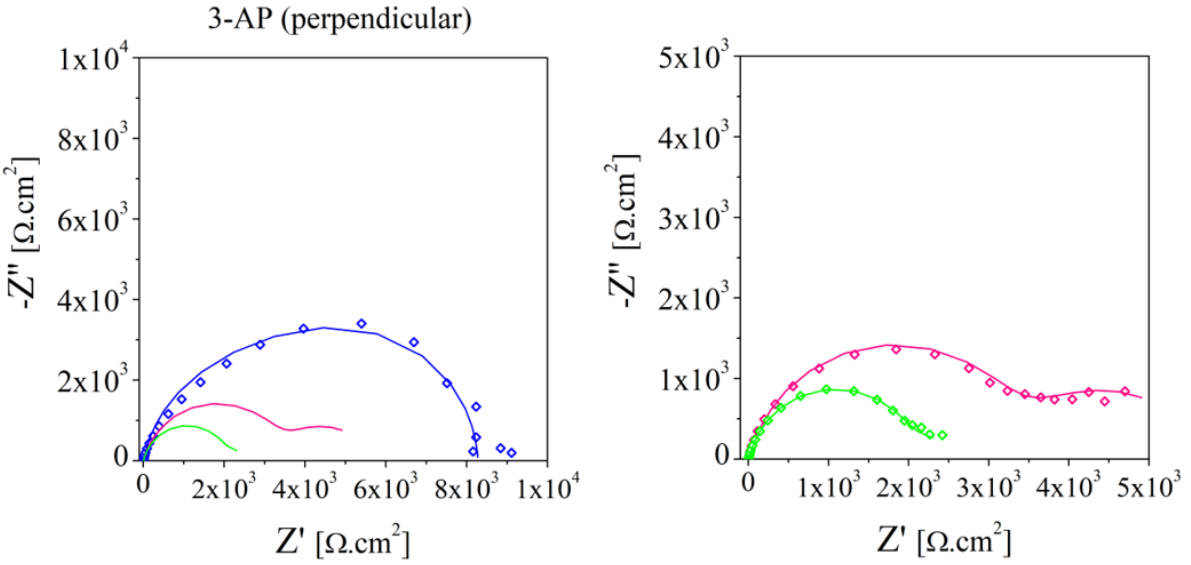
3-AP (perpendicular)
-Z'' [Ω.cm²]
Z' [Ω.cm²]
1x10⁴
8x10³
6x10³
4x10³
2x10³
0
5x10³
4x10³
3x10³
2x10³
1x10³

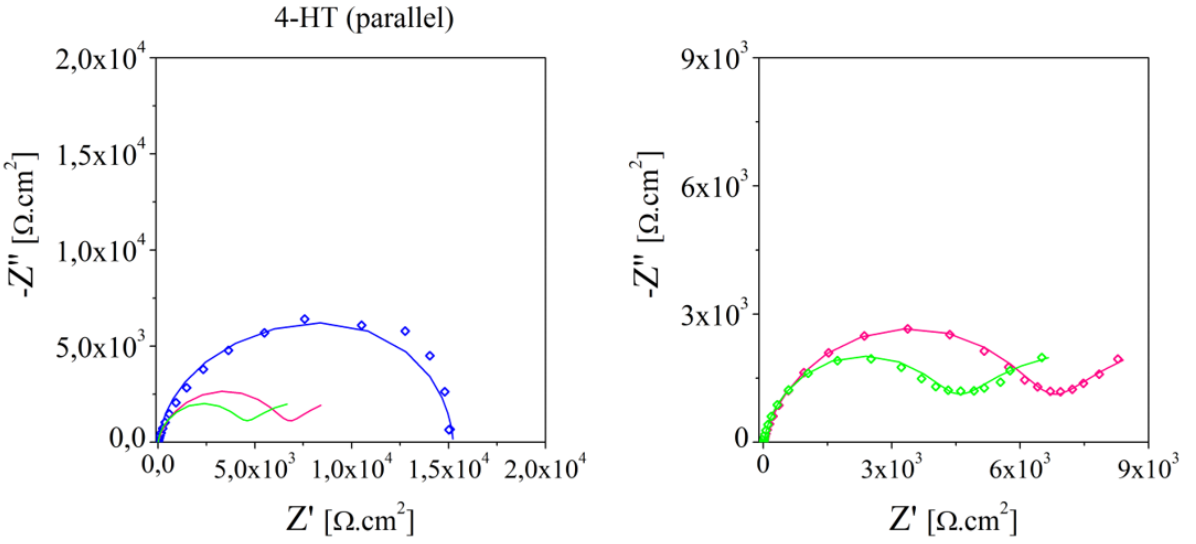
4-HT (parallel)
-Z'' [Ω.cm²]
Z' [Ω.cm²]
2,0x10⁴
1,5x10⁴
1,0x10⁴
5,0x10³
0,0
9x10³
6x10³
3x10³
0

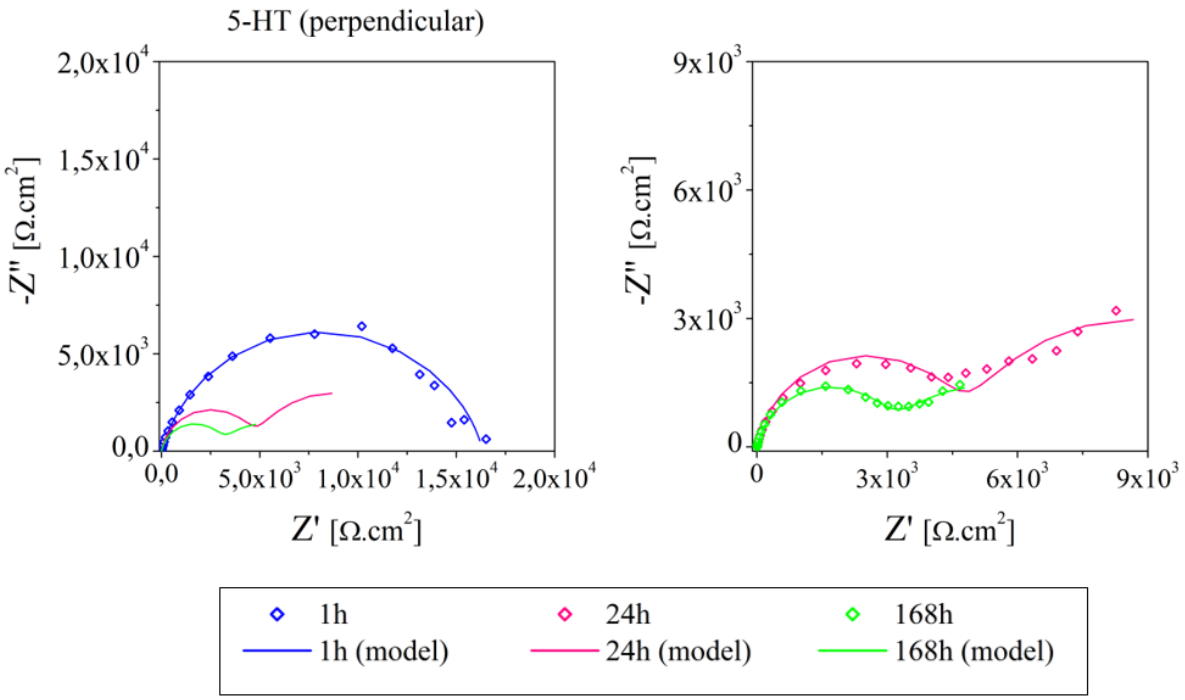

Figure 5. 20: Nyquist plots experimental and fitting results.

For the first-hour semi-circle of as-printed samples, a higher diameter is seen for parallel samples than for perpendicular ones. This indicates a higher impedance response and thereby greater protection provided by the passive film in XZ planes than XY. Satisfactorily, these results are in good agreement with potentiodynamic tests' results, mostly because it reflects the naturally formed layer in the first moments of immersion. Moreover, analysing the following immersion days' results, a higher corrosion behaviour is consistently depicted for parallel planes.

Continuing the evaluation at higher frequency values, for the case of heat-treated samples, a higher diameter is seen for the perpendicular sample, which is not in agreement with polarization results. Nonetheless, from 24 hours onward, the expected resistive behaviour is seen; thus presenting a higher corrosion resistance the parallel plane in HT samples as well.

Further conclusions can be obtained if analysing the fitting parameters that arise from modelling procedure. For this purpose, the main results from the several fitting studies are summarized in **Table 5.2**, always normalized by the actual exposed of each of the samples. Therefore, the resistance values (*Rs*, *Rf* and *Rct*) are presented in $\Omega.cm^2$, the capacitances (CPE_f and CPE_{ct}) in $s^n/(\mu\Omega.cm^2)$, taking into account equation (5.2), and n_1 as well as n_2 are non-dimensional magnitudes:

Table 5. 2: Impedance fitting parameters.

Sample	*Rs* [Ω.cm^2]	*Rf* [Ω.cm^2]	*Rct* [Ω.cm^2]	*CPEf* [s^n/(μΩ.cm^2)]	n_1	*CPEct* [s^n/(μΩ.cm^2)]	n_2
2-AP							
1h	14.4	30624.0	40400.0	314.8	0.7180	21.8	0.7726
24h	25.6	8206.4	4300.8	462,3	0.7000	38,7	0.904
168h	9.6	4401.6	2612.8	513.1	0.8929	226.8	0.9370
3-AP							
1h	4.8	3672.0	4603.0	23.7	0.8720	49.5	0.9987
24h	5	3398.0	2312.0	41.7	0.8522	2206.0	0.7500
168h	4.5	2109.0	395.9	235.1	0.8665	28610.0	0.9087
4-HT							
1h	10.6	9176.2	6040.5	23.6	0.9790	13.1	0.9061
24h	9.1	7448.0	6578.6	2117.1	0.7000	22.2	0.8447
168h	9.1	6362.7	4309.2	1691.4	0.7200	39.4	0.9150
5-HT							
1h	5.7	15381.9	961.5	20.5	0.8338	1137.9	0.9100
24h	6.5	8197.2	4656.7	1120.3	0.7900	25.4	0.9031
168h	7.3	4505.2	3003.5	2116.1	0.700	65.4	0.9011

As a general consideration based upon certain research works [34], the capacitance value is inversely proportional to the passive layer thickness. Hence, heat treatment effects can be clearly seen by the thicker porous layer than AP samples, feature that is noticed in the *CPEct* value for 24h and 168h. Meanwhile, the inner compact layer was always thicker for the AP samples, also with the exception of the first hour. This discrepancy in the initial moments is explained by the fact that, when it is first immersed, the sample may be covered with a passive film that is naturally formed within air conditions and thus the HT samples present higher resistance properties. This is in accord with other research studies [83] for which annealed specimens showed higher quality of compact layer only during the first hour of immersion. As time passes, the thickness of both compact and porous films generally decreases as corrosion attack intensifies.

These results are also linked with the values of resistances as some studies [62] attribute the higher corrosion rate to the lower resistivity of the layer. In all cases *Rf* and *Rct* are higher in the first hour of immersion showing an overall decrease in the subsequent hours. Some samples' *Rf* values, like 2-AP and 5-HT, are even higher than the rest by one order of magnitude. The rapid formation of the compact layer can be attributed to this trend. For as-printed samples, *Rct* is initially higher than *Rf*, in contrast with annealed which present the opposite case. Nonetheless, as the steady state is reached, the inner resistance values decrease for all cases due to increased corrosion attacks. Instead, the *Rct* has a dissimilar trend. For the

AP case it decreases, whereas for the HT increases at 24 h and then decreases. This might indicate that, as the outer porous layer becomes thicker its resistance does as well up to a certain point when the corrosion attack becomes severe, after days of immersion, and thus its resistance decreases.

Taking into consideration the microstructure that gave rise to such passive layer properties, one could argue that the isolation of silicon particles from the previous conformed matrix and also from its depletion from the α-matrix can cause thicker porous layer which seems to gain certain resistance in the first 24 h but not enough to resist further immersion times. A more connected silicon network provides less localized micro-galvanic sites, therefore generating thicker protective layer.

Comparing parallel and perpendicular cases, of the same manufactured type, perpendicular planes persistently show higher *CPEct* values, which suggests superior corrosive properties of parallel surfaces. Similarly, the outer porous layer present higher resistances *Rct* for the XZ case. An opposite trend is followed by the *CPEf* value, indicating that perpendicular planes generate thicker compact layers than parallel ones. Nonetheless, the corresponding resistance values *Rf* in as-printed do confirm that even if the inner coating is thinner, it possesses higher resistance features, therefore providing a higher quality coating. In heat-treated this trend is not seen as *Rf* is also higher in perpendicular cases. This means that when annealing an AM sample, the outer porous layer is the main contribution to corrosion resistance as it is thicker and more resistive for the parallel plane. Such statement is in good agreement with literature [44] that indicates the thickness of the porous layer as the defining factor for corrosion resistance.

Continuing with the comparison between such planes, both AP and HT perpendicular planes show microstructural features that form thinner porous layers and less resistive as well. This is linked therefore to the higher discontinuities in the boundary zone and lesser grain sizes in the finer dendritic zone in the AP specimens. Concurrently, the weaker properties of the outer layer are related to the more scattered, isolated, silicon configuration that XY annealed planes present. Therefore, microstructures that show a more continuous silicon network can certainly enhance corrosion resistance properties by generating a higher-quality passive film, both in AP and HT specimens.

5.4 Limitations in Electrochemical tests

As in every experimental evaluation, there exists certain factors that may vary the experimental results and limit future reproducibility. Even if the employed tests in this thesis have been broadly used since the 1950s because of being a relatively fast and simple to perform experiments, it is still limited by some theoretical and practical issues [44].

Among the theoretical concerns, the measure of i_{corr} follows the Faraday law, as was fairly used in *Section 1.2* of this thesis. This means that a uniform mass loss is considered to be the corrosion characteristic behaviour of the studied alloy. As seen from the many studies addressed to and some final aspects of post-immersion tests, the actual corrosion proceeding of AlSi10Mg as-printed is pitting attack. Therefore, the measurement of i_{corr} gives no information on the type of corrosion and when comparing to heat-treated samples, which actually present a more uniform attack, this response should also be considered.

The practical reasons relate to using properly controlled experimental conditions, such as temperature, electrolyte concentration, aerated or deaerated medium, working electrode's geometry, among others. In this sense, some literature works [9] suggest to avoid geometries

with corners in the working electrode, which was not followed for the as-printed and heat-treated specimens. The use of ultra-pure water and reagents, like NaCl, was acutely respected in order to prevent the contamination of the electrode or the introduction of undesirable components. Nonetheless, a minimum level of uncertainties always remains. Moreover, the polishing procedure between each of the repetitions might also increase this level as a flawless proceeding may not always be reached.

Meanwhile, EIS tests involve other particular limitations on its usage [11]. One of them relates to the association of the electrical response to ideal RC circuit components, which is not always an accurate proceeding. Using distributed impedance elements, like the CPE, clearly improved the fitting process. The equivalent circuit might also represent a limitation but, as a fairly studied process, the one that was employed in this thesis relates to those found in many research works and provides excellent fitting results.

CONCLUSIONS

Throughout the development of this thesis, the potential employment of AM techniques in the automotive industry was studied from the perspective of the corrosion performance that they can deliver. The motivation in using AM technologies instead of traditional ones was also ascertained as for the flexibility in manufacturing that it presents, the potential of easily achieve complex-shaped parts and the low-waste generation that characterizes the laser melting procedure.

From the many experimental tests and discussion of results performed throughout this thesis, understanding the corrosion behaviour of an alloy was revealed to be a true holistic study. It not only comprised electrochemical tests but also microstructure characterization, plus the eventual application of other techniques found in many research works, not herein carried out but nonetheless taken into account for certain interpretations.

The starting point of this study was understanding the characteristics of each of the alloy's microstructure. Casting-made sample characterized by a clearly continuous Al-rich phase with rounded and sometimes elongated shape (average diameter: 16 ± 4 μm). Along its boundaries a finer β-Si phase, rounded elements of less than 1 μm diameter, was noticed together with several porosities. The AM samples presented the characteristic semi-circular conformations (width: 142 ± 68 μm) of the molten pool in the XZ planes, whereas the 67º scanning strategy was clearly identified in the perpendicular plane. Greater magnifications made it possible to appreciate the finer microstructure, composed by a cellular α-Al matrix (spacing not higher than 3 μm) which is supersaturated in silicon and presents at the grain boundaries a silicon-rich phase. The XY plane presented nearly rounded morphologies, whilst in the XZ surface the grains were fairly more elongated. Heat treated samples presented a total different microstructure as now the silicon phase did not form a continuous network but individual and isolated polygonal particles. Nonetheless, a more elongated trend was also seen in the parallel face.

Regarding the potentiodynamic results and the following Tafel analysis, as-printed samples presented less negative values of E_{corr} than cast specimen, whereas the heat-treated had the highest values. This indicated that the corrosion attack was thermodynamically more favoured in cast samples due to the presence of several secondary phases containing Si and Mg, which decisively influence the corrosion resistance by reducing it. Specifically, they enhance the breakdown of the passive film generated as the metal corrodes. Meanwhile in AM alloys these detrimental phases were not present in appreciable amounts as the rapid heating and cooling process allows higher solubility in the α-matrix, thereby explaining their lesser i_{corr} values. Heat treated samples were even less prone, from a thermodynamic point of view, to submit corrosion because of higher thickness on the outer layer of the passive film (condition ascertained within EIS results) together with the characteristic general type of corrosion attack that they expose. Such type of corrosion attack is related with the scattered silicon configuration that characterized HT specimens. This further indicated that pitting initiation in AP samples was thermodynamically more favoured than a uniform attack in annealed ones.

From a kinetic point of view, parallel surfaces consistently presented lesser corrosion rates than perpendicular ones, both for AP and HT samples. Moreover, perpendicular planes results showed greater data dispersion than parallel ones. In the as-printed case EIS modelling parameters confirmed higher *Rf* and *Rct* resistances in parallel planes. Therefore, a more

elongated and less interrupted silicon network in the molten pool boundary zone generated a passivation coating which was more resistive and thinner on the inside and thicker but anyway less resistive on the outside. Meanwhile, a thicker (lesser *CPEct*) and more resistive outer porous layer was determined to be the predominant factor that improves corrosion resistance in annealed samples. This indicated that a silicon distribution being less scattered and more similar to its original as-printed microstructure can undeniably create a higher resistive passive film in XZ-HT planes.

A quite interesting discrepancy was found within EIS characteristic parameters, and it was related to the first hour values. In annealed specimens, the passive film presented a thicker inner layer with respect to the outer one; whereas for the AP case the outer one was thicker. As time passed and the final conformation was further achieved, the outer layer in the HT became greater as the inner layer did for AP samples. Taking into consideration the resistances *Rf* and *Rct*, they were both higher in the first hour for AP and only *Rf* for HT, as impedance plot also depicted, because of the passive film that might have been generated within air conditions moments before the immersion. Nonetheless, as the inner layer became thicker for as-printed, so did its resistance (*Rf*) when compared to the porous *Rct*. Meanwhile, in heat treated samples, as the outer coating became thicker its resistance began to rise until the first 24 h, afterwards it decreased as the corrosion attack became severe.

This phenomenon was also seen in the Bode plots, if comparing the first hour with the last scenario (168 h). Firstly, the |Z| vs *f* graphic showed quite similar curves even overlapping trends, whereas a higher differentiation was achieved by the end of the immersion. Furthermore, Nyquist graphics also depicted the expected two time constants related to the equivalent RC circuit at higher immersion times. This further confirmed that the parameters that are accurate to perform an evaluation were at 24 and 168 hours. In Nyquist plots, the higher diameters in these latter scenarios also corroborated the higher protectiveness that parallel-generated passive film provides with respect to perpendicular-generated ones. Meanwhile, thanks to Bode representations, higher time constants were found for as-printed samples compared to heat-treated, this further verified higher corrosion rates in the annealed case.

Upon these results, and knowing that silicon is more noble than the α-matrix, one main conclusion that can be drawn is that the type of silicon distribution is what ultimately will differentiate the corrosion behaviour of a sample. It is because of this distinction that an AP cellular-microstructure is considered to be more homogeneous and less reactive, from a galvanic point of view, than the disconnected individual silicon particles that characterizes HT specimens. This solute depletion of Si creates “microcathodes” which exceptionally decrease the passive layer resistance. In addition to this, the presence of Mg_2Si phase was corroborated for annealed samples whereas for as-printed was practically absent. This arise of Mg secondary phase creates “microanodes” and dissolve preferentially, thereby increasing the corrosion rate.

Collectively, the determination of Tafel slopes and fitting parameters gave consistent information in most of the cases. However, in other cases some discrepancies arose. It is therefore that limitations in electrochemical tests are to be considered, like the theoretical and practical reasons exposed in the last section of this thesis.

Overall, detrimental effect of 300ºC annealing process on corrosion behaviour still remains as a controversial issue to overcome. Its application was linked to the enhancing of mechanical properties by stress relieving, but this process also increased the corrosion rate. The possibility of developing other alloy compositions can be suggested as a solving path, for instance the use of Al-Mg-Zn alloys which present higher strength, formability and corrosion

resistance than Al-Si-Mg casting alloys [40]. Other way of maintaining corrosion properties in the AM alloy and still diminishing residual stresses is the employment of high-temperature building platforms during the additive procedure (successfully investigated in research works [84]) or even optimizing the scanning strategy. Regardless, other stress relieving processes could be further explored regarding the corrosion response that they may generate.

A second interesting topic for future research is the optimization of surface finish in 3D printing. Within this matter the polished surfaces are to be considered, as all of the results analysed in this thesis are linked to such fishing. It is known that non-polished surfaces show poor corrosion resistance and also that using polished surfaces represents an unfeasible method to apply in finished automotive parts. Therefore, a more realistic approach for less surface defects in AM parts warrants future investigation.

A third and important issue that remains controversial up to date regards the influence that SLM microstructure has on corrosion behaviour. Having ascertained that it clearly changes when submitting heat treatments, further studies on the preferred sites for intermetallic phases precipitation as well as their precise composition is suggested.

Finally, it is of great importance highlighting that the study of corrosion behaviour in automotive AM potential parts comprises just a segment of the studies to be performed before its actual incorporation in the automotive industry can be achieved. Such additional studies include mainly the determination of mechanical properties which, along with the corrosion behaviour, can guarantee a superior functional integration.

REFERENCES

[1] Ducker Frontier (2019) 'Aluminum Content in European Passenger Cars', *European Aluminium*, p. 13. Available at: https://www.european-aluminium.eu/media/2714/aluminum-content-in-european-cars_european-aluminium_public-summary_101019-1.pdf (Accessed: 5 November 2020).

[2] Li, G. (2018) *Nano-inspired biosensors for protein assay with clinical applications*, *Nano-inspired Biosensors for Protein Assay with Clinical Applications*. Nanjing, P. R. China: Elsevier. doi: 10.1016/C2016-0-01779-5.

[3] Bagotsky, V. S. (2006) *Fundamentals of Electrochemistry*. Second Edit. Moscow, Russia. John Wiley & Sons, Inc. doi: 10.1002/047174199X.

[4] Rieger, P. H. (1994) *Electrochemistry*. Second Edit. London, Great Britain: Chapman & Hall. doi: https://doi.org/10.1007/978-94.011.0691-7.

[5] Damaskín, B. B. and Petri, O. A. (1981) *Fundamentos de la Electroquímica Teórica*. Moscú, Rusia: MIR Moscú.

[6] Brett, C. M. A. and Brett, A. M. O. (1993) *Electrochemistry: Principles, methods, and Applications*. First Edit. New Yor, U.S.A. doi: https://doi.org/10.1002/bbpc.19940981033.

[7] Zaki, A. (2006) *Principles of Corrosion Engineering and Corrosion Control*. First Edition. Oxford, UK: Elsevier Ltd. doi: 10.1016/B978-0-7506-5924-6.X5000-4

[8] Orazem, M. E. and Tribollet, B. (2008) *Electrochemical Impedance Spectroscopy*. New Jersey, U.S.A.: John Wiley & Sons, Inc. doi: 10.1002/9780470381588.

[9] Zoski, C. G. (2007) *Handbook of Electrochemistry*. First Edit. New Mexico, USA: Elsevier. doi: https://doi.org/10.1016/B978-0-444-51958-0.X5000-9.

[10] Gileadi, E. (1993) *Electrode Kinetics for Chemical Engineers, and Materials Scientists*. First Edit. WILEY. doi: https://doi.org/10.1002/ange.19941060745.

[11] Barsoukov, E. and Macdonald, J. R. (eds) (2005) *Impedance Spectroscopy -Theory, Experiment, and Applications*. Second Edi. New Jersey, U.S.A.: John Wiley & Sons, Inc. doi: https://doi.org/10.1007/s10008-007-0260-1.

[12] Macdonald, D. D. (1977) *Transient Techniques in Electrochemistry*, *Transient Techniques in Electrochemistry*. Boston, U.S.A.: Springer US. doi: https://doi.org/10.1007/978-1-4613-4145-1.

[13] Gramy Instruments Inc. (2014) 'Basics of Electrochemical Impedance Spectroscopy', pp. 1–28.

[14] Majeed, A. *et al.* (2021) 'A big data-driven framework for sustainable and smart additive manufacturing', *Robotics and Computer-Integrated Manufacturing*. Elsevier Ltd, 67(June 2020), p. 102026. doi: 10.1016/j.rcim.2020.102026.

[15] ISO/ASTM International (2017) 'BSI Standards Publication Additive manufacturing — General principles — Terminology (ISO/ASTM 52900:2015)', pp. 1–19.

[16] Patalas-Maliszewska, J. *et al.* (2020) 'Single Tracks as a Key Factor in Additive Manufacturing Technology-Analysis of Research Trends and Metal Deposition Behavior', *Materials*, 13(5), p. 23. doi: 10.3390/ma13051115.

[17] Djukanovic, G. (2018) *Latest Trends for Aluminium Demand in Automotive Industry*. Available at: https://www.spotlightmetal.com/latest-trends-for-aluminium-demand-in-automotive-industry-a-736213/ (Accessed: 5 November 2020).

[18] Stefanescu, D. M. (2013) *Science and Engineering of Casting Solidification*. Springer US. Available at: https://books.google.it/books?id=u8EGCAAAQBAJ.

[19] Karayel, E. and Bozkurt, Y. (2020) 'Additive manufacturing method and different welding applications', *Journal of Materials Research and Technology*. Korea Institute of Oriental Medicine, 9(5), pp. 11424–11438. doi: 10.1016/j.jmrt.2020.08.039.

[20] Das, S. (2003) 'Physical Aspects of Process Control in Selective Laser Sintering of Metals', *Advanced Engineering Materials*, 5(10), pp. 701–711. doi: 10.1002/adem.200310099.

[21] Thompson, M. K. *et al.* (2016) 'Design for Additive Manufacturing: Trends, opportunities, considerations, and constraints', *CIRP Annals - Manufacturing Technology*. CIRP, 65(2), pp. 737–760. doi: 10.1016/j.cirp.2016.05.004.

[22] Sander, G. *et al.* (2018) 'Corrosion of additively manufactured alloys: A review', *Corrosion*, 74(12), pp. 1318–1350. doi: 10.5006/2926.

[23] Yap, C. Y. *et al.* (2015) 'Review of selective laser melting: Materials and applications', *Applied Physics Reviews*, 2(4). doi: 10.1063/1.4935926.

[24] Yadroitsev, I. and Smurov, I. (2010) 'Selective laser melting technology: from the single laser melted track stability to 3D parts of complex shape', 5(2), pp. 551–560. doi: 10.1016/j.phpro.2010.08.083.

[25] Trevisan, F. *et al.* (2017) 'On the selective laser melting (SLM) of the AlSi10Mg alloy: Process, microstructure, and mechanical properties', *Materials*, 10(1). doi: 10.3390/ma10010076.

[26] Yan, C. *et al.* (2015) 'Microstructure and mechanical properties of aluminium alloy cellular lattice structures manufactured by direct metal laser sintering', *Materials Science and Engineering A*. Elsevier, 628, pp. 238–246. doi: 10.1016/j.msea.2015.01.063.

[27] Paschotta, R. D. (2008) 'RP Photonics Encyclopedia - YAG lasers'. Available at: https://www.rp-photonics.com/yag_lasers.html (Accessed: 20 September 2020).

[28] Zuback, J. S. and DebRoy, T. (2018) 'The hardness of additively manufactured alloys', *Materials*, 11(11). doi: 10.3390/ma11112070.

[29] Liu, Y., Yang, Y. and Wang, D. (2016) 'A study on the residual stress during selective laser melting (SLM) of metallic powder', *International Journal of Advanced Manufacturing Technology*, 87(1–4), pp. 647–656. doi: 10.1007/s00170-016-8466-y.

[30] Huang, L. *et al.* (2018) 'Effect of magnesium content on keyhole-induced porosity formation and distribution in aluminum alloys laser welding', *Journal of Manufacturing Processes*. Elsevier, 33(January), pp. 43–53. doi: 10.1016/j.jmapro.2018.04.023.

[31] Kong, D. *et al.* (2019) 'Corrosion of metallic materials fabricated by selective laser melting', *npj Materials Degradation*. Springer US, 3:24. doi: 10.1038/s41529-019-0086-1.

[32] Revilla, R. I. *et al.* (2020) 'Microstructure and corrosion behavior of 316L stainless steel prepared using different additive manufacturing methods: A comparative study bringing insights into the impact of microstructure on their passivity', *Corrosion Science.*, vol. 176. Elsevier. doi: 10.1016/j.corsci.2020.108914.

[33] Ziętala, M. *et al.* (2016) 'The microstructure, mechanical properties and corrosion resistance of 316 L stainless steel fabricated using laser engineered net shaping', *Materials Science and Engineering A*, 677(November 2016), pp. 1–10. doi: 10.1016/j.msea.2016.09.028.

[34] Nie, J. *et al.* (2020) 'Corrosion mechanism of additively manufactured 316 L stainless steel in 3.5 wt.% NaCl solution', *Materials Today Communications*. Elsevier Ltd., p. 101648. doi: 10.1016/j.mtcomm.2020.101648.

[35] Xie, F. *et al.* (2013) 'Influence of pore characteristics on microstructure, mechanical properties and corrosion resistance of selective laser sintered porous Ti-Mo alloys for biomedical applications', *Electrochimica Acta*. Elsevier Ltd, 105, pp. 121–129. doi: 10.1016/j.electacta.2013.04.105.

[36] Lin, Y. C. *et al.* (2015) 'Corrosion resistance of a two-stage stress-aged Al-Cu-Mg alloy: effects of stress-aging temperature', *Journal of Alloys and Compounds*. Elsevier Ltd, 657, pp. 855–865. doi: 10.1016/j.jallcom.2015.10.114.

[37] Sharma, A. *et al.* (2020) 'Investigation of electrochemical corrosion behavior of additive manufactured Ti–6Al–4V alloy for medical implants in different electrolytes', *Journal of Alloys and Compounds*, vol. 830. Elsevier B.V. doi: 10.1016/j.jallcom.2020.154620.

[38] Dai, N. *et al.* (2016) 'Distinction in corrosion resistance of selective laser melted Ti-6Al-4V alloy on different planes', *Corrosion Science*. Elsevier Ltd, 111, pp. 703–710. doi: 10.1016/j.corsci.2016.06.009.

[39] Paul, T. (2000) 'Corrosion of aluminum and aluminum alloys', *Choice Reviews Online*, 37(05), pp. 37-2798-37–2798. doi: 10.5860/choice.37-2798.

[40] Zolotorevsky, V. S., Belov, N. A. and Glazoff, M. V. (2017) *Casting Aluminium Alloys*. First Edit. Oxford, UK: Elsevier. doi: 10.1017/CBO9781107415324.004.

[41] Somerday, B. P. and San Marchi, C. (2008) 'Hydrogen containment materials', in *Solid-State Hydrogen Storage: Materials and Chemistry*. Elsevier Inc., pp. 51–81. doi: 10.1533/9781845694944.1.51.

[42] Shanmughasundaram, P. and Dahle, A. K. (2018) 'Heat Treatment of Aluminum Alloys', in *Reference Module in Materials Science and Materials Engineering*. Elsevier. doi: 10.1016/B978-0-12-803581-8.03374-9.

[43] Vargel, C. (2004) *Corrosion of Aluminium*, *Corrosion of Aluminium*. Elsevier B.V. doi: 10.1016/B978-0-08-044495-6.X5000-9.

[44] Vargel, C. (2004) *Corrosion of Aluminium*, *Corrosion of Aluminium*. Oxford, UK: Elsevier B.V. doi: 10.1016/B978-0-08-044495-6.X5000-9.

[45] CiAl (2019) *Il riciclo dell'alluminio in Italia*. Available at: https://www.cial.it/category/alluminio-e-riciclo/il-riciclo/ (Accessed: 26 September 2020).

[46] Foley, R. T. (1986) 'Localized Corrosion of Aluminum Alloys - a Review.', *Corrosion*, 42(5), pp. 277–288. doi: 10.5006/1.3584905.

[47] Cole, G. S. and Sherman, A. M. (1995) 'Lightweight materials for automotive applications', *Materials Characterization*. Elsevier Science Inc. 35(1), pp. 3–9. doi: 10.1016/1044-5803(95)00063-1.

[48] Hirsch, J. (2014) 'Recent development in aluminium for automotive applications', *Transactions of Nonferrous Metals Society of China (English Edition)*. Elsevier, 24(7), pp. 1995–2002. doi: 10.1016/S1003-6326(14)63305-7.

[49] UACJ Corporation. (2020) *Aluminum Alloy Sheets for Automobile Panels:* Available at: https://www.uacj.co.jp/english/products/sheeting/aas-panel.htm#ac01 (Accessed: 6 November 2020).

[50] Tolum, F. (2019) 'Use of Aluminium Alloys in Automotive Industry'. *International Mediterranean Natural Sciences, Health Sciences and Engineering Congress* (R. Aydin & H. Yildiz, ed.), Sarajevo, Bosnia and Herzegovina, 10-12 September 2019. Printed edition, Vol. 3 (4) pp. 63-72 [ISSN: 2566-3402].

[51] Das, S. K., Green, J. A. S. and Kaufman, J. G. (2007) 'The Development of Recycle-Friendly Automotive Aluminum Alloys', *JOM*. Springer, 59(11), pp. 47–51. doi: 10.1007/s11837-007-0140-2.

[52] Asension-lozano, J. (2009) 'The Al-Si Phase Diagram', *Buehler*, 5(1). doi: 10.1017/S1431927609092642.

[53] Dobkowska, A. *et al.* (2016) 'The comparison of the microstructure and corrosion resistance of sand cast aluminum alloys', *Archives of Metallurgy and Materials*, 61(1), pp. 209–212. doi: 10.1515/amm-2016-0038.

[54] Sokkalingam, P. *et al.* (2020) 'Rheo-Die-Casting of Al-Si-Mg Alloy and Al-Si-Mg/SiCp Composites: Microstructure and Wear Behavior', *Materials Research*, 23(2).

[55] Yan, Q., Song, B. and Shi, Y. (2020) 'Comparative study of performance comparison of AlSi10Mg alloy prepared by selective laser melting and casting', *Journal of Materials Science & Technology*. The editorial office of Journal of Materials Science & Technology, 41, pp. 199–208. doi: 10.1016/j.jmst.2019.08.049.

[56] Iturrioz, A. *et al.* (2018) 'Selective laser melting of AlSi10Mg alloy: influence of heat treatment condition on mechanical properties and microstructure', *Welding in the World*. Welding in the World, 62(4), pp. 885–892. doi: 10.1007/s40194-018-0592-8.

[57] Alghamdi, F. and Haghshenas, M. (2019) 'Microstructural and small-scale characterization of additive manufactured AlSi10Mg alloy', *SN Applied Sciences*. Springer International Publishing, 1(3), pp. 1–10. doi: 10.1007/s42452-019-0270-5.

[58] Prashanth, K. G. *et al.* (2014) 'Microstructure and mechanical properties of Al-12Si produced by selective laser melting: Effect of heat treatment', *Materials Science and Engineering A*. Elsevier, 590, pp. 153–160. doi: 10.1016/j.msea.2013.10.023.

[59] Salmi, A. and Atzeni, E. (2020) 'Residual stress analysis of thin AlSi10Mg parts produced by Laser Powder Bed Fusion', *Virtual and Physical Prototyping*. Taylor & Francis, 15(1), pp. 49–61. doi: 10.1080/17452759.2019.1650237.

[60] Cabrini, M. *et al.* (2016) 'Evaluation of corrosion resistance of Al-10Si-Mg alloy obtained by means of Direct Metal Laser Sintering', *Journal of Materials Processing Technology*. Elsevier B.V., 231, pp. 326–335. doi: 10.1016/j.jmatprotec.2015.12.033.

[61] Takata, N. *et al.* (2017) 'Change in microstructure of selectively laser melted AlSi10Mg alloy with heat treatments', *Materials Science and Engineering A*. Elsevier B.V., 704(May), pp. 218–228. doi: 10.1016/j.msea.2017.08.029.

[62] Gu, X. *et al.* (2019) 'Abnormal corrosion behavior of selective laser melted AlSi10Mg alloy induced by heat treatment at 300 °C', *Journal of Alloys and Compounds*. Elsevier B.V, 803, pp. 314–324. doi: 10.1016/j.jallcom.2019.06.274.

[63] Wei, P. *et al.* (2017) 'The AlSi10Mg samples produced by selective laser melting: single track, densification, microstructure and mechanical behavior', *Applied Surface Science*. Elsevier B.V., 408, pp. 38–50. doi: 10.1016/j.apsusc.2017.02.215.

[64] Liu, H. and Altan, M. (2002) *Science and Engineering of Droplets: Fundamentals and Applications*, *Applied Mechanics Reviews*. New York, U.S.A.: Noyes Publications. doi: 10.1115/1.1445335.

[65] *Mechanical Cross-Sectioning — Sample Preparation | www.labs-services.com* (no date). Available at: http://www.labs-services.com/mechanical-cross-sectioning-sample-preparation/ (Accessed: 12 September 2020).

[66] *Pulidora Automatica Mecatech 234 (Pulido y Desbaste) Presi - Grupo Testek* (no date). Available at: https://www.testekndt.net/producto/mecatech-234 (Accessed: 9 October 2020).

[67] Ensminger, D. and Stulen, F. B. (2008) *Ultrasonics: Data, equations and their practical uses*, *Ultrasonics: Data, Equations and Their Practical Uses*. Available at: https://books.google.it/books?id=u2XlPFCbVPgC&pg=PA328&dq=ultrasonic+cleaning&hl=en&sa=X&ei=fUPwTpOlNefhiALayIjIDg&redir_esc=y#v=onepage&q=ultrasonic cleaning&f=false (Accessed: 9 October 2020).

[68] Roberge, P. R. (2002) *Corrosion books: Handbook of Corrosion Engineering*, *Materials and Corrosion*. New Yor, U.S.A: McGraw-Hill. doi: 10.1002/1521-4176(200204)53:4<284::AID-MACO1111284>3.0.CO;2-8.

[69] Rodríguez Rius, Daniel (2000). Obtención de capas de nitruro de titanio mediante tratamiento termoquímico en titanio y Ti6A14V y caracterización de sus propiedades para aplicaciones biomédicas. Tesis Doctoral, Universitat Politècnica de Catalunya. Available at: http://hdl.handle.net/10803/6032.

[70] Joy, D. C. (2019) *Scanning electron microscope*. Encyclopædia Britannica. Available at: https://www.britannica.com/technology/scanning-electron-microscope (Accessed: 8 November 2020).

[71] Bozzola, J. J. and Russell, L. D. (1999) *Electron Microscopy*. 2nd Edition. Toronto, Canada: Jones and Barlett Publishers Canada.

[72] Goldstein, J. I. *et al.* (2012) *Scanning electron microscopy and X-ray microanalysis*. 3rd Edition. New York, U.S.A.: Springer New York. doi: 10.1007/978-1-4615-0215-9.

[73] Manfredi, D. *et al.* (2013) 'From Powders To Dense Metal Parts: Characterization of a Commercial AlSiMg Alloy Processed through Direct Metal Laser Sintering', *Materials*, 6(3), pp. 856–869. doi: 10.3390/ma6030856.

[74] Cabrini, M. *et al.* (2016) 'Corrosion resistance of direct metal laser sintering AlSiMg alloy', *Surface and Interface Analysis*, 48(8), pp. 818–826. doi: 10.1002/sia.5981.

[75] Lam, L. P. *et al.* (2015) 'Phase analysis and microstructure characterisation of AlSi10Mg parts produced by Selective Laser Melting', *Virtual and Physical Prototyping*, 10(4), pp. 207–215. doi: 10.1080/17452759.2015.1110868.

[76] Durejko, T. *et al.* (2016) 'The microstructure, mechanical properties and corrosion resistance of 316 L stainless steel fabricated using laser engineered net shaping', *Materials Science & Engineering A*. Elsevier B.V., 677, pp. 1–10. doi: 10.1016/j.msea.2016.09.028.

[77] Cabrini, M. *et al.* (2016) 'Effect of heat treatment on corrosion resistance of DMLS AlSi10Mg alloy', *Electrochimica Acta*. Elsevier Ltd, 206, pp. 346–355. doi: 10.1016/j.electacta.2016.04.157.

[78] Battocchi, D. *et al.* (2006) 'Comparison of testing solutions on the protection of Al-alloys using a Mg-rich primer', *Corrosion Science*. Elsevier Ltd, 48(8), pp. 2226–2240. doi: 10.1016/j.corsci.2005.05.059.

[79] Cai, C. *et al.* (2018) 'Microstructure evolution of AlSi10Mg(Cu) alloy related to isothermal exposure', *Materials*, 11(5). doi: 10.3390/ma11050809.

[80] Leon, A., Shirizly, A. and Aghion, E. (2016) 'Corrosion behavior of AlSi10Mg alloy produced by additive manufacturing (AM) vs. Its counterpart gravity cast alloy', *Metals*, 6(7). doi: 10.3390/met6070148.

[81] Fratila-Apachitei, L. E., Apachitei, I. and Duszczyk, J. (2006) 'Characterization of cast AlSi(Cu) alloys by scanning Kelvin probe force microscopy', *Electrochimica Acta*, 51(26), pp. 5892–5896. doi: 10.1016/j.electacta.2006.03.027.

[82] Ambat, R. *et al.* (2006) 'Effect of iron-containing intermetallic particles on the corrosion behaviour of aluminium', *Corrosion Science*. Elsevier, 48(11), pp. 3455–3471. doi: 10.1016/j.corsci.2006.01.005.

[83] Rafieazad, M., Mohammadi, M. and Nasiri, A. M. (2019) 'On microstructure and early stage corrosion performance of heat treated direct metal laser sintered AlSi10Mg', *Additive Manufacturing*. Elsevier, 28(April), pp. 107–119. doi: 10.1016/j.addma.2019.04.023.

[84] Cabrini, M. *et al.* (2018) 'Corrosion behavior of heat-treated AlSi10Mg manufactured by laser powder bed fusion', *Materials*, 11(7). doi: 10.3390/ma11071051.

APPENDIX A

SYMBOLS AND UNITS

Table A. 1: List of symbols and physical constants

Symbol	Name	Units
A	Cross-sectional area	m^2
a	Activity	*None*
α	Cathodic transfer coefficient	*None*
b	Tafel Slopes	*None*
β	Anodic transfer coefficient	*None*
C	Capacitance	F/cm^2
C_G	Capacity of the Gouy layer	C/V
C_O	Concentration of the oxidized species	mol/L
C_O*	Bulk concentration of the oxidized species	mol/L
C_R	Concentration of the reduced species	mol/L
C_R*	Bulk concentration of the reduced species	mol/L
c	Concentration	mol/L
γ	Activity coefficient	*None*
γs	Surface tension	J/m^2
D_O	Diffusion coefficient	cm^2/s
d	Average crystallite dimension	m
E	Potential	V
E^0	Standard potential	V
E_{corr}	Corrosion potential	V
E_e	Equilibrium potential	V
ε	Dielectric constant of a medium	$C^2/(J.m)$
ε_0	Free space permittivity	$C^2/(J.m)$
ε_F	Electromotive force	V
ζ_{ei}	Data point	*None*
ζ_k	Theoretical model point	*None*

F	Faraday Constant	C/mol
f	Frequency	Hz (cycle/s)
f_C	Characteristic relaxation frequency	Hz
ϕ	Potential	V
G	Gibbs Free Energy	J/mol
η	Overpotential	V
H	Enthalpy	J/mol
I	Net flowing current	A
I_S	Ionic Strength	mol/L
i	Current density	A/cm^2
i_{corr}	Corrosion current density	A/cm^2
J_O	Oxidize species flux	$mol/s.cm^2$
K	Equilibrium constant	*None*
Kc	Conversion constant	mm/(μA.cm.y)
k	Rate constant	m/s
k_{HP}	Hall-Petch characteristic slope	$MPa.m^{1/2}$
M	Molar mass	g/mol
n	Number of moles	mol
n_e	Exchanged electrons	*None*
ν	Coefficient of a chemical formula	*None*
P	Pressure	bar (10^5 MPa)
Q	Heat	J
q	Charge	C
μ	Chemical potential	J/mol
μ^0	Standard chemical potential	J/mol
R	Resistance	Ω
Rct	Charge-transfer resistance	
Re	Electrolyte resistance	Ω
Rp	Polarization resistance	Ω
ρ	Density	g/cm^3
S	Entropy	J/(mol.K)
S_m	Sum of squares functions	*None*
σ	Strength	MPa
σ_0	Lattice resistance for dislocation movement	MPa

σ_M	Charge density	C/m^2
T	Temperature	ºC
t	Time	s
τ_D	Characteristic relaxation time	s
U	Internal energy	J/mol
V	Volume	m^3
v_{corr}	Corrosion rate	mm/y
ϕ	Phase angle	degrees
w	Work	J
w_{elec}	Electrical Work	J
w_i	Specific weight of a parameter	*None*
x	Space coordinate	*None*
Z_r	Pre-exponential term	m/s
Z	Impedance	$\Omega.cm^2$
Z'	Real part of the impedance	$\Omega.cm^2$
Z''	Imaginary part of the impedance	$\Omega.cm^2$
|Z|	Impedance magnitude	$\Omega.cm^2$
ω	Angular frequency	s^{-1} (radians/s)
ω_C	Characteristic angular frequency	s^{-1}

APPENDIX B

THERMODYNAMIC EXPRESSIONS USED IN ELECTROCHEMISTRY

As the aim of this thesis is not the complete development of thermodynamics theory, only the section that is going to be useful for the understanding of the corrosion analysis is here presented.

For closed systems which can submit changes but within equilibrium states, there are certain relations between fundamental properties that can be defined as follows [1]:

$$dU = T\,dS - P\,dV \tag{B.1}$$

$$dH = T\,dS - V\,dP \tag{B.2}$$

$$dG = V\,dP - S\,dT \tag{B.3}$$

where the enthalpy (H) and the Gibbs Energy (G) are correspondingly defined as:

$$H = U + PV \tag{B.4}$$

$$G = H - TS \tag{B.5}$$

being: U the internal energy, S the entropy, T the temperature, P the pressure and V the volume.

The Gibbs energy is a thermodynamic potential which determines whether a reaction will occur spontaneously ($\Delta G < 0$) or not. When its value is equal to zero, then it means that the reaction is at its equilibrium state.

If the system is composed of more than one pure component, then the total Gibbs energy (nG) will be the sum of each component's contribution as the following expression denotes:

$$nG = \sum n_k \,.\, G_k \tag{B.6}$$

where n_k is the k component's number of moles and G_k its Gibbs energy per mole.

Therefore, if the number of moles (n) is added to the equation (B.6) then:

$$d(nG) = (nV)\,dP - (nS)\,dT \tag{B.7}$$

On the contrary, for the making of a more general equation which represents an open system, is important to note that the Gibbs energy will not only be dependent of temperature and pressure conditions, but also on the specie's mole number:

$$nG = g(T, P, n_1, n_2, \ldots, n_i, \ldots) \tag{B.8}$$

These kind of systems are not formed by pure components but by components being part of mixed phases with fluctuating composition due to mixing or separation processes, transference processes or a chemical reaction.

Most electrochemical experiments are carried out under constant pressure and temperature conditions [2]. Consequently, the equation (B.7) can be rewritten as:

$$d(nG) = \sum_i \left[\frac{d(nG)}{dn_i} \right]_{T,P,nj} dn_i \tag{B.9}$$

where the sum is done for all the species and the term *nj* would indicate that the moles of the "i"th species varies while the rest of the species remain constant.

The equation (B.9) makes it possible to define the chemical potential (J/mol) of the "i"th species as:

$$\mu_i = \left[\frac{d(nG)}{dn_i} \right]_{T,P,nj} \tag{B.10}$$

Starting from the formulas (B.1) to (B.3), and developing a sequence of thermodynamic formulas, the following expression can be obtained for ideal gases:

$$\mu_i = \mu_i^{\,0} + RT \ln(p_i) \tag{B.11}$$

where μ_i^0 is the standard chemical potential (a constant parameter independent of the system's composition) and p_i the partial pressure of the "i"th species. The standard conditions imply:

a) For gases: a pure substance, considered as an ideal gas at 1 bar.

b) For liquid and solids: a pure substance at 1 bar.

As μ_i depends, in part, on the partial pressure of the stated substance (p_i), then it is pertinent to state that for ideal substances the μ_i of a substance depends on the concentration (c_i):

$$\mu_i = \mu_i^{\,0} + RT \ln(c_i) \tag{B.12}$$

This allows to work, along thermodynamic theory, with chemical potentials using a measureable magnitude (the concentration). Nonetheless, if working with no ideal solutions, this expression is no longer valid. This is the reason why the concept of a component's activity (a) is here presented. Gilbert N. Lewis (1907) defined this parameter with the equation:

$$\mu_i = \mu_i^{\,0} + RT \ln(a_i) \tag{B.13}$$

This means that in highly diluted solutions, the value of a_i approaches the concentration's one. Moreover, the concept of activity coefficient (γ) is necessary to represent how much a non-ideal solution approaches to the ideal state. Therefore,

$$a = \gamma\left(\frac{c}{c^0}\right) \tag{B.14}$$

being c^o = 1mol/L, the standard state concentration and the activity (a) a dimensionless quantity.

If equation (B.13) should be expressed in terms of Gibbs energy, thanks to the equation (B.10), we have:

$$G_i = G_i^{\,0} + RT\ln(a_i) \tag{B.16}$$

Considering the following general chemical reaction [3]:

$$\alpha.A + \beta.B \leftrightarrow \gamma.C + \delta.D \tag{B.17}$$

it is possible to calculate the change in the Gibbs energy, on the basis of equation (B.11), with the following equation (B.18) taking into account each of the coefficients (ν_i):

$$\Delta G_{rx} = \sum_{prod} \nu_i G_i - \sum_{react} \nu_i G_i \tag{B.18}$$

$$\Delta G_{rx} = \gamma(G_c^{\,0} + RT\ln a_C) + \delta(G_D^{\,0} + RT\ln a_D) + \tag{B.19}$$
$$-\alpha(G_A^{\,0} + RT\ln a_A) - \beta(G_B^{\,0} + RT\ln a_B)$$

Introducing the term $\Delta G_{rx}^{\,0} = \gamma.G_c^{\,0} + \delta.G_D^{\,0} - \alpha.G_A^{\,0} - \beta.G_B^{\,0}$, we have:

$$\Delta G_{rx} = \Delta G_{rx}^{\,0} + RT\ln\left(\frac{a_C^{\,\gamma}.a_D^{\,\delta}}{a_A^{\,\alpha}.a_B^{\,\beta}}\right) \tag{B.20}$$

As said before, at the equilibrium the change in Gibbs energy is zero. Hence, the equilibrium constant (K) is defined as:

$$K = \left(\frac{a_C^{\,\gamma}.a_D^{\,\delta}}{a_A^{\,\alpha}.a_B^{\,\beta}}\right) \tag{B.21}$$

And the change in standard Gibbs energy will always be:

$$\Delta G_{rx}^{\,0} = -RT\ln K \tag{B.22}$$

REFERENCES

[1] Smith, J. M., Ness, H. C. Van and Abbott, M. M. (1997) *Introducción a la Termodinámica en Ingeniería Química*. 5th edn. Mexico, D.F.: McGraw-Hill Education.

[2] Bagotsky, V. S. (2006) *Fundamentals of Electrochemistry*. Second Edit. Moscow, Russia. John Wiley & Sons, Inc. doi: 10.1002/047174199X.

[3] Zaki, A. (2006) *Principles of Corrosion Engineering and Corrosion Control*. First Edition. Oxford, UK: Elsevier Ltd. doi: 10.1016/B978-0-7506-5924-6.X5000-4.

Acknowledgements

Firstly, I would like to extend my sincere thanks to Professor Sabrina Grassini for accepting my request in developing this thesis, for her constant guidance and her always friendly manner.

Secondly, I am extremely grateful to Alessio Gullino, PhD student who patiently helped me from the very beginning, guided me in every laboratory test, showed me the beauty of polishing and offered countless practical suggestions. I am also deeply grateful for his uninterrupted guidance during the "Covid situation", which certainly cannot be underestimated.

Thirdly, my course at Politecnico di Torino would have not been possible if not by my family support, Jimmy, Mabel, Sofía and Hilda, to whom I will always be grateful.

Lastly, I could not end this final page without mentioning Federico who has always given me unwavering support and played a decisive role on this thesis' Italian summary.